Experimental Study of Branching Fins for Enhanced Heat Transfer in Latent Energy Storage System

By

Jonas Skaalum

Submitted in partial fulfilment of the requirements
for the degree of Master of Applied Science

at

Dalhousie University
Halifax, Nova Scotia
December 2017

To my family, friends, and Rebecca.

Table of Contents

List of Tables

List of Figures

Abstract

Thermal energy from sustainable sources is a growing percentage of the global energy budget, one which requires storage technologies for effective use. For thermal energy, latent heat energy storage systems (LHESSs) offer the potential for significantly improved energy density and quality compared to traditional systems. Most materials suitable for use in LHESSs, however, have very low thermal conductivities leading to limited heat transfer rates and requiring advances in heat exchanger design for these systems.

A comparative study was performed between a heat exchanger with bifurcated fins and heat exchangers with straight fins within a LHESS. The bifurcated fins transferred less energy than the straight fins during charging tests due to their reduced ability to form convective cells of molten phase change material. During discharge the bifurcated geometry provided a lower but steadier rate of heat transfer, and exchanging slightly more energy over an eight-hour period than the straight fins.

List of Abbreviation and Symbols Used

Dimensional Variables	
A	Surface area (m^2)
c_p	Heat capacity (kJ kg^{-1} K^{-1})
D	Inside pipe diameter (m)
E	Energy (J)
L	Latent heat (J kg^{-1})
m	Mass (kg)
$\dot{m}$	Mass flow rate (kg s^{-1})
$\dot{q}$	Rate of heat transfer (W)
$\dot{Q}$	Rate of heat transfer (W)
t	Time (s)
T	Temperature (K)
U	Uncertainty
$\dot{V}$	Volumetric flow rate (m^3 s^{-1})
Greek Letters	
Δ	Change
ε	Effectiveness
μ	Dynamic viscosity (N s m^{-2})
ρ	Density (kg m^{-3})
φ	Melt fraction
Subscripts	
E	Energy
f	Final
i	Initial
m	Mass
Abbreviations	
CAD	Computer Aided Design
CAD	Canadian Dollars
cDAQ	Compact Data Acquisition System
DAQ	Data Acquisition System
HTF	Heat Transfer Fluid
LHESS	Latent Heat Energy Storage System
LMTD	Log-Mean Temperature Difference
NI	National Instruments
NTU	Number of Transfer Units
PCM	Phase Change Material
Non-Dimensional Variables	
Re_D	Reynolds number ($\rho u D/\mu$)
Ste	Stefan number ($c_p \Delta T/L$)

Acknowledgements

I would like to thank my supervisor Dr. Dominic Groulx for guidance and support over the course of this project, and my committee members, Dr. Michael Pegg and Dr. Alain Joseph, for their time and feedback.

I would also like to acknowledge the technical and support staff at the Department of Mechanical Engineering, especially Kate Hide, Albert Murphy, Mark MacDonald, Angus MacPherson, and Peter Jones. Their help during this project was invaluable. Thanks are also owed to Simon Maranda for helping me solve the leaking problem.

This work was made possible by the generous funding of the Natural Sciences and Engineering Research Council of Canada (NSERC), as well as the Government of Nova Scotia through the Nova Scotia Graduate Scholarship.

Chapter 1. INTRODUCTION

1.1. Background

Due to the particulars of the Canadian climate, a significant portion of the country's energy budget is spent on heating buildings. In 2013, for example, 14 % of the country's secondary energy consumption was used for space and water heating within the residential and commercial/institutional sectors. The majority of this space heat was generated using natural gas (50 %), electricity (25 %), and wood (17 %) (Natural Resources Canada, 2017). As a party to the Paris Agreement, the government of Canada has set out a framework for reducing the greenhouse gas emissions of the population (Government of Canada, 2016). Part of this framework involves shifting the country's supply of energy towards low-carbon sources, such as solar and wind harvesting. Many of these sources are, however, extremely time-sensitive in terms of their supply. The availability of solar energy, for example, depends on the time of day and local weather conditions, as well as the season. As a result, the supply of energy from these sources does not always match the demand, and an energy storage system is required to bridge the gap.

There are three general forms in which thermal energy may be stored; sensible heat, latent heat, and thermochemical heat. Sensible heat refers to thermal energy that manifests as a change in the temperature of an object. Latent heat is thermal energy that contributes to a change of phase such as from solid to liquid without changing the temperature. Thermochemical heat storage systems convert heat into chemical potential energy through a reversible reaction, usually producing two substances that can be recombined to release the stored heat (Yan *et al.*, 2015). Sensible heat storage is ubiquitous in the heating systems of residential and commercial buildings. Hot water tanks, for either potable use or space heating, can commonly be found in basements or closets. The advantage of the hot water tank is that frequent, non-periodic, and short-duration demands for warm water can be met without relying on a high ramp-rate heat source, such as by burning natural gas. There are several limitations, however, to energy storage through purely sensible heating. Firstly, storing energy as sensible heat results in a higher temperature gradient between the storage medium and the environment, which leads to self-discharge. Secondly, as sensible heat is

added or removed from the system the temperature of the storage medium changes. As the storage medium approaches the temperature of the surroundings, there is a corresponding decrease in the quality of the stored energy as well as the rate at which it can be transferred. Thirdly, the energy density of sensible heat storage is limited by the heat capacity of the material and the temperature limits of the application (Tatsidjodoung *et al.*, 2013). In a domestic hot water tank, for example, the maximum temperature of the water is limited to prevent steam formation and dangerous pressure buildup. Therefore, the maximum quantity of heat that can be stored in a hot water tank is limited to the largest size of tank that may be installed.

The motivation for research into latent heat energy storage systems (LHESSs) is their potential for improving on the space and weight limitations of storing thermal energy as purely sensible heat.

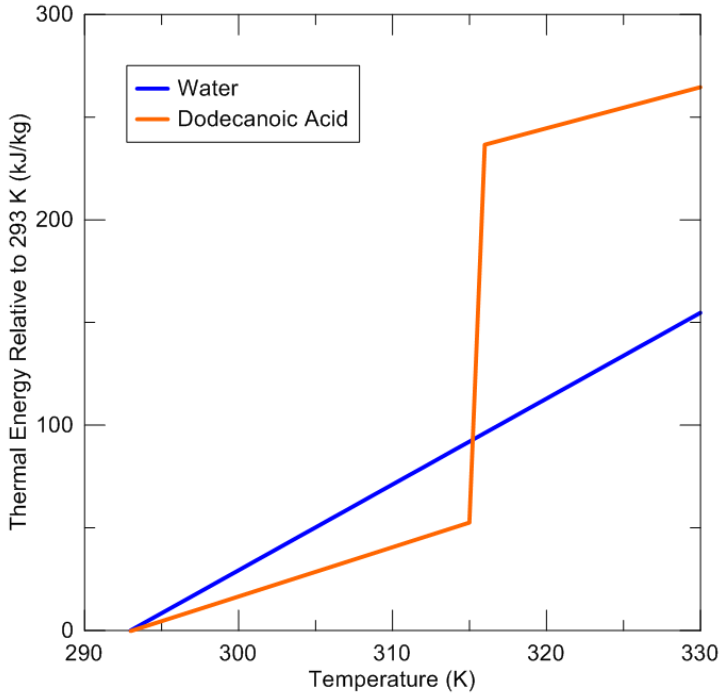

Figure 1.1 shows a comparison between the thermal energy stored in water and in dodecanoic acid as they are heated up from a temperature of 20 °C (293 K) up to 330 K. Dodecanoic acid melts at 42.5 °C (315.5 K) and has a latent heat of 182 kJ/kg, resulting in a large step increase of energy required to bring the temperature past the melting point (Desgrosseilliers *et al.*, 2013).

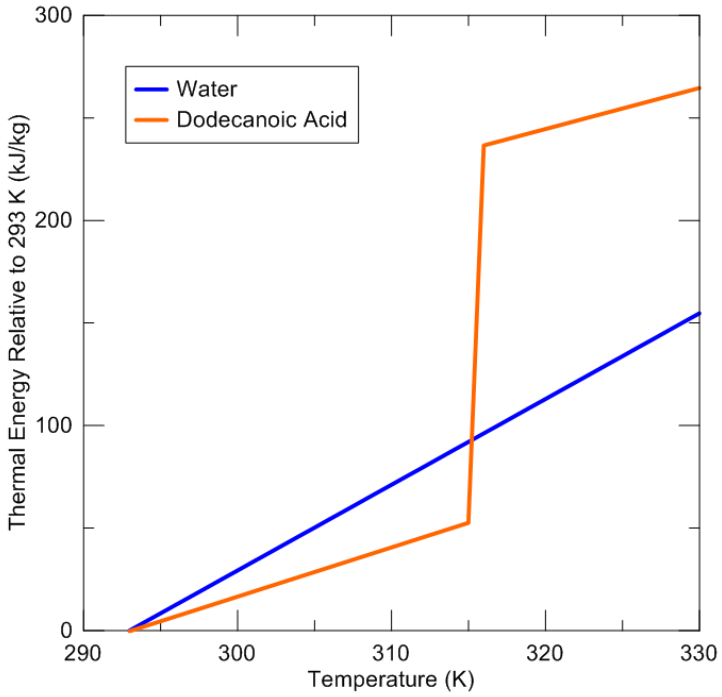

Figure 1.1: Thermal energy stored in water compared to dodecanoic acid relative to ambient temperature of 293 K

This step increase associated with the phase change represents a dramatic increase in energy storage density over the sensible heat storage on either side. The phase change process is also a nearly isothermal one, meaning that the quality of the heat does not decline as energy is removed from the system. So long as the system temperature cycles above and below the melting temperature of the selected material, the system can benefit from these improvements in energy density and quality.

There are two main issues facing the integration of phase change materials (PCMs) into thermal storage systems. One is the "rate problem", whereby most materials that have high latent heats also have low thermal conductivities. The low thermal conductivities limit the rate of heat transfer within the PCM, greatly increasing the time required to store and retrieve thermal energy (Groulx *et al.*, 2016). The second limitation is the lack of design equations for heat exchangers in contact with materials undergoing liquid-solid phase change. Heat exchanger design equations allow designers to estimate how a potential heat

exchanger will perform under different operating conditions based on the physical parameters of the design. Through these equations, such as the log-mean temperature difference (LMTD) method or the effectiveness-number of heat transfer units (ε-NTU) method, heat exchanger designers can identify optimal configurations based on the constraints of the application (Bergman *et al.*, 2011). These design equations, however, are intended for use with systems involving two moving fluids, or one moving fluid and a condensing or evaporating fluid. Thus, these design equations must be modified to account for a stationary medium with latent storage and variable thermophysical properties according to the phase.

1.2. Research Objectives

Energy is usually transferred between the PCM and the heat transfer fluid (HTF) via a heat exchanger, which generally includes finned surfaces to provide a larger surface area for heat transfer. There is a growing body of work on the topic of heat exchangers with fins that diverge from a main stem into smaller branch fins, much like the structure of a plant. These bio-inspired fin designs have been shown to offer superior rates of heat transfer compared to non-branched fins of equal volume when used to cool electronics (Park *et al.*, 2014). In terms of applications within LHESSs, there have been several numerical studies exploring various branching fin geometries to enhance heat transfer in PCM (Sciacovelli *et al.*, 2015; Ziaei *et al.*, 2015; Sheikholeslami *et al.*, 2016). There is little to no experimental work on branching fins within bodies of PCM, however, and additionally no works comparing branching fins to straight fins of equal surface area. Some guidelines as to the relative costs and benefits of branching fins compared to straight fins would be valuable to this field. In pursuit of that goal, the objective of this work is to experimentally compare a LHESS-based heat exchanger with bifurcated fins against heat exchangers with straight fins. To achieve this objective, the following sub-objectives were set for this project:

- Design and construct a new LHESSs testing platform for the Lab of Applied Multiphase Thermal Engineering (LAMTE) at Dalhousie University.

- Design and construct a PCM-based LHESS that can be used to test different fin geometries.
- Design and construct a set of bifurcating and straight fins of equivalent surface area, as well as a set of straight fins with equal mass to the bifurcating fins.
- Use the LHESS testing platform to experimentally examine the various fin types, outlining any differences in heat transfer mechanics between the two under various operating conditions.

1.3. Literature Review

1.3.1. PCM Categories

In practice, any material that changes phase at an application-appropriate temperature and has a comparatively high latent heat of fusion can be defined as a phase change material. PCMs can be divided into two main categories, organic and inorganic (Zalba *et al.*, 2003). Organic PCMs are composed of organic molecules, which are relatively large at the molecular scale and are built primarily from carbon, oxygen, and hydrogen atoms. Inorganic PCMs are those composed of non-organic molecules, with the main groupings being salt-hydrates and metallic PCMs (Sharma *et al.*, 2005).

Organic PCMs

Organic PCMs tend to take the form of waxy solids or liquids at room temperature and are mainly derived as by-products from the petrochemical and agricultural industries. When undergoing phase change from liquid to solid, most organic PCMs self-nucleate and exhibit little to no supercooling behaviour (Hasnain, 1998). This means that the liquid phase spontaneously forms crystals and solidifies at the freezing temperature, so that below this temperature there is no supercooled liquid remaining. Organic PCMs are also notable for their excellent chemical stability over many melt-freeze cycles, which allows them to be used for long periods of time and contributes to their cost-effectiveness and environmental sustainability (Kahwaji *et al.*, 2016; Sharma *et al.*, 2016). The two most common types of organic PCMs are paraffins and fatty acids. The paraffin family of organic molecules, characterized by their C_nH_{2n+2} structure, has a wide range of melting temperatures

depending on the length of the carbon chain, with each member also having a high latent heat (Sharma *et al.*, 2005). Paraffins are also relatively inexpensive and chemically compatible with common encapsulation materials, but can be flammable and thus may require additional safety precautions depending on the application (Sharma *et al.*, 2016). The fatty acid branch of organic PCMs have the form $CH_3(CH_2)_{2n}COOH$ and share many physical properties with paraffins (Sharma *et al.*, 2005). Fatty acids are generally less flammable than paraffins, but many are chemically incompatible with common plastics. Dodecanoic acid, a fatty acid with 12 carbon atoms, has particularly favourable properties for use in domestic solar-based LHESSs (Desgrosseilliers *et al.*, 2013). Also known as lauric acid, the material is derived from coconut or laurel oil and is commonly used as a food additive or as a component in soap-making. Dodecanoic acid has a melting temperature of 42.5 °C, which is ideal for domestic hot water systems where cold water below 20 °C is to be preheated with solar-sourced heat at 50-60 °C. In addition to its high latent heat and good chemical stability over many cycles, dodecanoic acid is food-safe and relatively inexpensive (Kahwaji *et al.*, 2017).

Inorganic PCMs

Any PCM which is not organic falls into the category of inorganic PCMs, resulting in an extremely broad spectrum of thermophysical properties. Salt compounds for use in concentrated solar plants, for example, have melting points between 120-220 °C. Most salt-hydrates, on the other hand, have melting temperatures between 8-89 °C, comparable to common organic PCMs (Pielichowska *et al.*, 2014). Salt-hydrates are formed when salt crystals incorporate water molecules into their lattices, such as in $CaCl_2 \cdot 12H_2O$. At elevated temperatures, the water and salt molecules separate into a liquid mixture of the two components, a process equivalent to melting. Compared to organic PCMs, salt hydrates generally have higher thermal conductivities and latent heats, but have severe corrosivity issues towards most metals (Sharma *et al.*, 2009). Salt hydrate PCMs also display supercooling, where the solution will remain in liquid form below the freezing temperature, requiring manual nucleation to begin the solidification process (Desgrosseilliers, 2012).

1.3.2. Heat Transfer in Shell and Tube LHESSs

One of the most common heat exchanger types used in experimental studies of LHESSs is the shell and tube design, where one section of the volume is occupied by the PCM and the other by the HTF (Charach *et al.*, 1992; Longeon *et al.*, 2013). Figure 1.2 shows a diagram of a simple cylindrical shell and tube heat exchanger, with a single tube passing through a larger concentric shell.

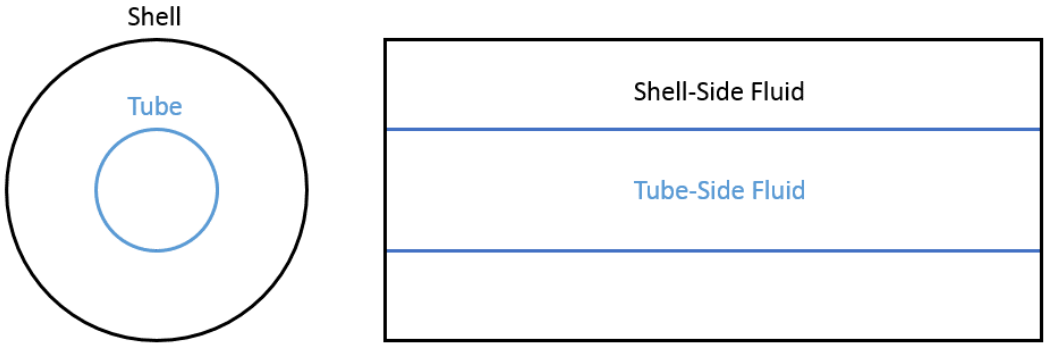

Figure 1.2: Diagram of a basic shell and tube architecture

There are many variations on this basic shell and tube architecture for increasing the rate of heat transfer between the two sides of the exchanger, such as:

- Multiple tubes within the shell (Arena *et al.*, 2015; Xiao *et al.*, 2015).
- Multiple passes of the tube through the shell (Castell *et al.*, 2008; Tay *et al.*, 2012; Hadiya *et al.*, 2016).
- Baffles within the shell or tube to increase the residence time and promote turbulence (Languri *et al.*, 2013).
- Non-circular cross-sections of the shell or tube (Kurnia *et al.*, 2013; Rouault *et al.*, 2014; Darzi *et al.*, 2016).
- Fins and other extended surfaces projecting from the shell or tube to increase the surface area (Sugawara *et al.*, 2011; Chiu *et al.*, 2012; Al-Abidi *et al.*, 2013; Paria *et al.*, 2015; Merlin *et al.*, 2016).

Charging and Discharging

There are two distinct modes of heat transfer within a LHESSs, depending on whether it is being charged or discharged. During charging, energy is added to the system by the HTF, which enters the heat exchanger at a temperature greater than the PCM melting temperature. Heat is transferred into the PCM in three stages; the first sensible, then latent, and then second sensible. During the first sensible stage, the initially solid PCM warms up until its temperature approaches the melting temperature, at which point the latent stage begins. During the latent phase, energy added to the system allows the PCM to transition from solid to liquid, with a front of molten PCM progressing from the heated surfaces. The second sensible stage begins when all the PCM has melted, meaning that additional thermal energy added to the system will increase the overall temperature of the PCM. During discharge the reverse occurs, as cold HTF passes through the heat exchanger and absorbs energy from the PCM, causing the PCM to cool down and resolidify.

Experimental studies have shown that during charging, natural convection within the molten PCM plays a significant role in the heat transfer between the HTF and the remaining solid PCM (Castell *et al.*, 2008; Longeon *et al.*, 2013; Kamkari *et al.*, 2014; Liu *et al.*, 2014; Murray *et al.*, 2014; Merlin *et al.*, 2016). Natural convection in the liquid PCM also causes the melting front to move from the top of the system to the bottom, and can cause thermoclines to appear within the liquid PCM (Longeon *et al.*, 2013). Numerical work has shown that increasing the contact area between the HTF pipe and the molten PCM increases the overall heat transfer rate (Belusko *et al.*, 2016). The same studies show that natural convection has a greatly reduced impact on the transfer of heat between the HTF and the PCM during discharge. The PCM around the cooled surface tends to solidify first, forming a layer of solid PCM that insulates the heat transfer surface from the remainder of the liquid PCM.

HTF Flow Rate

Increasing the flow rate of the HTF results in an improved rate of heat transfer within the LHESS by reducing the thermal resistance on the HTF side of the heat exchanger. Reducing the resistance of the HTF has a relatively minor effect on the overall rate of heat transfer, however, as the resistance on the PCM-side is usually much more significant

(Medrano *et al.*, 2009). During discharge, the increased thermal resistance from the solid PCM further reduces the impact of HTF flow rate on the overall heat transfer rate (Sarı *et al.*, 2002; Medrano *et al.*, 2009; Liu *et al.*, 2014; Murray *et al.*, 2014; Rahimi *et al.*, 2014).

1.3.3. LHESSs Evaluation by ε-NTU Methods

To compare and select the most appropriate heat exchanger geometries, designers make use of mathematical tools such as the log-mean temperature difference (LMTD) and effectiveness-number of transfer units (ε-NTU). These methods, however, are built on the premise that both sides of the heat exchanger are filled with moving fluids. If one side is filled with a stationary body, such as PCM in the solid phase, it is necessary to adjust the method to preserve it as a meaningful tool for comparison.

One approach for adapting the ε-NTU method is to consider only the latent portion of the heat exchange process, as most of the energy is transferred during this stage. During the latent stage, the HTF transfers energy to a body at constant temperature, thus the maximum rate of heat transfer occurs when the HTF streams leaves at the PCM temperature. Based on this assumption, an expression for effectiveness can be described by Eq. (1.1) (Ismail *et al.*, 1993; Tay *et al.*, 2012).

$$\varepsilon = \frac{T_{in} - T_{out}}{T_{in} - T_{PCM}} \tag{1.1}$$

The term ε is the effectiveness of the system, T_{in} and T_{out} are the inlet and outlet temperatures of the HTF, and T_{PCM} is the melting temperature of the PCM. Since the outlet HTF temperature will change over time as the PCM charges or discharges, the effectiveness is presented as an average over the entire charging or discharging process.

There have also been empirical correlations developed for the effectiveness based on specific experimental geometries. Amin *et al.* (2012), for example, presents effectiveness plots generated from experiments performed on a shell and tube exchanger filled with 7.4 cm diameter capsules of PCM. The correlations are functions of the mass flow rate, and are given for charging and discharging modes. For both modes, the effectiveness decreased as mass flow rate increased, due to the reduced residence time of the HTF (Amin *et al.*, 2012; Amin *et al.*, 2014). Similar approaches have been presented for tubes with annular fins (Tay *et al.*, 2014).

1.3.4. Impact of Extended Surfaces on LHESS Performance

A basic technique for improving the effectiveness of a heat exchanger is to increase the available surface area for heat transfer. This is most commonly achieved by adding fins, also known as extended surfaces, to the interface between the hot and cold sides of the exchanger. Fins are usually only placed on the PCM side of the exchanger, as placing fins on the HTF side will increase the pressure difference required to circulate the fluid. Inserting fins into the PCM side, however, comes at the cost of removing some of the PCM to make space, thus reducing the overall heat storage capacity of the LHESS. Thus, it is in the interest of the LHESS designer to achieve the greatest improvement in heat transfer using the minimum amount of extra non-PCM material. As a result, there is a large and expanding body of literature on experimental and numerical studies exploring the consequences of using various types and arrangements of fins within LHESSs.

Fin Geometries

The work of Ismail *et al.* (2001) serves as a standout parametric experimental study on the effects of fin geometries on the performance of a shell and tube based LHESS. It is shown that increases to the fin length, thickness, and number of fins all reduce the solidification time of the system, albeit with diminishing returns. In addition, increasing the fin thickness was shown to have a relatively minor effect on the solidification time compared to changes in the number and length of fins (Ismail *et al.*, 2001). Other experimental studies have also shown that increasing the fin thickness has a relatively minor effect on the rate of heat transfer, as very little surface area is added for a given change in thickness (Al-Abidi *et al.*, 2013; Paria *et al.*, 2015).

Concerning fin shapes, comparisons have been performed on the relative merits of pin-shaped and flat rectangular fins. It has been shown that for fins of equal volume, rectangular fins provide greater rates of heat transfer than pin fins due to their greater surface area (Baby *et al.*, 2012; Tay *et al.*, 2013). Certain orientations of flat fins can, however, impede the natural convection motion of the molten PCM and thus negatively impact the rate of heat transfer. In a vertical shell and tube heat exchanger, for example, longitudinal fins performed better than annular fins in terms of heat transfer, as the longitudinal fins allowed

fluid PCM to circulate up and down the length of the shell (Agyenim *et al.*, 2009). Likewise, in a horizontal shell and tube exchanger, angling longitudinal fins so that molten PCM may circulate from the bottom half to the upper half promotes natural convection and thus increases the overall rate of heat transfer (Liu *et al.*, 2014).

Branching fin designs

The practice of bio-inspired design involved examining structures and systems present in nature to gain insight into technological design problems. Regarding heat transfer via finned surfaces, researchers and designers have looked to circulatory systems as an example of highly efficient transport geometries. Analysis of the similarities between mass flow in natural structures, such as in plants, and the flow of heat from a point source through a medium has sparked a field of research into branching fin designs. Bejan (1997) described an analytical method for designing root-like system of cooling fins embedded into a heat-generating volume representing a computer chip. The method allocated a certain volume of conductive fin material within the chip to minimize the temperature difference between the chip and the fin. Bejan branded this type design as an application of his "*constructal theory*", a subset of bio-inspired design pertaining specifically to flow systems. Other algorithms have since been designed for a wide variety of fin structures protruding into single-phase media similar to computer chips. The works of Almogbel (2005), Yu *et al.* (2006), Lorenzini *et al.* (2011), for example, all considered cases of two-dimensional conduction heat transfer, where fins of a fixed volume are permutated into right-angled fractal designs, as shown in Figure 1.3.

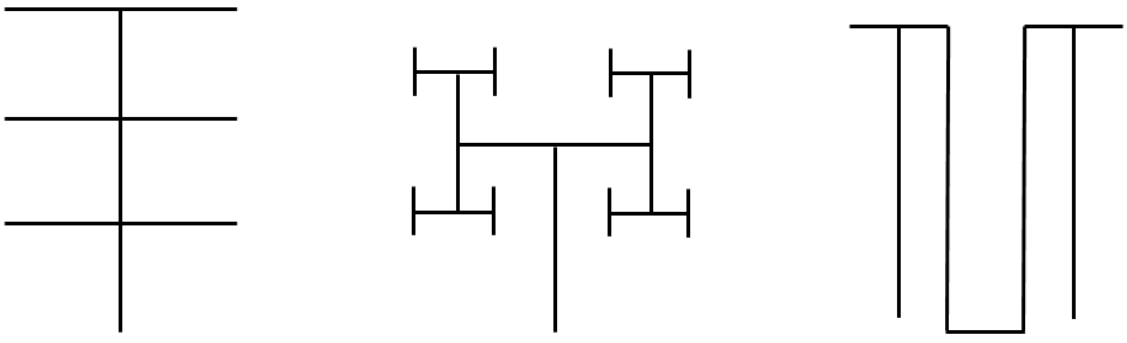

Figure 1.3: Fin geometries examined by Almogbel (2005), Yu *et al*. (2006) and Lorenzini *et al.* (2011) from left to right respectively.

In all three cases, it was found that longer and more complex fins resulted in decreased thermal resistance, but that the improvements diminished with greater complexity levels. In addition, for a given maximum fin volume it was show that an optimal combination of geometrical parameters for minimizing thermal resistance existed (Almogbel, 2005; Yu *et al.*, 2006; Lorenzini *et al.*, 2011). In the case described by Almogbel (2005), for example, a single optimal fin branch to fin thickness ratio can be found for a given fin volume, heat transfer coefficient, number of branches, and branch to stem length ratio.

Y-fins

In addition to right-angled fins, there have been numerical studies published on fins with one or two levels of branching at various angles. Lorenzini *et al.* (2006) examined the case of a fin branching once, forming a Y-shaped design. It was determined that for a given fin volume, dimensionless heat transfer rate, stem to branch length ratio, and stem to branch thickness ratio, there was a single optimal angle of bifurcation. In addition, it was shown that branches at right angles to the stem forming a T-shaped fin always had a greater thermal resistance than the Y-shaped ones (Lorenzini *et al.*, 2006). Calamas *et al.* (2013) numerically compared Y-shaped fins with three levels of branching to non-branching rectangular fins of equivalent volume. It is reported that the Y-shaped fins showed superior fin efficiencies compared to the rectangular fins. In addition, for the Y-shaped fins, bifurcation angles of 45° from the stem, and stem to branch thickness ratios of 1.68:1 provided the greatest fin efficiencies of those tested (Calamas *et al.*, 2013).

Bonjour *et al.* (2004) and Kim (2014) numerically examined the performances of Y-shaped fins transferring heat from a moving fluid to a heat sink. Bonjour *et al.* (2004) concluded that for a given set of boundary conditions, bifurcated fins performed better than straight fins when the radius of the heat exchanger exceeded a specific limit. Kim (2014) concluded that there existed branching geometries that provided greater rates of heat transfer than straight fins of equal cross-sectional area, but that the improvements diminished as the residence time of the fluid increased.

Branching Fins in PCM

Some studies have considered the application of branching fins specifically in LHESSs, with the fins embedded into the PCM side of the heat exchanger. Figure 1.4 shows the design presented by Sciacovelli *et al.* (2015) in their numerical study of a shell and tube exchanger with longitudinal fins. Four straight longitudinal fins were compared to branching longitudinal fins designed by an optimization algorithm. The performances were described in terms of exchanger efficiency, defined as the percentage of the total stored energy extracted in a given time. It was found that longitudinal fins with a single level of bifurcation provided a 6 to 9% increase in efficiency over straight fins, while fins that bifurcate twice along their length improved efficiency by 24%. It was also noted that the optimal angle between the branched fins depended on the fraction of molten PCM, thus each branch angle provided a peak efficiency improvement at a specific stage of the charging process (Sciacovelli *et al.*, 2015).

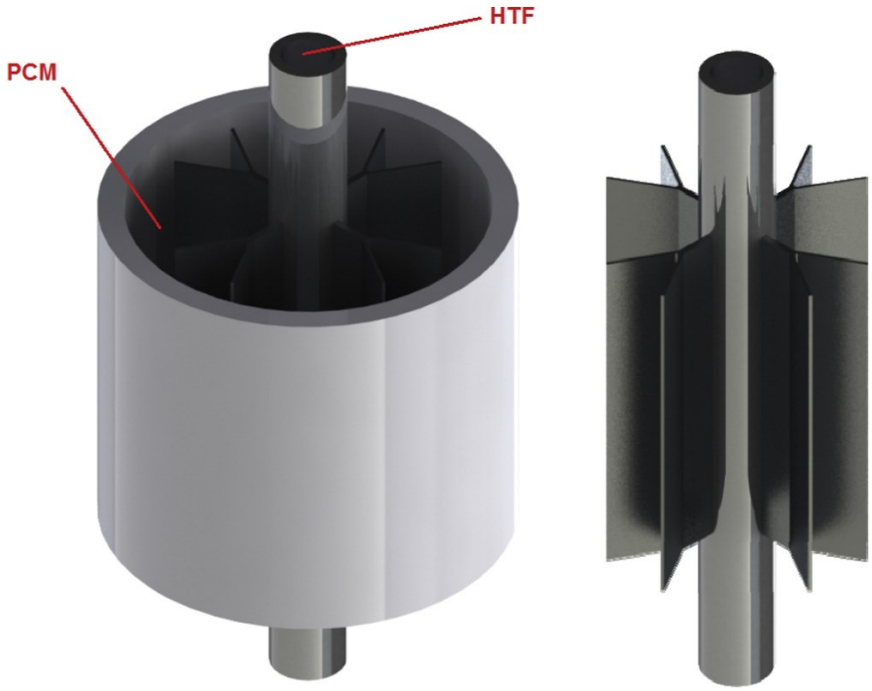

Figure 1.4: Bifurcating heat exchanger design of (Sciacovelli *et al.*, 2015)[1]

[1] Reprinted from Applied Energy, Volume 137, Sciacovelli, A., Gagliardi, F., & Verda, V., Maximization of performance of a PCM latent heat storage system with innovative fins, 707-715, Copyright (2015), with permission from Elsevier.

Another study presented by Pizzolato *et al.* (2017) expanded on the previous work of Sciacovelli *et al.* (2015), demonstrating an algorithm for generating branching finned structures with shell and tube LHESSs. The algorithm was designed to provide the optimal fins shape for delivering a specified percentage of the stored energy within a time limit. For high energy demands, the algorithm preferred shorter and thicker fins with fewer branches. If long time periods are chosen for a given energy demand, the fins become thinner at the base and at the intersections of branches so as to provide thermal chokepoints (Pizzolato *et al.*, 2017). In branching fin studies, it is more common to see fins that have varying thicknesses along their length. Usually the base of the fin is the thickest section and then at each branching point the fin thickness is divided between the branches. Other designs do not reduce the fin thickness at the branching points, such as those presented by Sheikholeslami *et al.* (2016) and Eslami *et al.* (2017).

Figure 1.5 shows the design examined by Sheikholeslami *et al.* (2016) in a numerical study on a tube fitted with four longitudinal fins projecting into a body of PCM. The rectangular fins were compared to four branching fins with two bifurcation points along their length. The resulting design had a snowflake-like arrangement with the same cross-sectional area as the original straight fins. The authors reported a 50% decrease in solidification time when using the branching fins and an 87% decrease over the case with no fins at all (Sheikholeslami *et al.*, 2016).

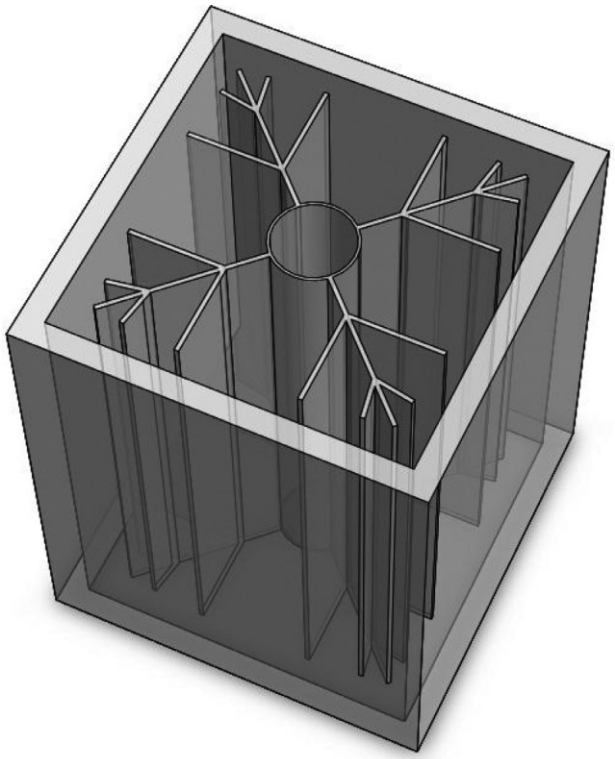

Figure 1.5: Snowflake heat exchanger of (Sheikholeslami *et al.*, 2016)[2]

Eslami *et al.* (2017) also discussed a 2D numerical model, but one that is axisymmetric with a fin branching out from the origin-point along the axis of rotation. Figure 1.6 shows the three models discussed by the authors; a straight fin, an angled fin forming a 'V', and an angled fin that straightens out to form a "*pencil shape"*. The V-shaped fin provided a 25% reduction in discharge time, and the pencil-shaped fin provided a 38% reduction compared to the straight fin. During charging, use of the two angled fin types resulted in a greater liquid fraction of PCM during the run, but the time for complete melting was the same for all three fins. The convergent melting times is explained by the presence of natural convection, which significantly increases the rate of heat transfer and thus masks the advantages of the branched fins at conducting heat (Eslami *et al.*, 2017). It is especially valuable to have studies that examine fin performance during both charging and discharging modes due to the different types of heat transfer present during each mode.

2 Reprinted from Journal of the Taiwan Institute of Chemical Engineers, Volume 67, Sheikholeslami, M., Lohrasbi, S., Ganji, D. D., Response surface method optimization of innovative fin structure for expediting discharging process in latent heat thermal energy storage system containing nano-enhanced phase change material, 115-125, Copyright (2016), with permission from Elsevier.

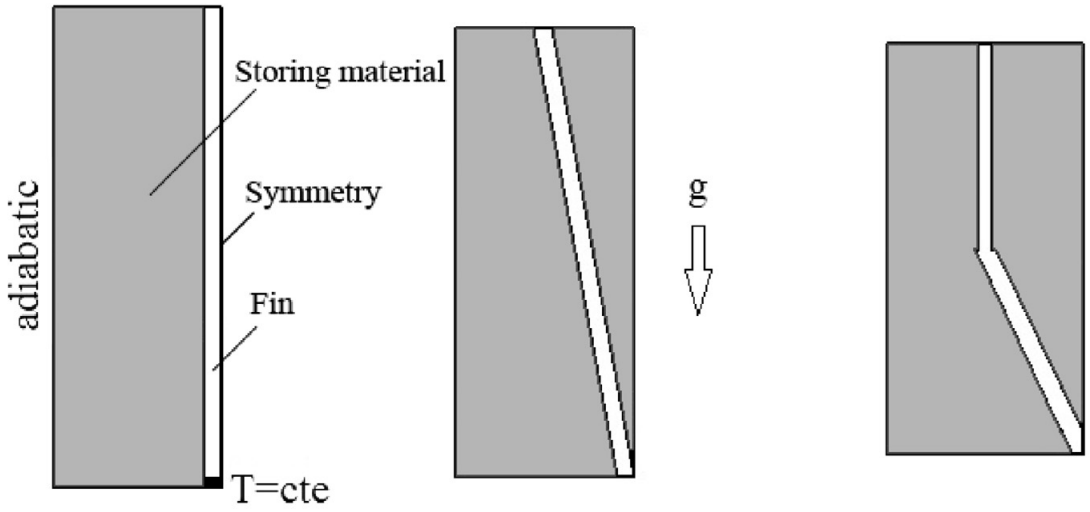

Figure 1.6: 2D axisymmetric fin designs of (Eslami *et al.*, 2017)[3]

There are also more abstract studies, which numerically examined heat transfer paths that dynamically grow and branch off into the PCM body during the study. Ziaei *et al.* (2015) considered a two-dimensional line heat source growing into a square of PCM, splitting into two branches at the halfway point along the PCM. It was determined that a branch angle of 155° resulted in the lowest melting time. The same authors then considered a three-dimensional version of a similar problem, with a line growing into a cylindrical volume and then branching into three equidistant lines. During the later study, it was shown that the angle of the branches in the longitudinal direction had a minimal impact on the melting time (Ziaei *et al.*, 2016).

Based on the available literature, it appears that branching fin designs provide a definite heat transfer advantage compared to straight fins during discharge; when conduction is the main mode of heat transfer (Sciacovelli *et al.*, 2015; Sheikholeslami *et al.*, 2016; Eslami *et al.*, 2017). Few papers, however, consider the differences in fin performance during melting, when natural convection plays a major role in heat transfer within the LHESSs.

[3] Reprinted from International Journal of Hydrogen Energy, Volume 42, Issue 28, Eslami, M., Bahrami, M. A., Sensible and latent thermal energy storage with constructal fins, 17681-17691, Copyright (2017), with permission from Elsevier.

Most studies compare branched fins to straight ones with equal cross-sectional area, holding fin volume constant so that the discharging time may be used as a metric of performance. For fins of equal volume, branching fins will have a greater surface area, so the comparison is usually skewed in favour of the branched fins. It would therefore be of interest to compare straight and branching geometries for fins of equal surface area, so that the change in geometry is the main variable affecting the rate of heat transfer. There is also a lack of studies in the literature examining the effectiveness of bifurcating fins experimentally. Potentially one of the only experimental studies performed on a branching fin heat exchanger is that of Park *et al.* (2014), which does not involve any PCM. The authors described a cylindrical heat exchanger with Y-shaped fins intended for cooling electronics via natural convection compared to a heat exchanger with straight fins of equal cross-sectional area. Thus, there is a need for an experimental study on branching fins used to charge and discharge PCM in a LHESS.

Parameters of Performance

There is currently no standard for testing the performance of finned heat exchangers used in PCM applications, resulting in a wide variety of metrics. Medrano *et al.* (2009), for example, reported that the addition of annular fins to a shell and tube LHESS improved the rate of heat transfer by 50-100 W compared to the case of the unfinned tube. Rathod *et al.* (2015), while discussing the addition of three longitudinal fins to a heat exchanger, describes the impact in terms of a 24% reduction in PCM melting time and a 43% reduction in solidification time. Merlin *et al.* (2016), also describing the effects of incorporating annular fins along a heat exchanger, reported a 400% increase in the "heat transfer coefficient" as described in Eq. (1.2),

$$\text{Heat Transfer Coefficient} = \frac{\dot{q}}{A\Delta T} \tag{1.2}$$

where $\dot{q}$ is the rate of heat transfer, A is the surface area of the heat exchanger, and ΔT is the temperature difference of the HTF between the system inlet and outlet. These three similar studies highlight the difficulty in comparing heat exchanger improvements when they are measured using different metrics. Furthermore, use of melting times or heat transfer coefficients to compare heat exchangers can lead to unintuitive conclusions. Charging and solidification times can be a convenient proxy for heat exchanger

effectiveness, as they are relatively simple to measure and provide a single scalar value to compare against. While melting time can be reduced by increasing the rate of heat transfer, it is also reduced by any changes that diminish the total volume of PCM in the system, and therefore the energy storage capacity. Thus, lowered melting time can represent both an improvement and a decrease in LHESS performance. The heat transfer coefficient likewise allows for simpler comparisons between exchangers through normalization by the heat transfer area and HTF temperatures. This normalization does not, however, account for the heat exchanger volume, and thus the loss of PCM storage capacity. As a result, Medrano *et al.* (2009) and Merlin *et al.* (2016) each conclude that absorbing PCM into porous graphite and placing the resultant composite into the heat exchanger provides the greatest normalized thermal power. In the experiment described by Merlin *et al.* (2016), use of the graphite-PCM composite improved the normalized thermal power by over 800% compared to the case with a bare copper tube embedded into the PCM. The graphite, however, occupied more than 50% of the volume previously occupied by the PCM, resulting in an equivalent loss of energy storage capacity.

Chapter 2. EXPERIMENTAL GEOMETRY

2.1. Mobile Testing Bench

A mobile testing bench was designed and constructed to facilitate the experimental work of this study as well as future studies conducted at the LAMTE. The requirements of the testing bench were as follows:

- The bench must have sufficient workspace to comfortably hold an experimental LHESS. The maximum footprint for such an experiment is 60 cm by 60 cm, and could be up to 60 cm tall.
- The bench must have a heater and chiller for controlling the temperature of a heat transfer fluid (HTF), such as water.
- The bench must include appropriate pumps and piping to circulate the HTF through the experiment.
- The bench must include sensors for measuring temperature, HTF flow rate, and the pressure differential across the experimental setup.
- The bench must be mobile so that it can be easily moved around the LAMTE.

Figure 2.1 shows a schematic view of the testing bench, detailing the HTF flow from either the hot or cold-water tank through the PCM-based LHESS. Temperature sensors are incorporated into the pipes to measure the change in HTF temperature between the inlet and outlet of the LHESS, as well as within the PCM. In addition, the volumetric flow rate of the HTF and the pressure drop in the HTF across the LHESS are measured with appropriate sensors. All of the sensor readings are collected by a single data acquisition system (DAQ), which is controlled by a LABVIEW user interface on a nearby computer.

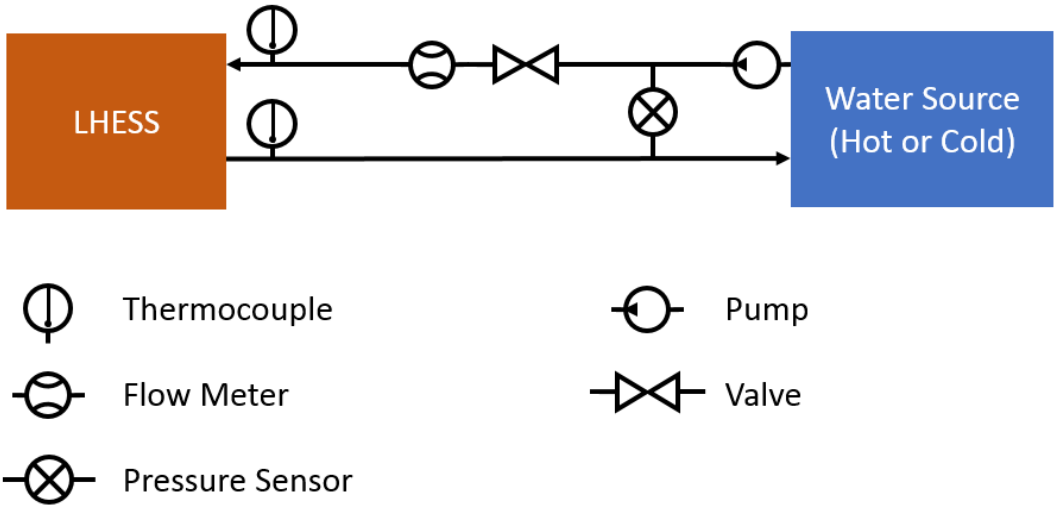

Figure 2.1: Schematic of experimental setup

Figure 2.2 shows the computer aided design (CAD) assembly of the test bench concept as well as a picture of the completed design.

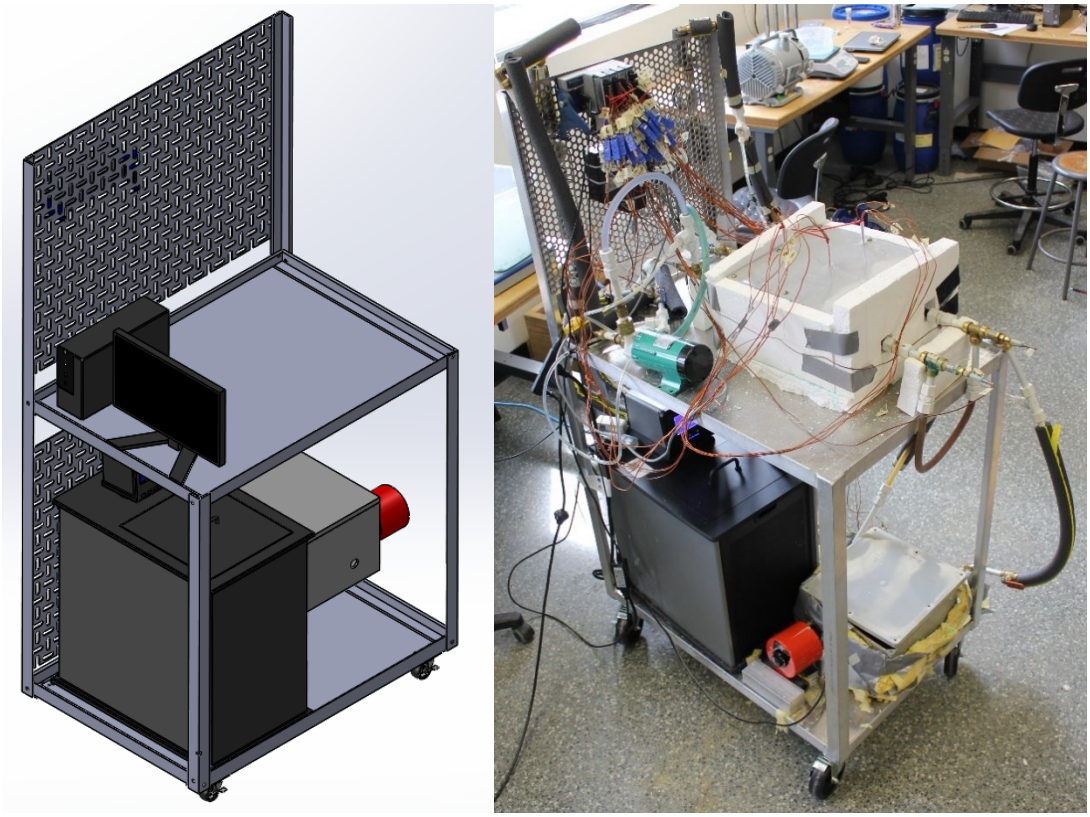

Figure 2.2: CAD model of test bench concept (left) and photograph of the constructed bench (right)

2.1.1. Heat Transfer Fluid Temperature Control and Circulation

The hot and cold-water loops each have their own temperature management and pumping systems, which allows them to be run simultaneously if necessary. Figure 2.3 shows the hot-water bath and the attached 500 W electric immersion heater with built-in temperature control (TEMPCO model TSP02793). To mitigate heat loss, the water storage container is wrapped with insulation that is not shown in the figure.

Figure 2.3: Water Heating Unit

Figure 2.4 shows the circulating bath used to provide cold water to the experimental setup. The Cole-Parmer Polystat RK-12122-52 model has a cooling capacity of 800 W at 20 °C, and is also able to provide hot water using a 1200 W heater. The bath has a built-in pump that can maintain a maximum flow rate of 17.0 liters per minute.

Figure 2.4: Cole-Parmer Polystat RK-12122-52 15L 230 V circulating bath

An Iwaki MD-30RT-115NL centrifugal pump (Cole Parmer model EW-72012-10) is used to pump the water in the hot loop. See Appendix A for the associated pump curves.

Figure 2.5: Picture of an Iwaki MD-30RT-115NL pump

2.1.2. Sensors

Temperature

Temperature data was sampled at the HTF inlet and outlet using T-type thermocouple wires, attached to a National Instruments NI 9213 DAQ card. See Appendix A for the data sheets of the thermocouples and DAQ card. Figure 2.6 shows one of the T-type probes, sheathed in a 1/16-inch diameter cladding.

Figure 2.6: Photograph of a T-type thermocouple probe with special limits of error

In addition, three K-type thermocouple probes were used to measure the temperature of the PCM along the length of the experimental geometry. Figure 2.7 shows one of the K-type probes, clad in a 1/8-inch diameter cladding.

Figure 2.7: K-type thermocouple probe

The rigid cladding ensures that the thermocouple remained in the same location between tests. Although less accurate than T-type probes, the K-type thermocouples were readily available in the LAMTE at the time of testing.

Volumetric Flow Rate

The flow rate of the heat transfer fluid was measured using two Omega brand model FTB 4605 turbine meters, one of which is shown in Figure 2.8. These meters are connected in-line with the fluid flow, which causes an internal turbine to rotate and trigger a current

pulse from a hall-effect sensor. The rate and number of pulse accumulations can be correlated with the rate and volume of flow over a given time. The current pulses pass through a step-up resistor as described in Appendix A and are then routed to a NI 9435 module attached to the NI-cDAQ 9174 National Instruments data acquisition system. The measurement uncertainty of the flowmeter in operation is ± 2% of the output.

Figure 2.8: Photograph of a FTB 4605 Flow Meter

As per the operating manual, the FTB 4605 flow meter outputs 40 pulses per liter of flow. To verify the pulse per liter output, each flow meter was connected to the circulating bath and water was discharged through the meters at a constant flow rate and temperature. The discharged water was collected and then weighed on a Cole-Parmer Symmetry model scale with 0.1 g precision. This process was repeated eleven times for each flow sensor. The density of the water was determined according to its temperature, which was measured with a submerged T-type thermocouple as well as by the circulating bath. For all trials, the recorded water temperature was 23.0 °C with variations of only 0.1 °C due to the controlled environment of the circulating bath. The resulting flow calibration constants for the two flow meters was determined to be 39.81 and 46.31 pulses per liter. The LABVIEW data acquisition program uses these calibration constants to output a flow rate figure for each metering device.

Pressure

The pressure drop across each side of the system is measured with an OMEGA brand PX26 pressure transducer, shown in Figure 2.9.

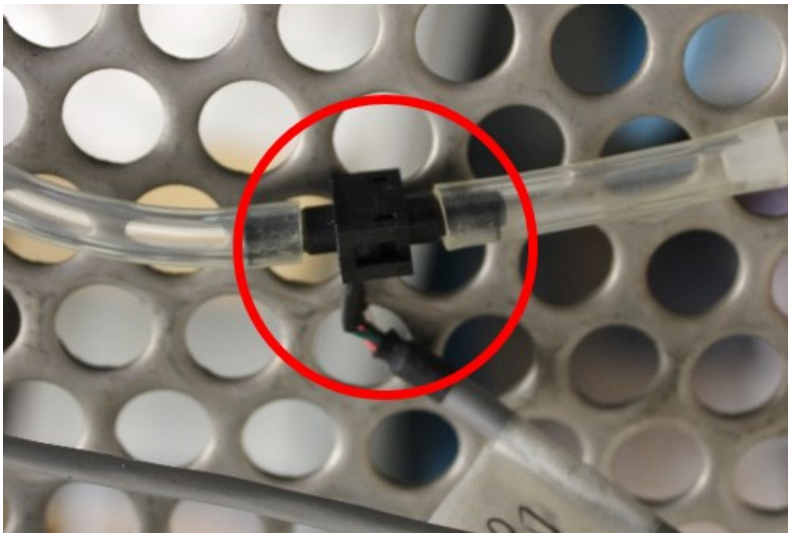

Figure 2.9: Photograph of a PX26 Differential Pressure Sensor and Connecting Tubes

In the setup, tubes branch off the main water-flow lines on either side of the heat-storage device that is to be tested and connect to the two inputs on the pressure sensor. The deflection of a small membrane within the sensor due to relative pressure differences between the inputs is expressed as a potential difference that is picked up by the NI-DAQ NI 9219 card. This voltage signal is multiplied by a gain to give a pressure value in pascals.

2.1.3. Data Acquisition Tools

Signals from the measurement sensors are processed and logged on the computer with the aid of a National Instruments data acquisition system, model NI-cDAQ 9174, as shown in Figure 2.10. This cDAQ model has four slots that may be filled by NI modules, which serve as connection ports for the measurement sensors. Thermocouples are connected to a NI 9213 module, which provides the cold junction compensation required for taking temperature readings. The flow sensors are connected to a NI 9435 module, intended for digital inputs. Whenever a voltage or current input passes over a specified threshold, the NI 9435 module outputs a digital ON signal. A pulse input, such as that produced by the flow sensors, is thus converted to a series of digital ON signals that the computer keeps a running count of. The pressure sensors connect to a NI 9219 module, a universal analog input device that picks up the voltage excitation.

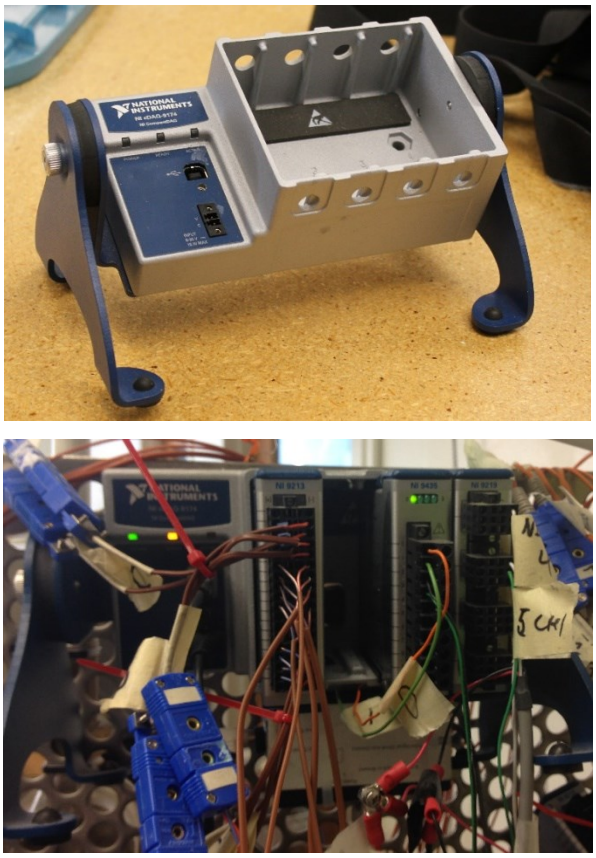

Figure 2.10: Photographs of empty NI-cDAQ 9174 unit (left) and NI-cDAQ mounted to test bench and filled with modules (right)

The reading and logging of the sensor signals is controlled by LABVIEW 15.0 software, which is designed for use with the NI-cDAQ system. The LABVIEW software allows for preprocessing of the signals, such as converting pulses counted by the flow meter into a volume measurement, and is also used to display the sensor outputs in real time.

2.2. Experimental Geometry

There are relatively few experimental studies on heat exchangers using bifurcated fins to enhance the heat transfer rate within a LHESS. Therefore, it would be of value to experimentally compare a heat exchanger with bifurcated fins to one with straight fins. The goal of this study is to explore the impact that bending a straight fin into a Y-shape has on the rate of heat transfer between a HTF and a mass of PCM. To isolate the effect of fin

geometry on the rate of heat transfer, the bifurcated fin and the straight fin were designed to have the same amount of surface area in contact with the PCM as the bifurcated fin.

Figure 2.11 shows a bifurcated fin folded from a single sheet of copper. The original copper sheet was 304.8 mm long (12 in), 76.2 mm wide (3 in) and 0.61 mm thick (0.024 in). The folded fin has a straight section 76.2 mm long (3 in) and then a Y-shaped bifurcation on each end. The angle of the bifurcation is 45 ° from the horizontal, resulting in a 90° split.

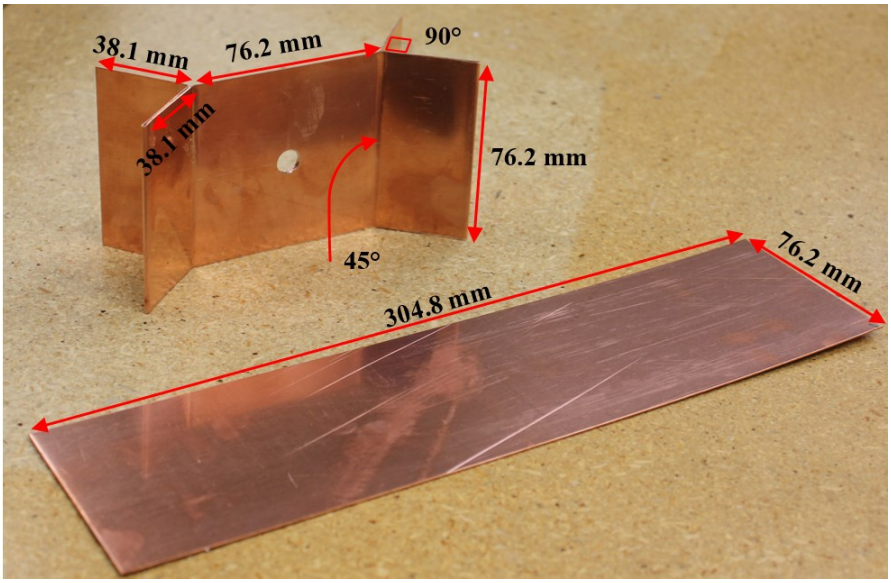

Figure 2.11: Photograph of bifurcated fin folded from a copper sheet

Figure 2.12 shows four of the bifurcated fins soldered onto a ¼ - inch nominal copper pipe with outer diameter of 9.525 mm (0.375 in) and inside diameter of 7.899 mm (0.311 in). The total mass of the heat exchanger is 1.3 kg, which contributes a relatively small 0.5 kJ/K of energy storage to the system due to its heat capacity.

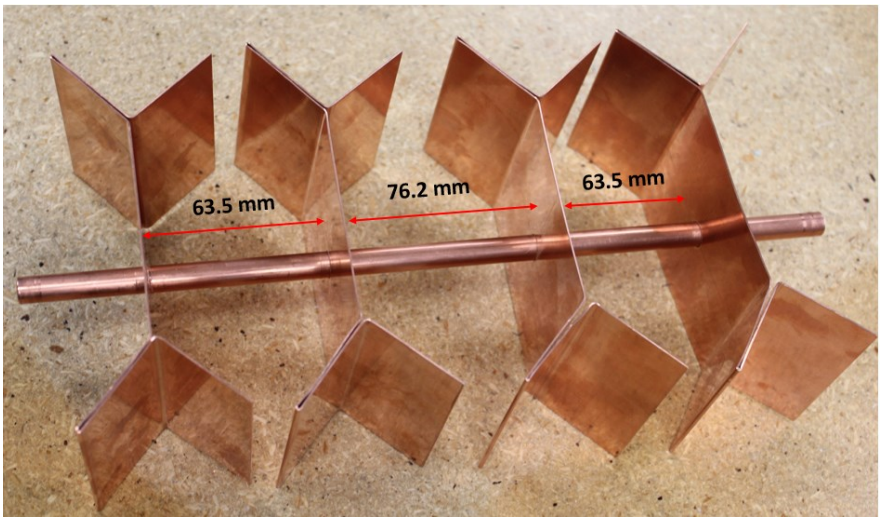

Figure 2.12: Photograph of bifurcated fins mounted onto copper pipe

The folding process used to construct the bifurcated fin results in some of the original surface area being lost, as the sheet must be folded back onto itself. Thus, to create a straight fin of equal surface area, the original sheet of copper was cut down to 228.6 mm (9 inches). The length of a fin can have a significant impact on the heat transfer rate in PCM, so to control this variable a third fin type of equal mass to the bifurcated fin is introduced. Figure 2.13 shows these two straight fins. The top fin has equivalent mass of 143 g to the bifurcated fin, being made from the same 304.8 mm by 76.2 mm sheet. The bottom fin has a surface area of 174.2 cm^2, equal to that of the bifurcated fin.

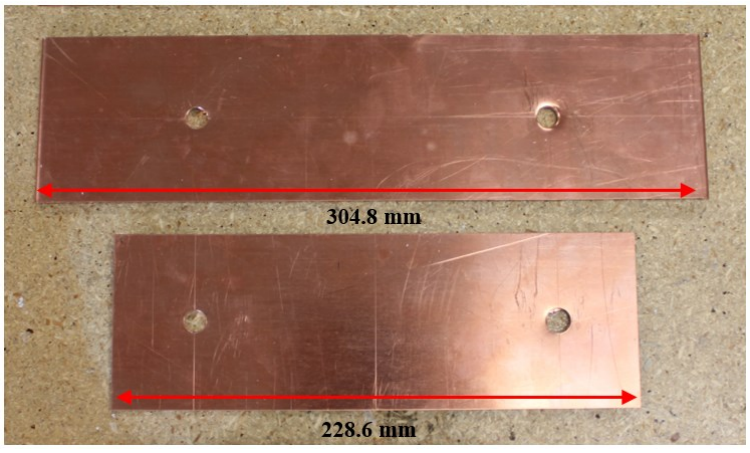

Figure 2.13: Photograph of straight fins of equal mass (top) and straight fin of equal surface area (bottom)

Figure 2.14 shows the fins of equal mass to the bifurcated ones, cut in half and mounted on copper pipes. The fins are spaced in increments of 3.175 cm (1.25 in.) and have been cut in half to facilitate installation and to prevent bending due to misalignment.

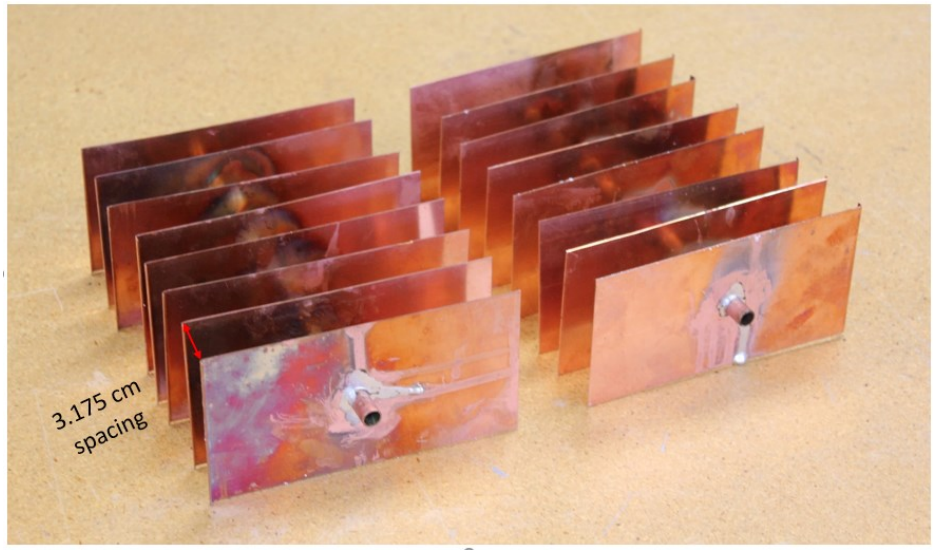

Figure 2.14: Photograph of straight fins of equivalent mass to bifurcated version mounted on pipes

Figure 2.15 shows the fins of equivalent surface area to the bifurcated ones, cut in half and then mounted onto the heat transfer pipe. Each pair of these straight fins have the same surface area as one of the bifurcated fins.

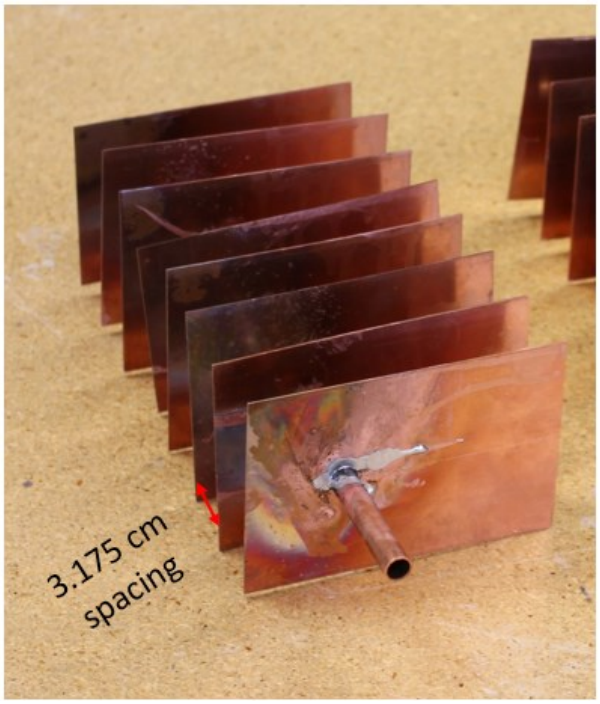

Figure 2.15: Photograph of straight fins of equivalent surface area to bifurcated version mounted on pipe

The LHESS used for this experiment is a box with interior side lengths of 303 mm (11.93 in) and a depth of 151 mm (5.95 in). Figure 2.16 shows the path of the HTF through the heat exchanger, as well as the placement of the thermocouples throughout the system. The three thermocouples embedded into the PCM are 6-inch probes (15.24 cm) and are inserted through the lid of the container so that the tip rests 1.5 cm above the container floor. Figure 2.17 shows the placement of the thermocouples relative to the straight-finned heat exchanger.

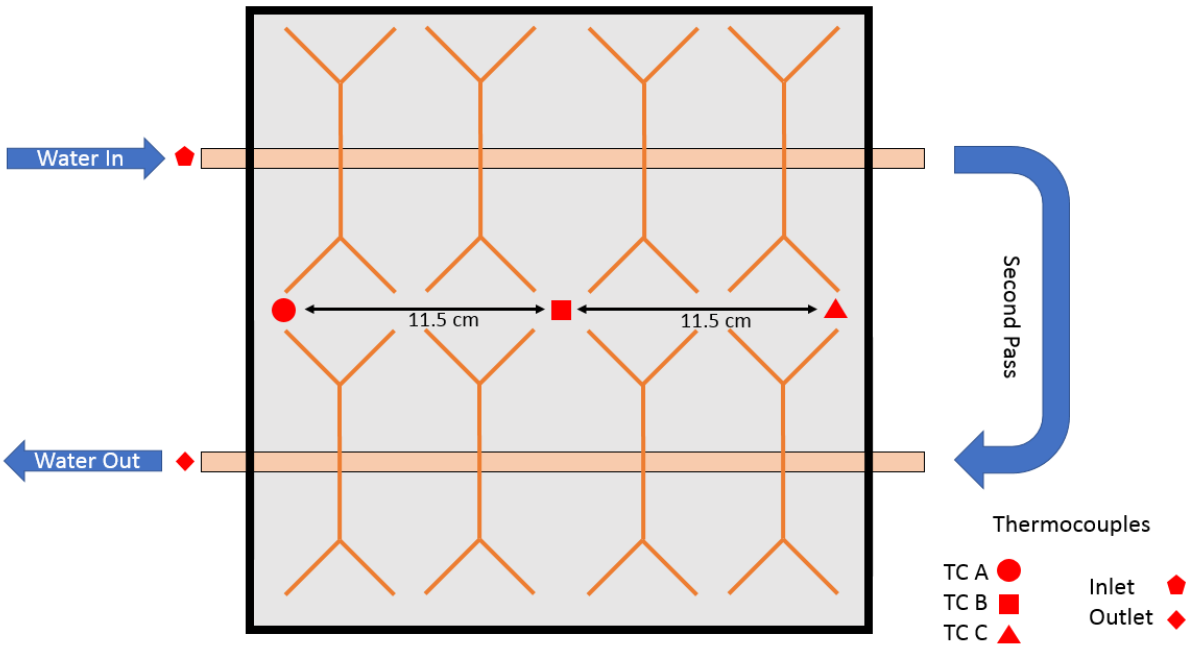

Figure 2.16: Diagram of HTF flow and thermocouple placement in heat exchanger

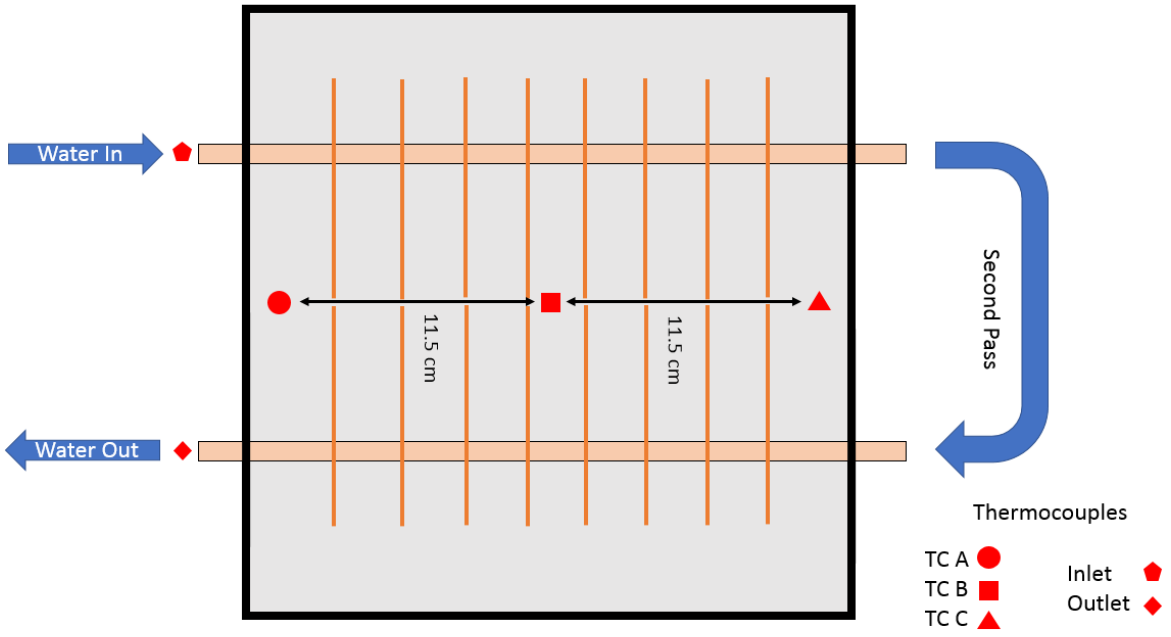

Figure 2.17: Diagram of thermocouple placement for straight-finned heat exchanger

The box was filled with the dodecanoic acid as the PCM, a food-grade additive derived from coconut oil and often used in soap manufacturing. Dodecanoic acid has a high latent heat and a melting temperature of 42.5 °C, making it ideal for solar thermal applications. Table 2.1 lists the thermophysical properties of lauric acid according to Yaws (1999) and the experimental work of Desgrosseilliers *et al.* (2013). The change of heat capacity of dodecanoic acid with temperature is also provided in Desgrosseilliers *et al.* (2013) and was used for the energy calculation in this study.

Table 2.1: Properties of liquid and solid dodecanoic acid

Molecular Weight	200.31 kg/kmol
Density of Powder at 20°C / Liquid at 45°C	869 / 873 kg/m^3
Melting Temperature	42.5 ± 0.5°C
Latent Heat of Fusion	182 kJ/kg ± 5 %
Heat Capacity of Solid/Liquid	2.4 / 2.0 kJ/kg·K ± 3 %
Thermal Conductivities of Solid / Liquid	0.150 / 0.148 W/m·K
Viscosity of Liquid at 44 °C	0.008 Pa·s

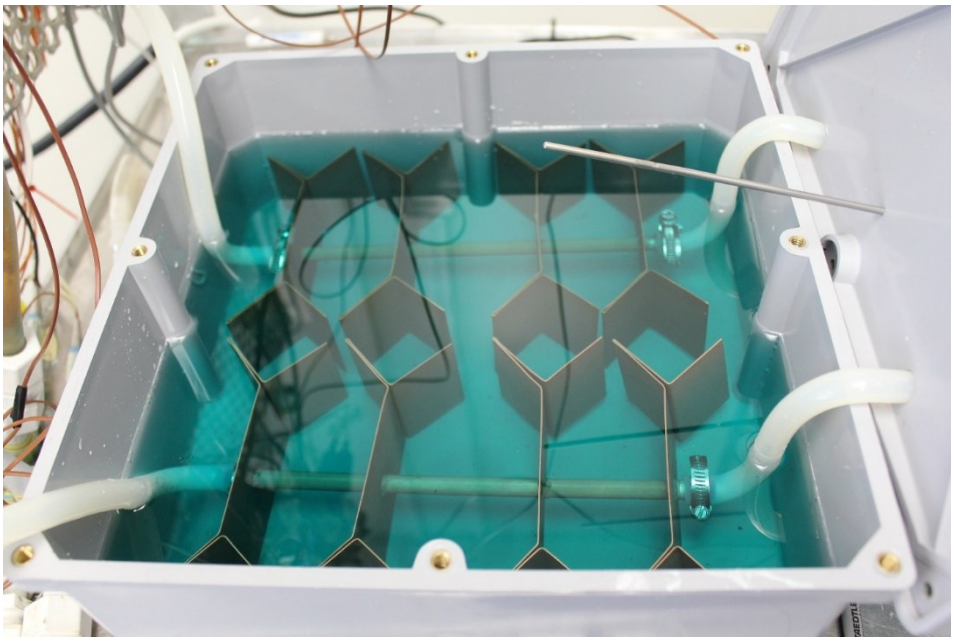

Figure 2.18: Photograph of the heat exchanger submerged in molten PCM

Figure 2.18 shows the system filled with molten dodecanoic acid up to a height of 97 mm, so that there is 20 mm of PCM above the top edge of the fins.

2.3. Experimental Procedure

To investigate the heat transfer characteristics of the heat exchangers, it is necessary to test them using various water temperatures leading to different temperature differentials driving the heat transfer. The experimental method for this process is as follows:

- Cycle water through the heat exchanger at 62.5 °C for at least 8 hours.
- Repeat for the following temperatures in order: 12.5, 72.5, 22.5 and 62.5 °C.
- Repeat for all fin geometries.

The four water setpoint temperatures (hot HTF of 62.5 and 72.5°C, cold HTF of 12.5 and 22.5°C) were selected to provide symmetrical ranges around the melting temperature of 42.5 °C, resulting in identical Stefan numbers. The 12.5 °C setpoint, for example, is 30 °C below the melting temperature, while 72.5 °C is 30 °C above the melting point. The Stefan number is a dimensionless term describing the ratio of the sensible and latent heat in a mass of phase change material, as shown in Eq. (2.1).

$$\mathrm{Ste} = \frac{c_p \Delta T}{L} \tag{2.1}$$

Ste is the Stefan number, c_p is the heat capacity of the material, L is the latent heat of the material, and ΔT is the temperature difference the material undergoes.

The flow rate for all experiments is set to 3 liters per minute. The Reynold's number was calculated for this flow rate according to Eq. (2.2).

$$\mathrm{Re}_D = \frac{\pi \rho \dot{V}}{4 \mu D} \tag{2.2}$$

Re_D is the Reynolds number for flow through a pipe, ρ is the density of water, $\dot{V}$ is the volumetric flow rate of water, μ is the dynamic viscosity of water, and D is the inside diameter of the pipe. Table 2.2 summarizes the pipe flow properties that remained constant for all of the experiments, while Table 2.3 lists the properties of water at the four tested temperatures.

Table 2.2: Pipe flow properties

Properties	Value
Flow rate	0.00005 m^3/s
Inside diameter	0.0079 m

Table 2.3: Water density and dynamic viscosity with temperature

Temperature (°C)	Density (kg/m^3)	Dynamic Viscosity (kg/m·s)
12.5	999.3	1.23
22.5	997.6	0.95
62.5	981.9	0.45
72.5	976.3	0.39

Table 2.4: Reynolds number for experimental conditions

Temperature (°C)	Reynolds Number
12.5	4036
22.5	5214
62.5	6492
72.5	7864

Table 2.4 shows the calculated Reynolds numbers for the four operation conditions of the experiment. Flow through a circular tube becomes turbulent at Reynolds numbers larger than 2300, so the regime is expected to be turbulent for all four experiments.

HTF Flow Rate Variations

Variations in the flow rate of the HTF will affect the rate of heat transfer in the system by changing the residence time of the fluid as well as the convective coefficient inside the pipes. Early trials of the experimental procedure investigated the effect of varying the HTF flow rates in the range of 1.1 to 4.1 L/min. It was found that varying the flow rate in this range had a negligible effect on the rate of heat transfer (Skaalum *et al.*, 2017).

2.4. Error and Uncertainty

2.4.1. Temperature and Volumetric Flow

Thermocouples

The thermocouple limits of error were examined using a FLUKE 7102 microbath, which maintains a bath of oil at a controlled temperature with accuracy ±0.25 °C and a stability of 0.015 °C.

The two T-type thermocouples used to measure the change in HTF temperature were tested simultaneously in the bath over a temperature range of 10 °C to 75 °C. Figure 2.19 shows the steady-state temperature readings of the two probes. The difference between the thermocouple readings and the setpoint temperature was in all cases less than 0.1 °C, and the maximum difference between the two thermocouples was 0.05 °C.

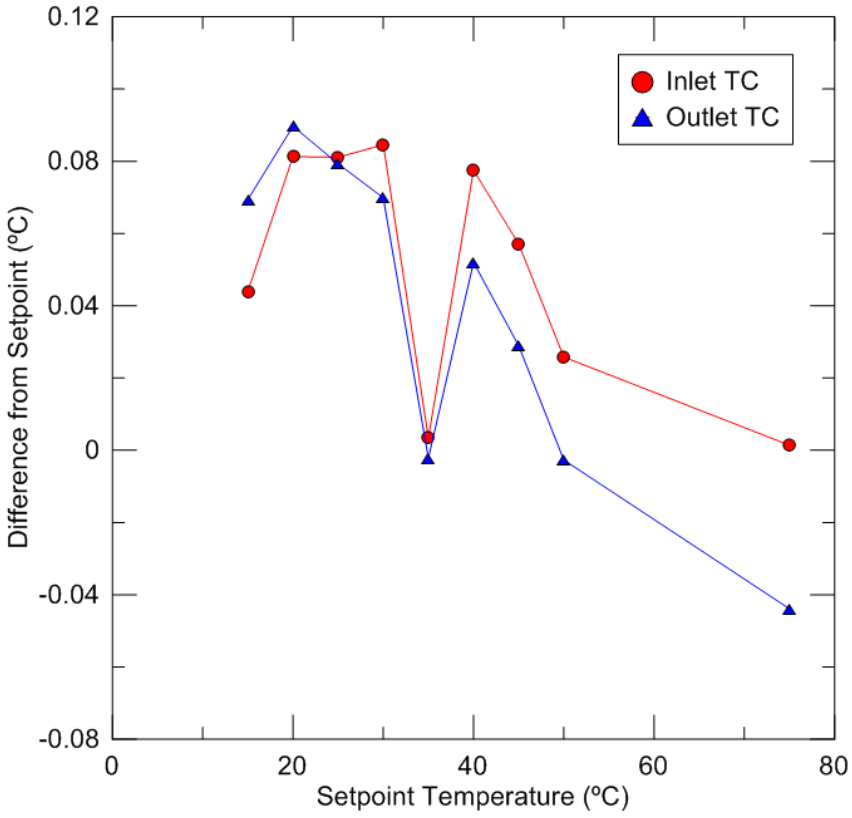

Figure 2.19: Calibration results of inlet and outlet thermocouples

The three K-type thermocouples were tested at the four HTF setpoint temperatures: 12.5 °C, 22.5 °C, 62.5 °C, and 72.5 °C. Figure 2.20 shows the results of the K-type thermocouple

calibration. The greatest deviation from the setpoint is thermocouple C, which registered 0.55 °C above the 12.5 °C setpoint. Therefore, ± 0.55 °C was used as the uncertainty of these three K-type thermocouples.

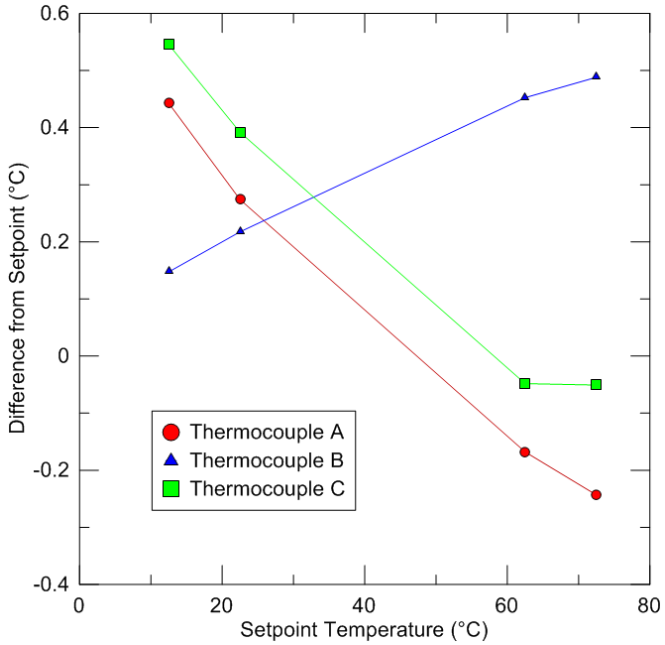

Figure 2.20: Calibration results of PCM thermocouples

Flow Meters

The measurement uncertainty used for the FTB 4605 flowmeter is ±2% of the output value, as specified in the equipment datasheet.

2.4.2. Heat Transfer Rate

The rate of heat transfer is calculated from the inlet and outlet temperatures according to Eq. (2.3)

$$\dot{Q} = \dot{m} c_p \Delta T \tag{2.3}$$

where $\dot{Q}$ is the rate of heat transfer, $\dot{m}$ is the mass flow rate of the HTF, c_p is the heat capacity of the water, and ΔT is the temperature change of the water between the inlet and outlet of the system. The mass flow rate is calculated by multiplying the density of water by the volumetric flow rate measured using the FTB 4605 flow meter, and thus the measurement uncertainty for the mass flow rate is 2%. The change in temperature is calculated from the difference between two T-type thermocouples placed on opposite ends

of the heat exchanger. These thermocouples were validated in constant-temperature bath, and it was found that the maximum variation between the two probes at the same temperature setpoint was 0.05 °C. Thus, ±0.05 °C is also used as the measurement uncertainty of the ΔT term.

The total measurement uncertainty of the rate of heat transfer is determined by calculating the maximum and minimum $\dot{Q}$ that could result from the two measurement uncertainties, as shown in Eqs. (2.4) and (2.5).

$$\dot{Q}_{max} = (1 + U_{\dot{V}}) * \dot{m} c_p (\Delta T + U_{\Delta T}) \tag{2.4}$$

$$\dot{Q}_{min} = (1 - U_{\dot{V}}) * \dot{m} c_p (\Delta T - U_{\Delta T}) \tag{2.5}$$

Where $U_{\dot{V}}$ is the measurement uncertainty of the flow sensors (as a percentage in decimal form) and $U_{\Delta T}$ is the measurement uncertainty of the temperature difference between the two T-type thermocouples. For each time step in the measurement output file a rate of heat transfer is calculated alongside upper and lower bounds based on measurement uncertainties. This method slightly overestimates the total measurement uncertainty compared to performing a root-mean-squared summation, but is much simpler to implement during data processing.

2.4.3. Net Energy Transfer

The net energy transferred between the HTF and the LHESS is calculated by integrating the rate of heat transfer over the duration of the experiment, as in Eq. (2.6).

$$\Delta E = \int \dot{m} c_p \Delta T \; dt \tag{2.6}$$

Where ΔE is the total energy transferred by the HTF. The maximum and minimum rates of heat transfer are likewise integrated to provide bounds of uncertainty for the net energy transfer.

The net energy transfer may also be calculated by considering the change in temperature of the PCM, according to Eq. (2.7).

$$\Delta E_{PCM} = \Delta E_{latent} + \Delta E_{sensible} = mL\varphi + mc_p \Delta T \tag{2.7}$$

Where ΔE_{PCM} is the change in PCM energy, ΔE_{latent} is the change in latent energy of the PCM, $\Delta E_{sensible}$ is the change of sensible energy in the PCM, m is the mass of the PCM, L is the latent heat of the PCM, φ is the fraction of PCM that has changed phase, c_p is the

heat capacity of the PCM, and ΔT is the temperature change of the PCM. The measurement uncertainties of these variables are presented in Table 2.5.

Table 2.5: Measurement uncertainties for calculating energy change

Variable	Measurement Uncertainty
Mass	5%
Latent Heat	5%
Heat Capacity	3%
Temperature Change	±1.0 °C

The uncertainties of the PCM material properties are those given by Desgrosseilliers *et al.* (2013). The temperature change is estimated from the HTF temperatures measured at the end of the previous experiment and the current experiment. Thus, the uncertainty of the temperature change is equal to double the measurement uncertainty of the T-type thermocouples inserted into the HTF stream. There is no uncertainty associated with the melt fraction because it is not measured, rather it is assumed that all of the PCM changes phase between the beginning and the end of each experiment.

The total measurement uncertainty for the PCM-side energy calculations is shown in Eq. (2.8).

$$U_E = U_{E,latent} + U_{E,sensible} = \Delta E_{latent}\left(\sqrt{U_m^2 + U_L^2}\right) + \Delta E_{sensible}\left(\sqrt{U_m^2 + U_{c_p}^2 + U_{\Delta T}^2}\right) \quad (2.8)$$

U_E is the total uncertainty, $U_{E,latent}$ is the total uncertainty of the latent energy change, $U_{E,sensible}$ is the total uncertainty of the sensible energy change, U_m is the uncertainty of the PCM mass, U_L is the uncertainty of the PCM latent heat, U_{c_p} is the uncertainty of the PCM heat capacity, and $U_{\Delta T}$ is the uncertainty of the PCM temperature change. In order to calculate the total uncertainty, $U_{\Delta T}$ is first divided by the recorded PCM temperature change to convert it to a percentage uncertainty.

Chapter 3. RESULTS AND DISCUSSION

This chapter will present the recorded temperature profiles and calculated rates of heat transfer for each experimental run with the three fin geometries (bifurcated, short-straight, and long-straight).

Four sequential experiments were performed for each fin type with the following HTF inlet temperatures: 22.5 °C, 72.5 °C, 12.5 °C and 62.5 °C. Each experiment was run for at least 8 hours, which was used as the cut-off point for displaying the results of each experiment.

3.1. Discharging with 22.5 °C HTF

3.1.1. Bifurcated Fins

Figure 3.1 shows the temperature data collected from the T-type thermocouples positioned at the HTF inlet and outlet, as well as the three K-type thermocouples placed within the PCM along the length of the heat exchanger. Temperatures were sampled at 4-second intervals, and then the raw data files were down-sampled to 20-second intervals to reduce the file sizes. Symbols were added to the three K-type thermocouples every 40 data points (800 second intervals) to help distinguish them from each other.

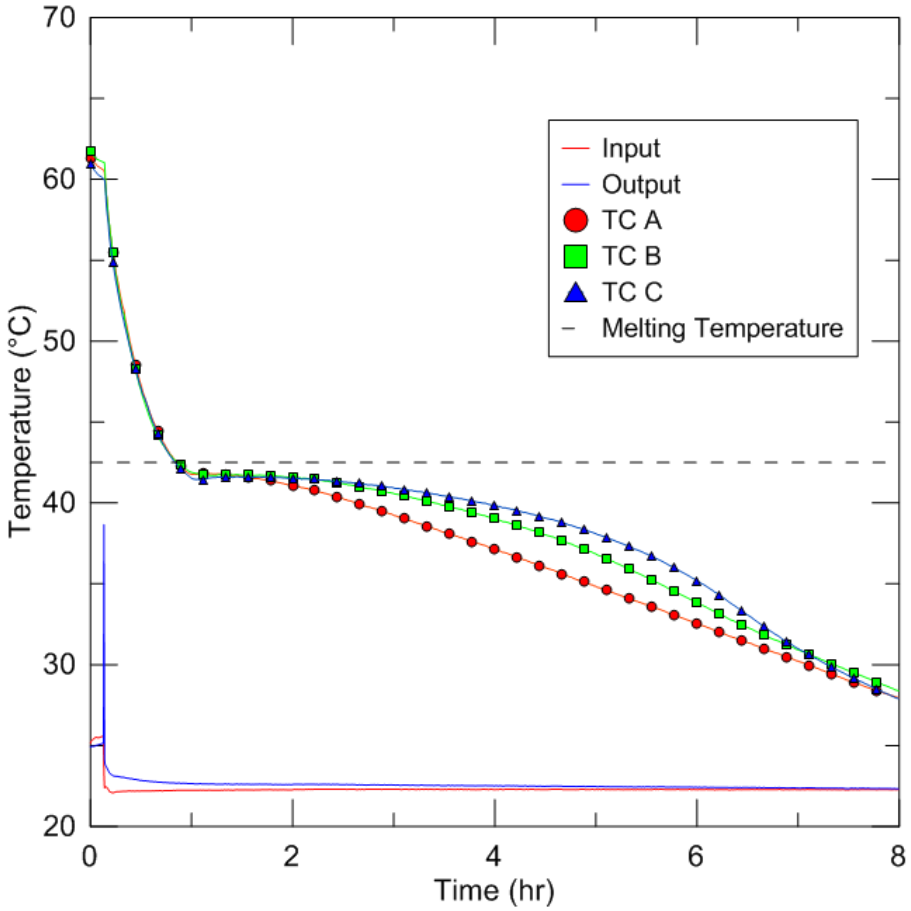

Figure 3.1: Temperature profile from bifurcated fin discharge experiment: HTF inlet temperature of 22.5 °C, initial temperature of 62.5 °C, Ste = 0.48

The PCM temperature begins at 62.5 °C before the HTF at 22.5 °C is introduced at the inlet. Once the cooler HTF is introduced, the temperature recorded by the thermocouples embedded into the PCM drops quickly to the solidification temperature in approximately 1 hour. The HTF output temperature spikes at the beginning of the experiment as the easily available energy in the PCM close to the heat exchanger and the copper is extracted. The temperature of the PCM around the thermocouples then stabilizes at 41.7 °C, which is slightly below the melting temperature, for another hour before beginning to decline once again towards the HTF setpoint. The temperature stabilization at 41.7 °C could be an indication of a small amount of supercooling, where the PCM only solidifies at a temperature below the melting point. Alternatively, the plateau location below the solidification temperature could be the result of combined uncertainties between the K-

type thermocouples and the literature value for this melting point. During the second temperature decline, the temperature probe at point A shows the quickest response, followed by the probes at B and C. Point A is closest to the HTF inlet/outlet side of the heat exchanger while C is the furthest away, thus the thermocouple A is expected to experience a greater temperature difference between the PCM and HTF than points B and C due to changes in the HTF temperature along the heat exchanger.

3.1.2. Short Straight Fins

Figure 3.2 shows the temperatures recorded for the 22.5 °C HTF experiment performed with the short-straight fins of equal surface area to the bifurcated fins. The initial temperature of the PCM is slightly lower than in the test shown in Figure 3.1 because that is the temperature the PCM stabilized at during the previous experiment (62.5 °C inlet HTF through the bifurcating-finned heat exchanger). Although the initial temperature for this test is 9 °C lower than the one performed with bifurcated fins, this temperature difference represents a relatively small fraction of the total energy change over the test period. During the bifurcated fin experiment the PCM exchanged 1785 kJ of energy, of which 511 kJ was sensible energy. The 9 °C difference in starting temperatures between the two experiments represents 126 kJ of energy, which is 7.4 % of the energy exchanged during the short-straight fin test and 7.1 % of the energy exchanged during the bifurcated-fin test.

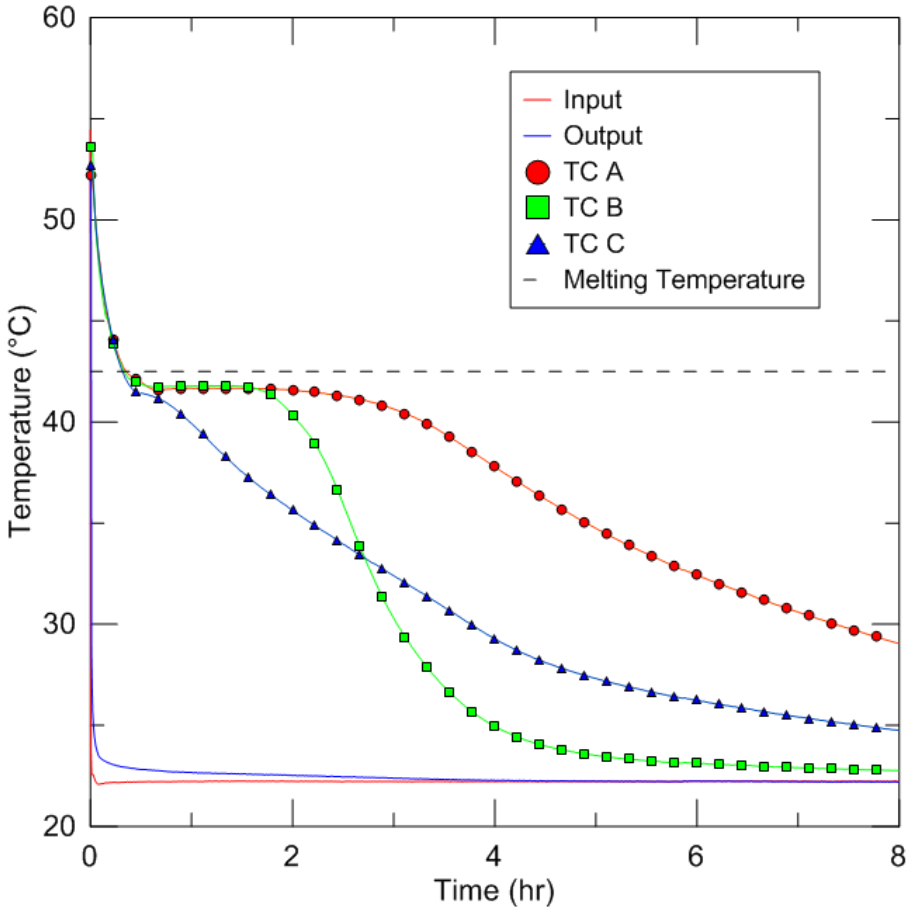

Figure 3.2: Temperature profile from short-straight fin discharge experiment: HTF inlet temperature of 22.5 °C, initial temperature of 53.5 °C, Ste = 0.38

For this test, the thermocouples at points B and C responded much more rapidly to the HTF temperature change than for the equivalent test performed with bifurcating-finned heat exchanger. Figure 3.3 shows the thermocouple placements relative to the straight fins. During the soldering process, one of the fins was attached at a slight angle, bringing it very close to thermocouple C. As a result, thermocouple C is expected to follow the HTF temperature more closely than A, which is further away from the fins. Thermocouple B is likewise placed much closer to a copper surface in the straight-finned arrangement than it was with the bifurcated fins, and thus should also respond quickly once the temperature fronts from the two adjacent fins meet.

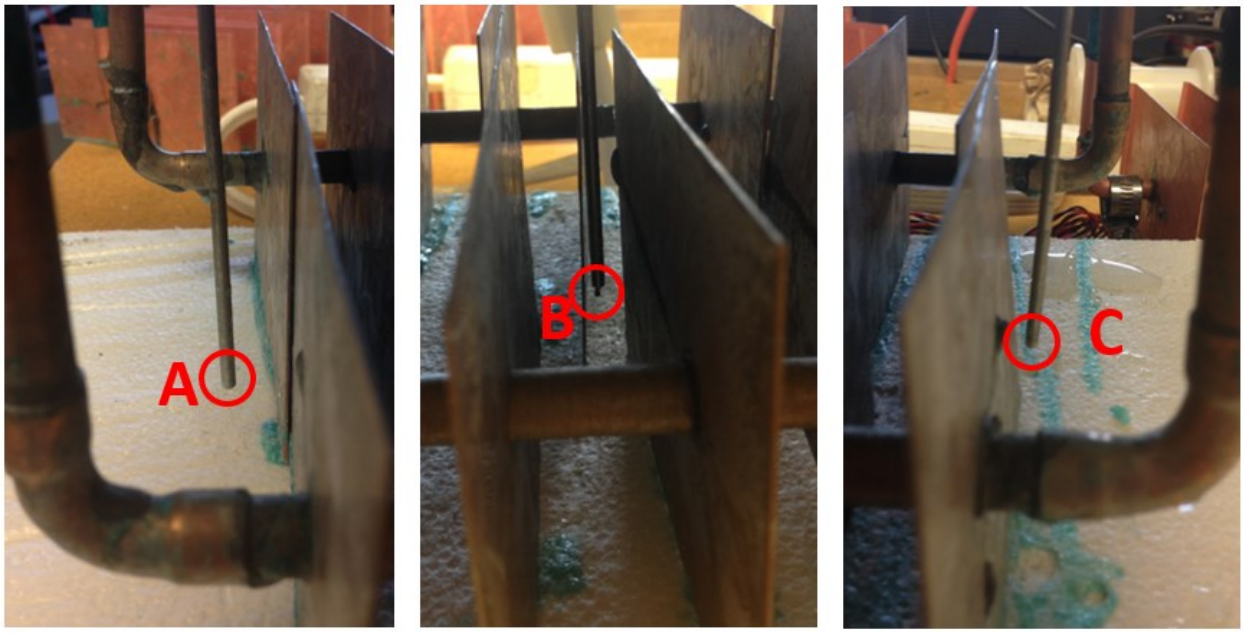

Figure 3.3: Positions of thermocouples relative to short-straight fins

3.1.3. Long Straight Fins

Figure 3.4 shows the temperatures recorded for the 22.5 °C HTF inlet experiment using the longer straight fins, with initial PCM temperature of 58 °C. Compared to the shorter straight fins, the longer fins were able to bring the PCM temperature slightly closer to the HTF inlet temperature by the end of the 8-hour run, likely due to the increased surface area and thus rate of heat transfer. For both of the straight-finned exchanger experiments, the thermocouples embedded in the PCM reached the melting temperature more quickly than in the case of the bifurcating-finned exchanger. As the distance between the probes and the fins is different for the bifurcated and straight-finned exchangers, it is difficult to draw conclusions from the rapidity of the thermocouple response rates. It is likely, however, that the proximity of each straight fin to its neighbour results in more concentrated regions of heat exchange around the locations where the probes are placed.

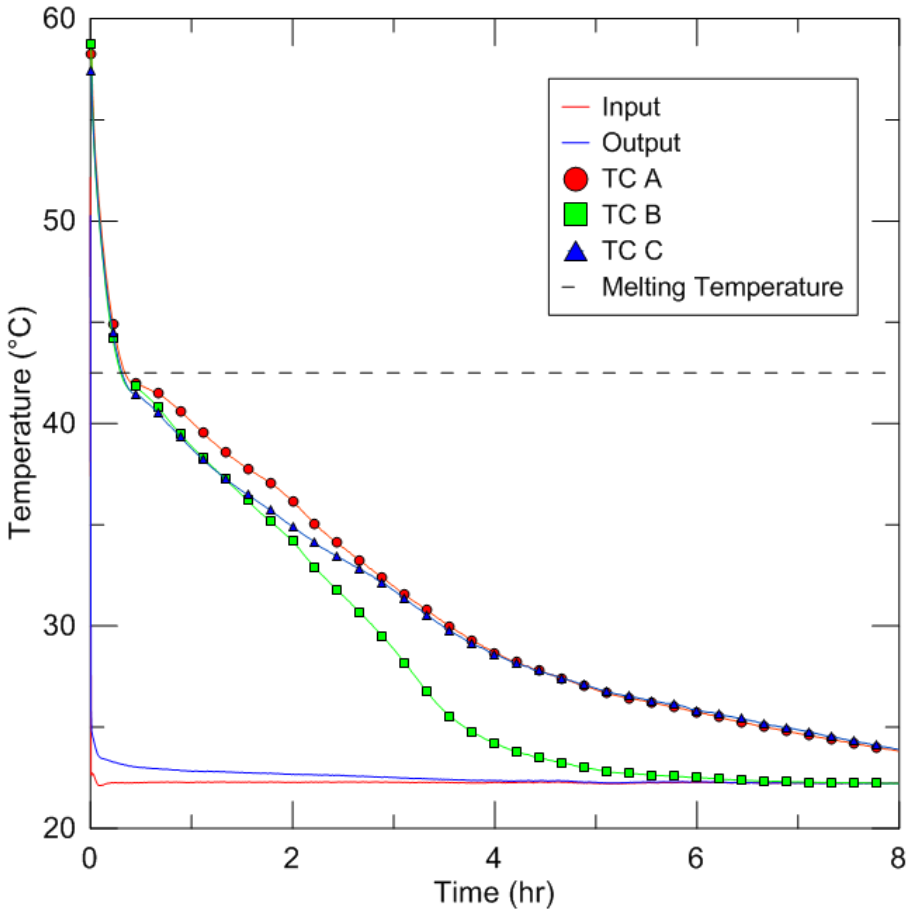

Figure 3.4: Temperature profile from long-straight fin discharge experiment: HTF inlet temperature of 22.5 °C, initial temperature of 58 °C, Stefan = 0.43

3.1.4. Power Comparison

Figure 3.5 shows the rates of heat transfer for the three experiments run with 22.5 °C HTF. The dotted lines represent the uncertainty on the rates of heat transfer. As the HTF mass flow rate and heat capacity are constant throughout the experiment, the profiles in the figure also represent the temperature difference between the inlet and outlet streams. The axis on the right has the scale for the temperature difference, which is generally below 1 K due to the small size of this experimental heat exchanger. For all three fin types, the heat transfer rate is disproportionally large at the beginning of the experiment, corresponding with the sudden increase in outlet HTF temperature compared to the inlet due to the removal of easily available thermal energy. The rate of heat transfer during the first few seconds of the

experiment is generally in the magnitude of thousands of Watts, but the axis of the figure has been limited to 400 W to preserve the details of the profile.

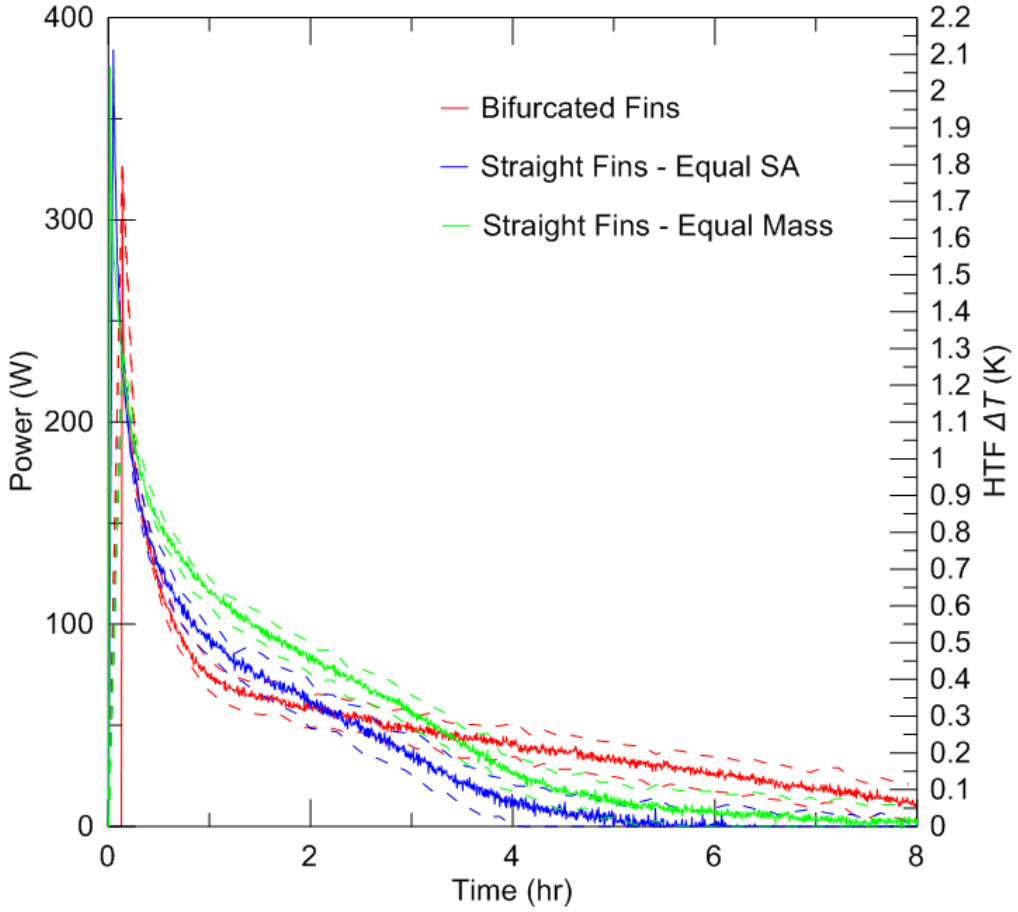

Figure 3.5: Rate of heat transfer profiles for all three fin types with HTF inlet temperature of 22.5 °C

The rate of heat transfer profiles for the two straight-finned exchangers are very similar, with the longer fins providing more heat transfer as expected due to their increased surface area compared to the other two fins types. The bifurcating-finned exchanger provides the lowest rate of heat transfer for the first two hours of the experiment, but afterwards maintains a higher rate of heat transfer than the straight-finned exchangers. The declining slope of the two straight-finned exchangers is much steeper than the bifurcating-finned exchanger, thus it takes much longer for the bifurcating-finned exchanger to remove all of the available energy and reach 0 W of heat transfer.

Figure 3.6 shows the rate of heat transfer divided by the total surface area of the fins, normalizing the differences in surface area between the longer straight fins and the other two fin types. The profiles in this figure show that the two straight fin types provide similar rates of heat transfer per unit area for the first two hours of the experiment. For the remainder of the run, however, the longer straight fins maintain a higher normalized rate of heat transfer than the shorter straight fins. During discharge, conduction is the primary mode of heat transfer between the PCM and the heat exchanger. The longer fins therefore provide an advantage over the shorter fins due to the reduced distance that heat must conduct through the PCM before reaching the heat exchanger.

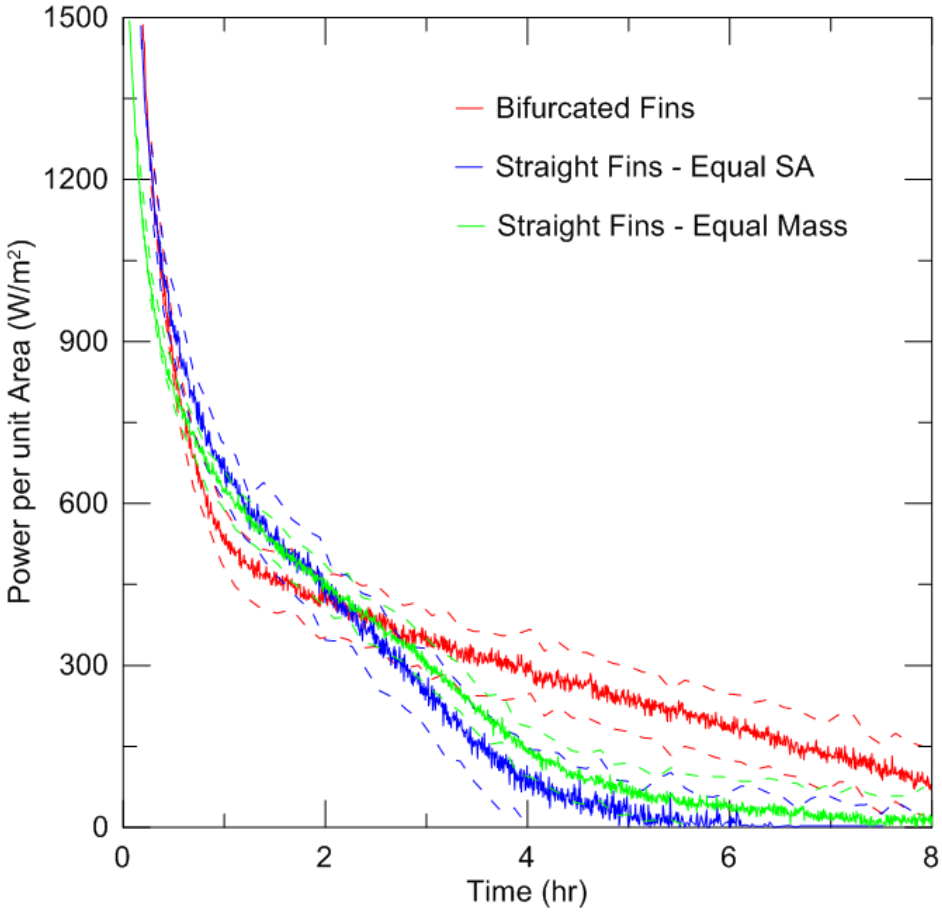

Figure 3.6: Rate of heat transfer profiles per unit of fin area for all three fin types with HTF inlet temperature of 22.5 °C

3.2. Discharging with 12.5 °C HTF

3.2.1. Bifurcated Fins

Figure 3.7 shows the temperature data collected from the 12.5 °C HTF inlet temperature experiment through the bifurcating-finned heat exchanger. The initial temperature of the PCM around the thermocouples begins at 65 °C, which is where the PCM temperature stabilized during the previous experiment (HTF inlet temperature of 72.5 °C through the bifurcating-finned exchanger). The temperature trends are very similar to the experiment performed on the same heat exchanger with 22.5 °C HTF, but with a shorter temperature plateau.

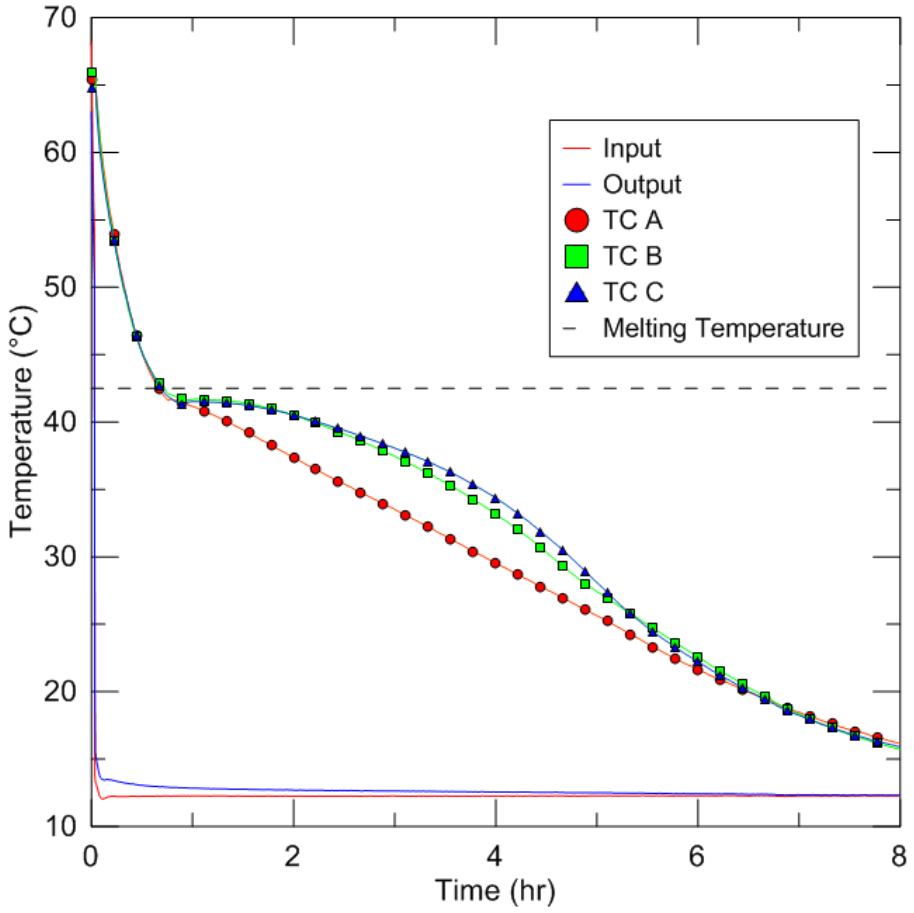

Figure 3.7: Temperature profile from bifurcated fin discharge experiment: HTF inlet temperature of 12.5 °C, initial temperature of 65 °C, Ste = 0.64

3.2.2. Short Straight Fins

Figure 3.8 shows the temperatures recorded for the 12.5 °C HTF experiment run with the short-straight finned heat exchanger and the same initial PCM temperature of 65 °C as the bifurcated-fin experiment. Compared to the bifurcating-finned exchanger, the short-straight fins resulted in a more rapid decline in temperature at points B and C, but a slower decline at point A.

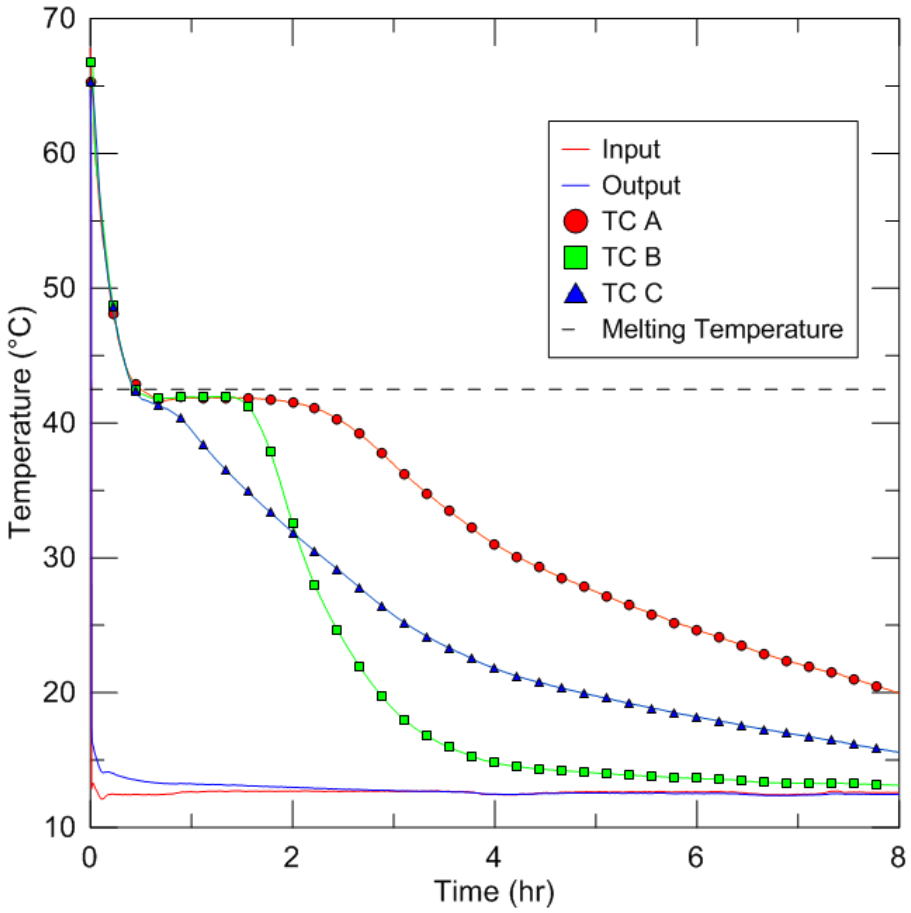

Figure 3.8: Temperature profile from short-straight fin discharge experiment: HTF inlet temperature of 12.5 °C, initial temperature of 66 °C, Ste = 0.65

3.2.3. Long Straight Fins

Figure 3.9 shows the temperatures recorded for the 12.5 °C HTF inlet temperature experiment run with the long-straight fins, with the initial PCM of 65.5 °C. For the long-straight fins the temperature plateau is negligibly short, but the temperature of the three

PCM thermocouples is the same by the 8-hour mark as for the experiments run with the other two types of fins.

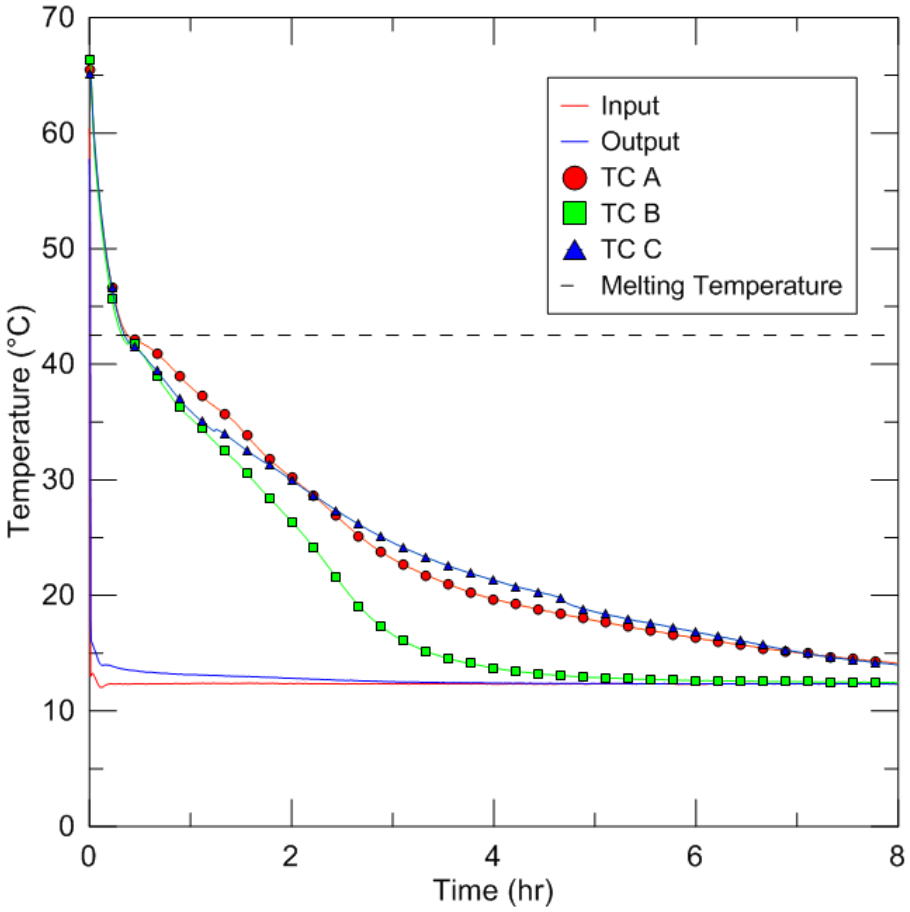

Figure 3.9: Temperature profile from long-straight fin discharge experiment: HTF inlet temperature of 12.5 °C, initial temperature of 65.5 °C, Ste = 0.64

3.2.4. Power Comparison

Figure 3.10 shows the rates of heat transfer for the three experiments run with 12.5 °C HTF. Compared to the tests run at 22.5 °C, the rates of heat transfer are greater for all three fin types, as expected due to the larger difference between the HTF inlet and the solidification temperature. As with the 22.5 °C experiments, the bifurcating-finned exchanger maintains a steadily-declining rate of heat transfer over a longer period of time compared to the two straight-finned exchangers.

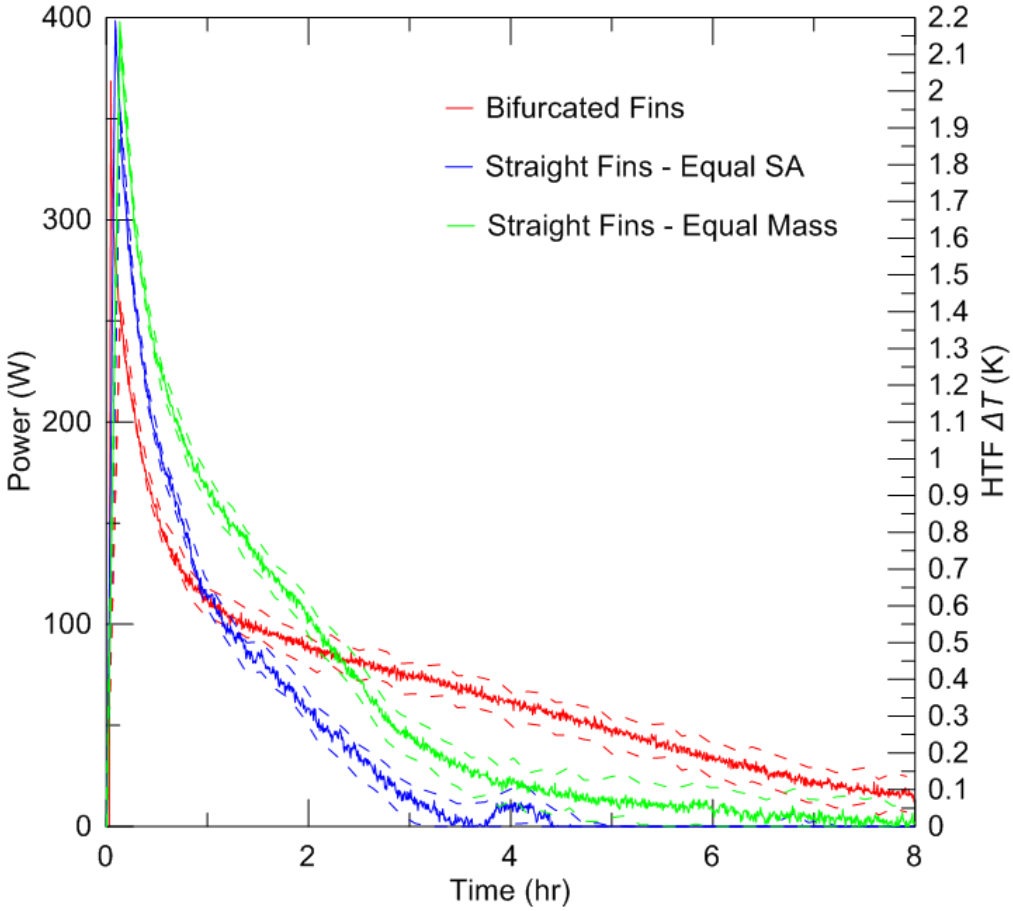

Figure 3.10: Rate of heat transfer profiles for all three fin types with HTF inlet temperature of 12.5 °C

Figure 3.11 shows the heat transfer profiles normalized by the surface area of the three fin types. In this normalized plot, the heat transfer rates provided by the three heat exchangers are equivalent for the first hour of the experiment, after which the profiles for the two straight fins declines quickly while the bifurcated fins profile descends more gradually.

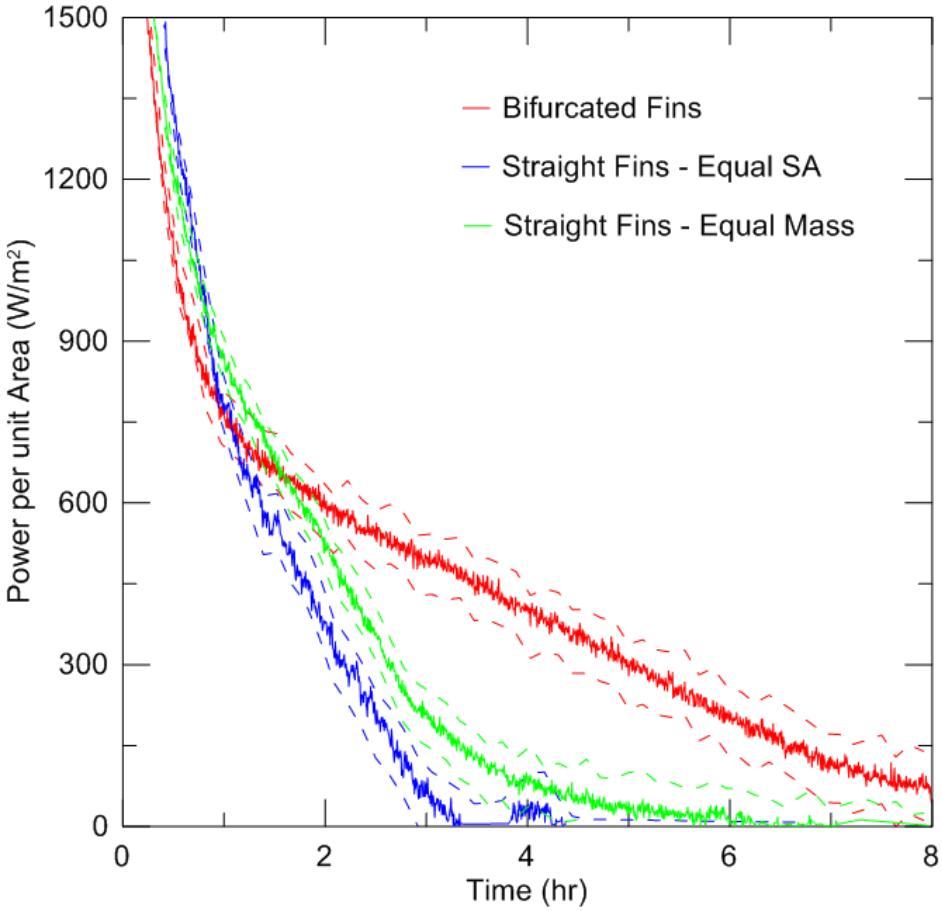

Figure 3.11: Rate of heat transfer profiles per unit of fin area for all three fin types with HTF inlet temperature of 12.5 °C

3.3. Charging with 62.5 °C HTF

3.3.1. Bifurcated Fins

Figure 3.12 shows the temperature data collected from the 62.5 °C HTF experiment run with the bifurcated fins and the PCM initially at 12.5 °C. The jagged appearance of the inlet and outlet temperatures is the result of the on-off operation of the heater unit. The heater unit was also difficult to set to a specific temperature, thus for this experiment the inlet temperature is closer to 60 °C rather than the intended 62.5 °C. Compared to the discharge experiments (HTF of 22.5 and 12.5 °C) the PCM thermocouples take longer to reach the plateau and spend much longer at constant temperature during this middle stage of the experiment.

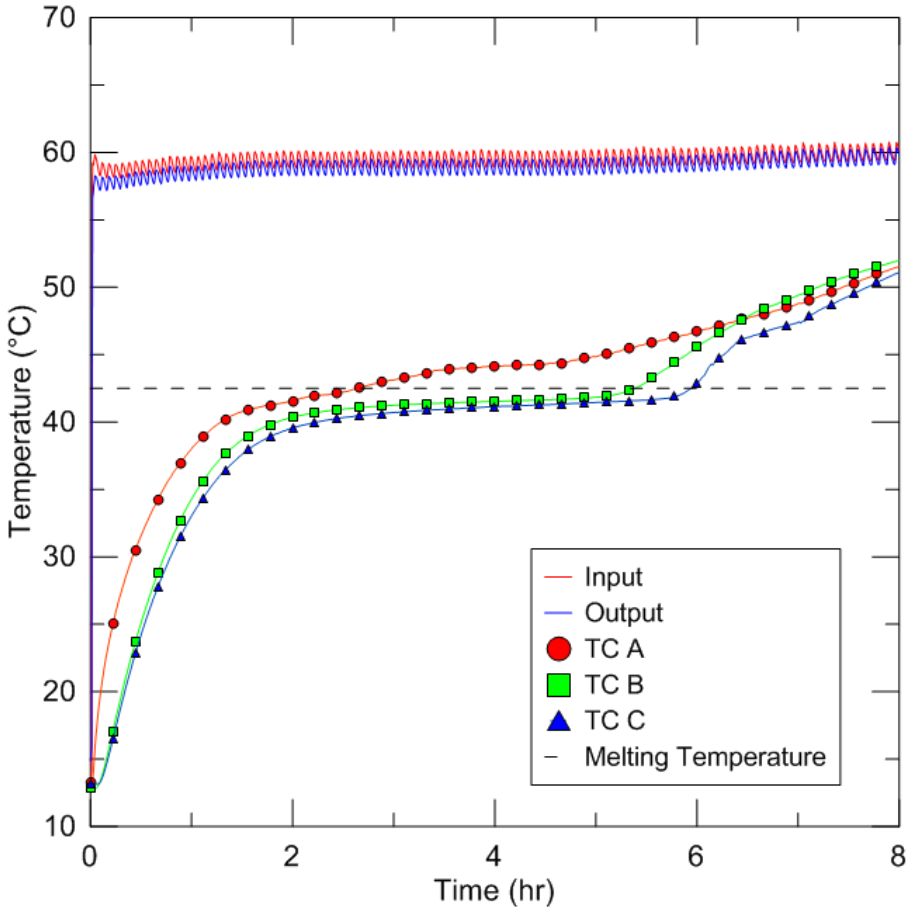

Figure 3.12: Temperature profile from bifurcated fin charging experiment: HTF inlet temperature of 60 °C, initial temperature of 12.5 °C, Ste = 0.57

3.3.2. Short Straight Fins

Figure 3.13 shows the temperatures recorded for the 62.5 °C HTF experiment performed with the straight-finned heat exchanger and initial PCM temperature of 12.5 °C. The HTF inlet temperature is closer to 64 °C for the first three hours of the experiment due to the imprecision of the control mechanism, but for the remainder of the experiment it remains at the intended setpoint. Compared to the bifurcating-finned exchanger, the PCM thermocouples exceed the melting temperature much sooner, likely due to the smaller distance between the probes and the fins. In addition, the thermocouples report a temperature of 57.5 °C by the 8-hour mark, which is 6 degrees higher than the final

temperature reading from the same experiment performed with the bifurcating-finned exchanger.

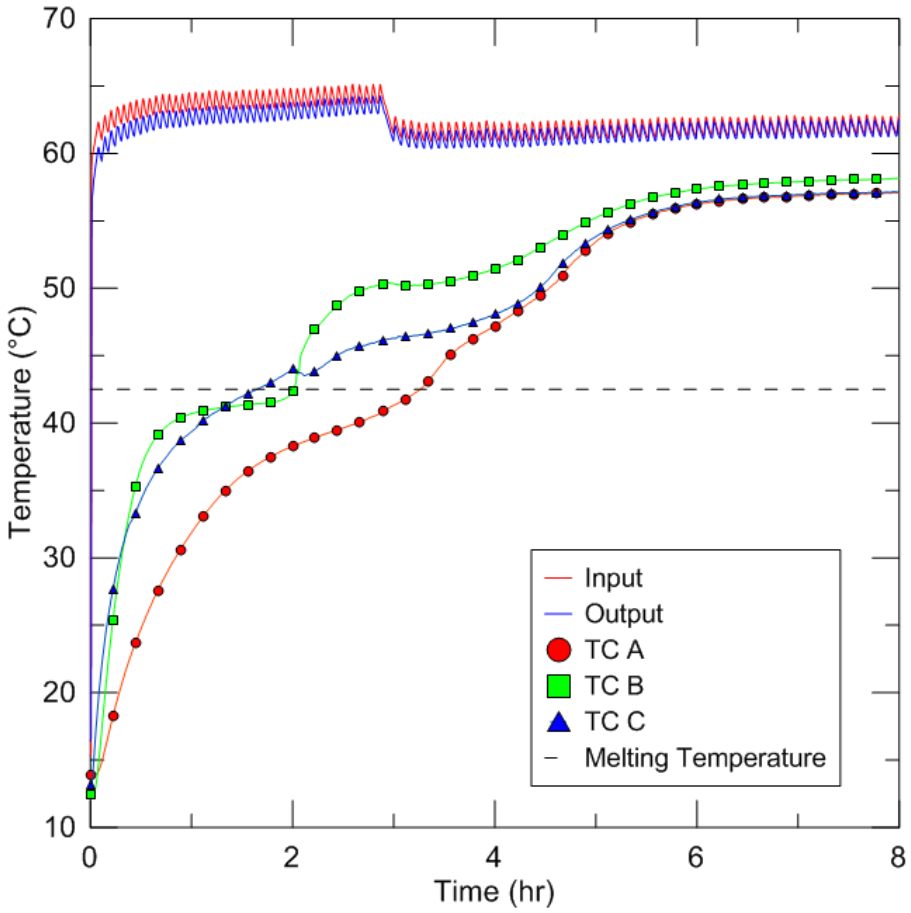

Figure 3.13: Temperature profile from short-straight fin charging experiment: HTF inlet temperature of 62.5 °C, initial temperature of 12.5 °C, Ste = 0.60

3.3.3. Long Straight Fins

Figure 3.14 shows the temperatures recorded for the 62.5 °C charging experiment performed with the long-finned heat exchanger and the PCM initially at 12.5 °C. As expected, the trends are similar to those recorded for the short-finned exchanger, but with the thermocouples reaching a steady state temperature about 30 minutes sooner due to the greater surface area. Notably, the PCM around the thermocouples in the bifurcating-finned exchanger were still in the process of approaching a steady temperature when the 8-hour experiment ended.

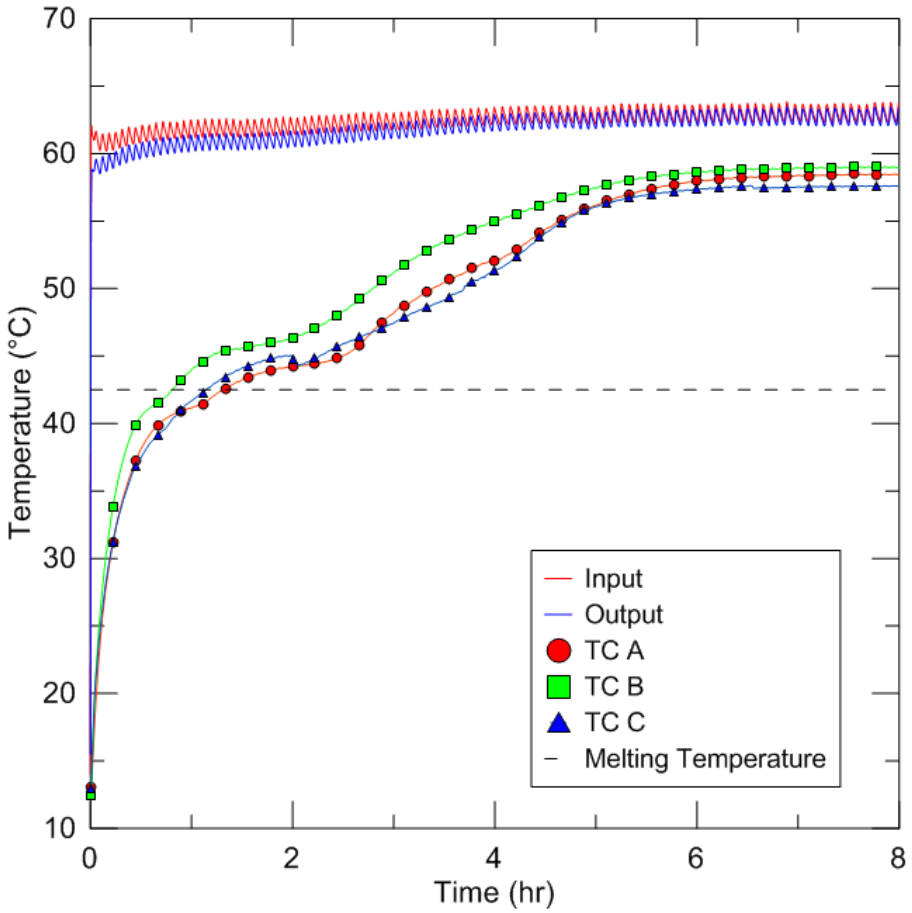

Figure 3.14: Temperature profile from long-straight fin charging experiment: HTF inlet temperature of 62.5 °C, initial temperature of 12.5 °C, Ste = 0.60

3.3.4. Power Comparison

Figure 3.15 shows the rates of heat transfer for the three experiments run with 62.5 °C HTF. A 13-point rolling average was used to smooth out the jagged peaks of the data, so that the trends may be observed more clearly. For these charging experiments, the rate of heat transfer profiles for the straight fins overlap almost completely. This similarity is likely due to the presence of natural convection within the molten PCM enhancing the rate of heat transfer, and thus masking the differences in heat transfer due to surface area.

The bifurcating-finned exchanger maintains a lower rate of heat transfer during the first half the of the experiment and a higher one during the latter half compared to the two straight-finned exchangers. This same pattern was seen during the two discharge experiments, but is much more pronounced for the charging experiments.

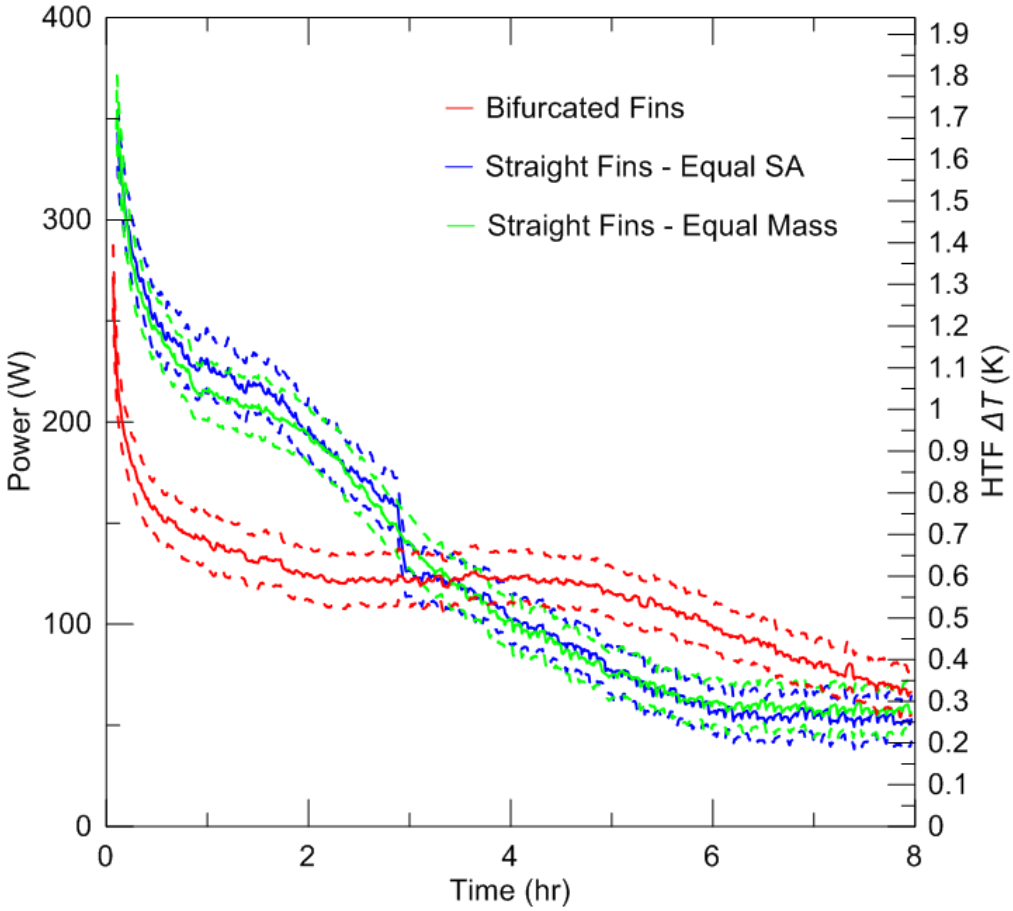

Figure 3.15: Rate of heat transfer profiles for all three fin types with HTF inlet temperature of 62.5 °C

Figure 3.16 shows the rates of heat transfer normalized by fin surface area. The normalization highlights how the additional surface area of the longer straight fins does not result in a proportional gain in heat transfer rate. Overall, when charging with a HTF temperature of 62.5 °C, the shorter straight fins provide the highest rates of heat transfer per unit area.

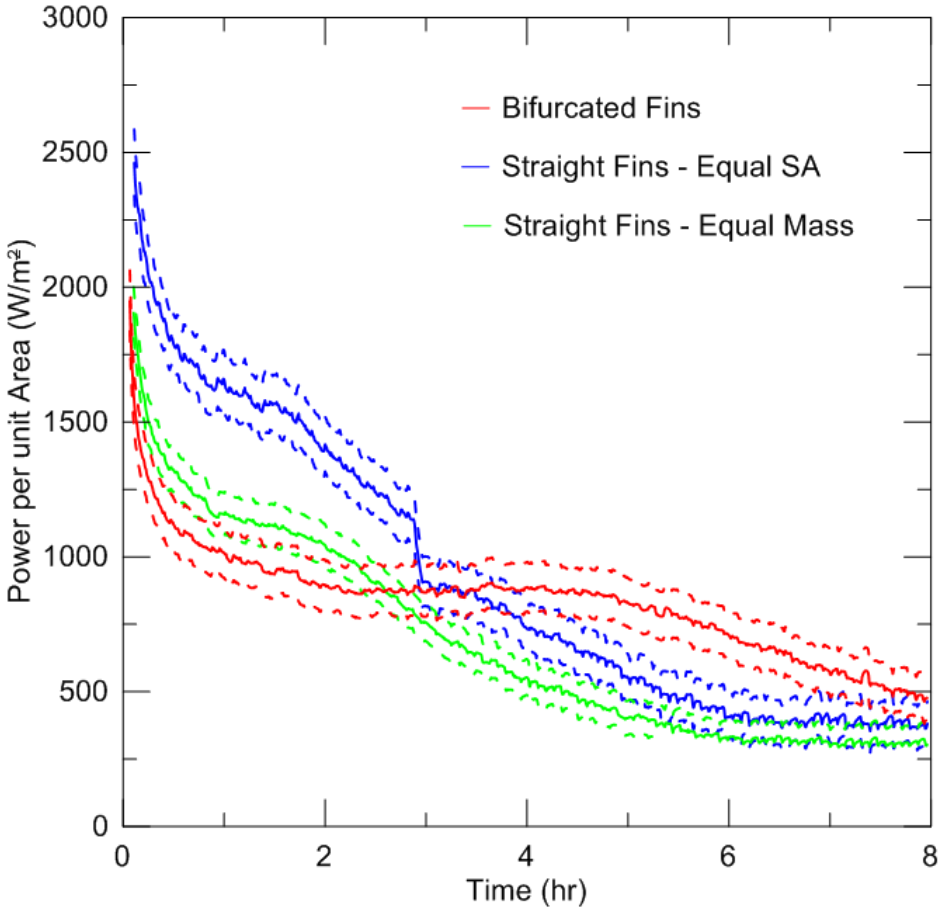

Figure 3.16: Rate of heat transfer profiles per unit of fin area for all three fin types with HTF inlet temperature of 62.5 °C

For all three experiments, the rate of heat transfer reaches a value of approximately 60 W by the end of the experiment. For the two straight-finned tests, the PCM thermocouples had reached a steady temperature by this point, indicating that the energy transferred from the HTF is being lost through the system to the environment. The majority of the energy losses to the environment likely left through the uninsulated piping between the HTF inlet and outlet, as well as through some small uninsulated regions on the lid of the LHESS. As the HTF temperature within these pipes was held constant throughout the experiment, the rate of heat loss should be consistent over the entire 8-hour run. Therefore, the heat transfer rate profiles may be corrected by subtracting the steady-state heat losses at each time step.

Figure 3.17 shows the data from Figure 3.15 shifted downwards by 60 W to account for the ambient losses.

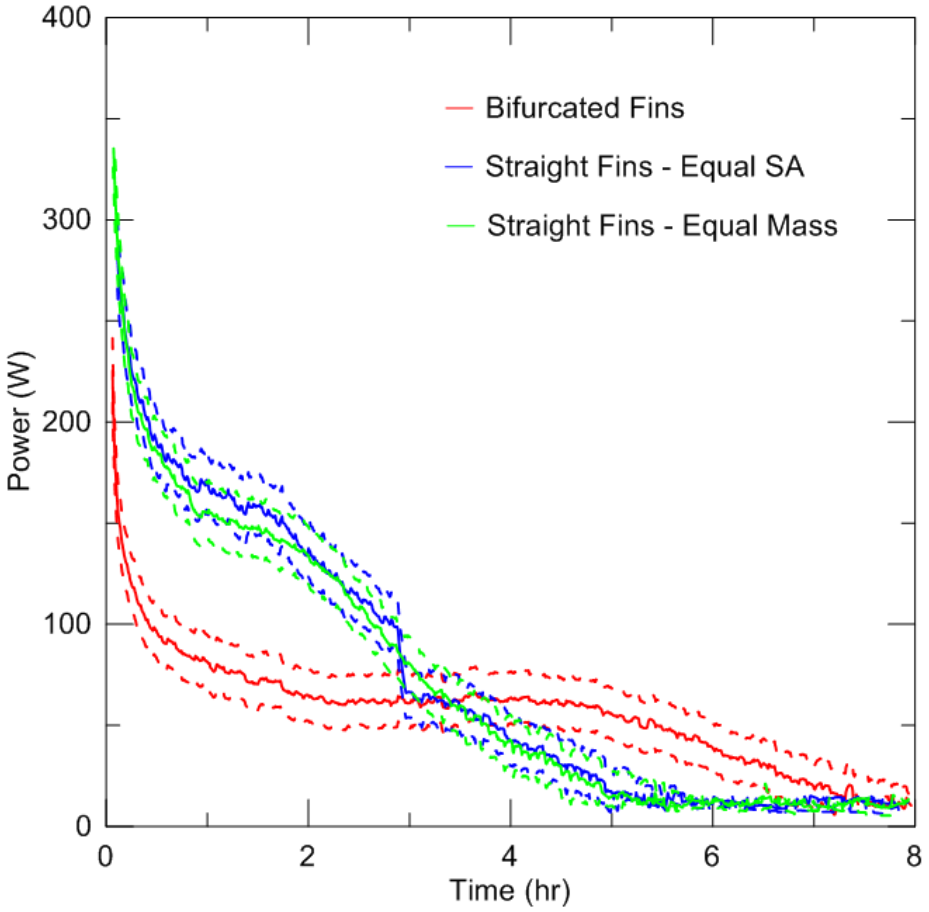

Figure 3.17: Rate of heat transfer profiles for all three fin types with HTF inlet temperature of 62.5 °C corrected to account for ambient losses.

Figure 3.18 shows the heat transfer rates of the fin types per unit surface area corrected to account for the 60 W of heat lost to the environment.

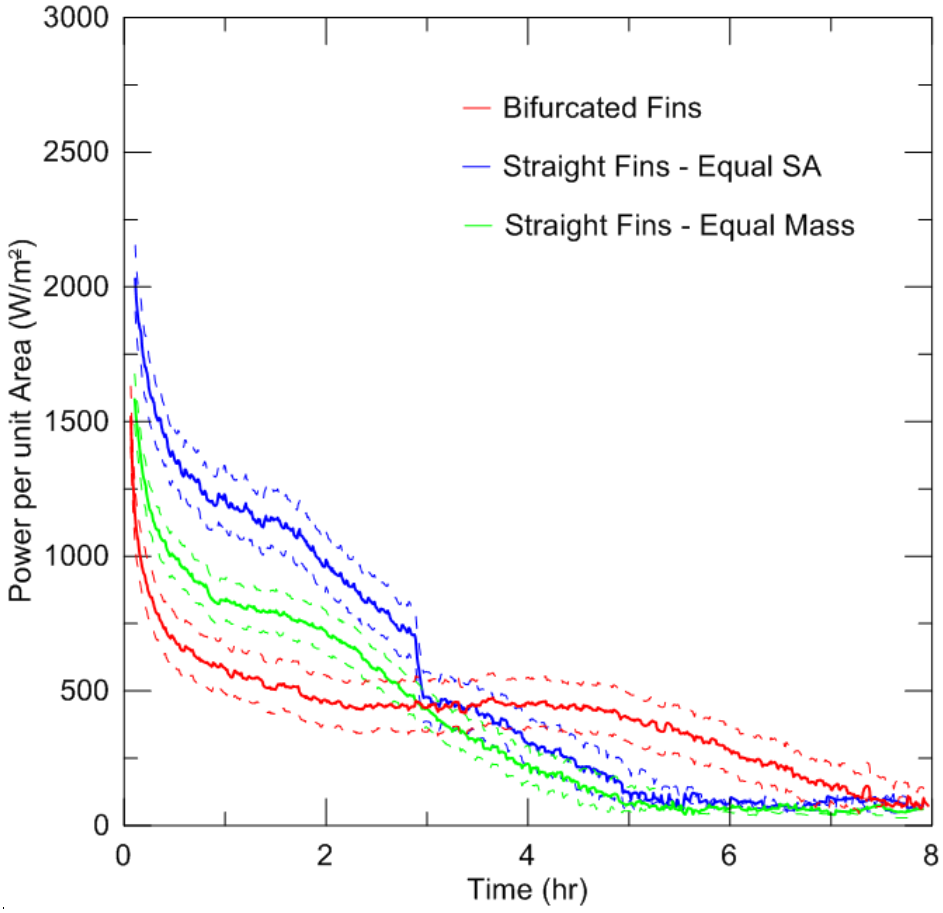

Figure 3.18: Rate of heat transfer profiles per unit of fin area for all three fin types with HTF inlet temperature of 62.5 °C corrected to account for ambient losses.

3.4. Charging with 72.5 °C HTF

3.4.1. Bifurcated Fins

Figure 3.19 shows the temperature data collected from the experiment performed with the bifurcating-finned exchanger, which followed the discharge experiment performed with the same heat exchanger and HTF at 22.5 °C. For this experiment the HTF inlet temperature was set to 72.5 °C and the initial PCM temperature was 22.5 °C. The jagged appearance of the inlet and outlet temperatures is the result of the on-off operation of the heater unit.

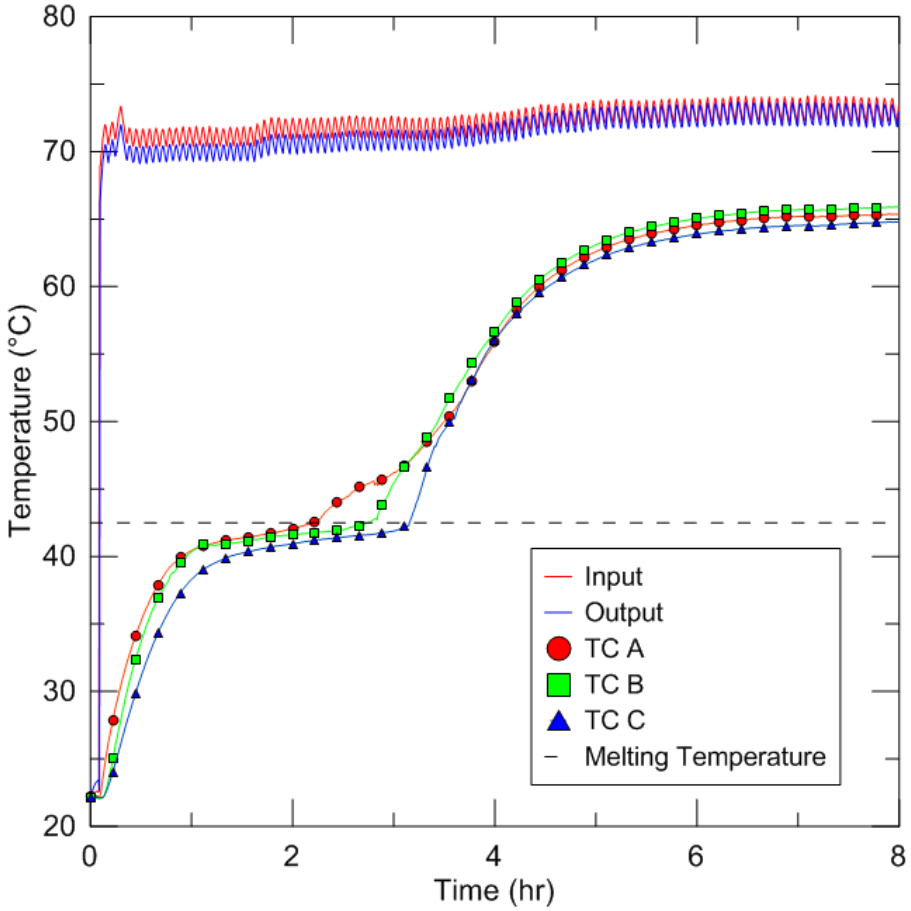

Figure 3.19: Temperature profile from bifurcated fin charging experiment: HTF inlet temperature of 72.5 °C, initial temperature of 22.5 °C, Ste = 0.60

Compared to the experiment performed with the bifurcating-finned exchanger using 62.5 °C HTF at the inlet, increasing the HTF temperature to 72.5 °C has a dramatic effect on the melting profile. The temperature plateau around the melting point is shortened from 4 hours to around 1 hour, and the PCM thermocouples record a steady-state temperature well within the 8-hour experiment run time.

3.4.2. Short Straight Fins

Figure 3.20 shows the temperatures recorded for the 72.5 °C HTF experiment performed with the straight-finned heat exchanger and an initial PCM temperature of 22.5 °C. Compared to the same experiment performed with bifurcated fins, the PCM thermocouples

exceed the melting point sooner, which in turn results in the PCM reaching a steady-state temperature approximately 1 hour earlier.

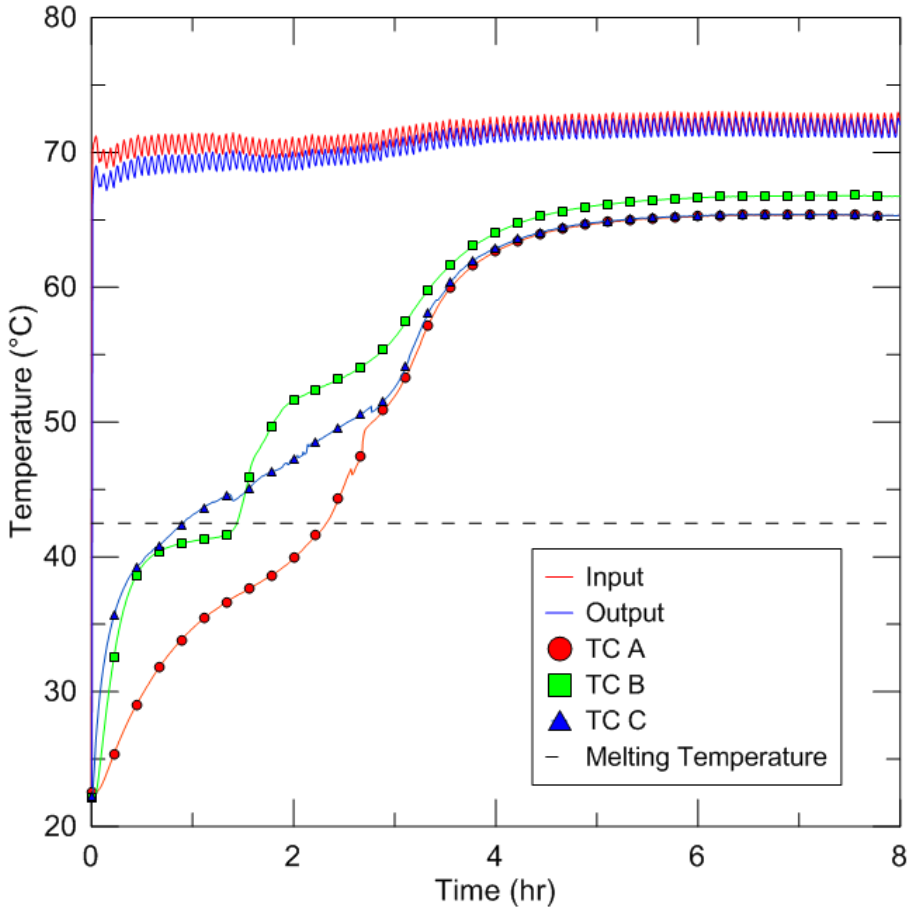

Figure 3.20: Temperature profile from short-straight fin charging experiment: HTF inlet temperature of 72.5 °C, initial temperature of 22.5 °C, Ste = 0.60

3.4.3. Long Straight Fins

Figure 3.21 shows the temperatures recorded for the long-straight finned exchanger run with 72.5 °C HTF at the inlet and an initial PCM temperature of 22.5 °C. The profile is similar to the ones captured during the same experiment run with the shorter fins, except the PCM thermocouples reach the melting temperature slightly sooner and thus the steady state temperature earlier.

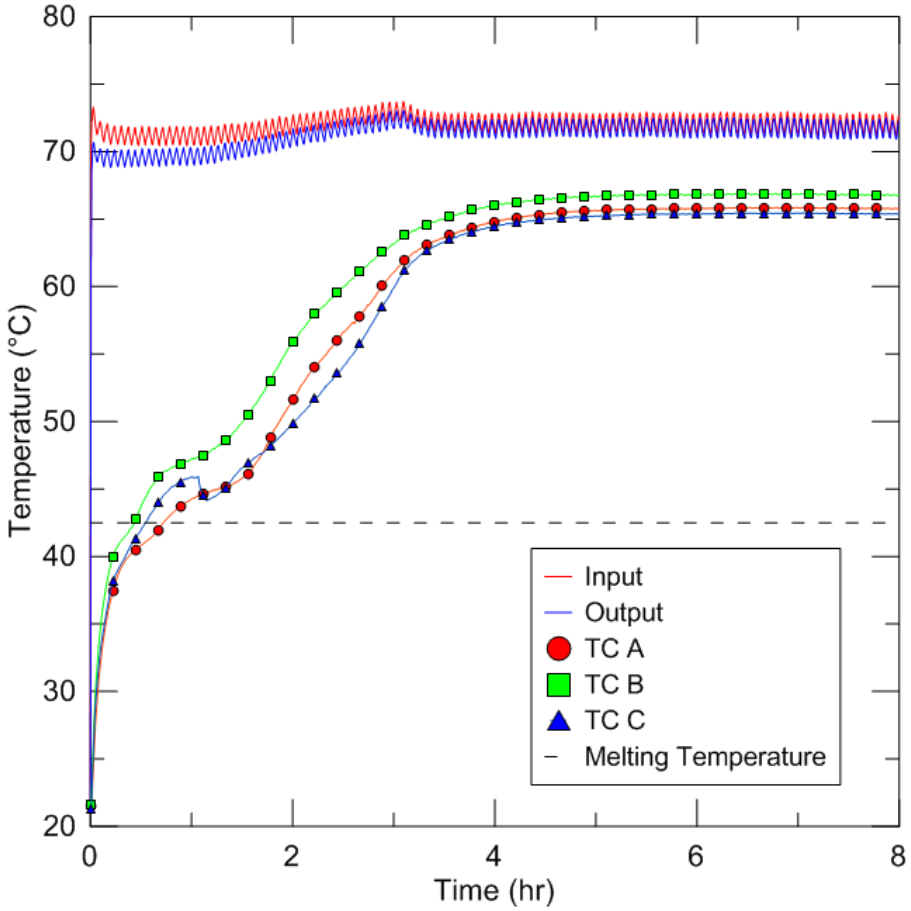

Figure 3.21: Temperature profile from long-straight fin charging experiment: HTF inlet temperature of 72 °C, initial temperature of 22.5 °C, Ste = 0.60

3.4.4. Power Comparison

Figure 3.22 shows the rates of heat transfer for the three experiments run with 72.5 °C HTF. As with the experiments run with 62.5 °C HTF, the long-straight finned heat exchanger initially shows the highest rate of heat transfer, followed closely by the short-finned exchanger, with the bifurcating-finned exchanger transferring heat at a rate around 50 W lower than the short-straight finned exchanger. After a brief plateau, the heat transfer rates of the two straight-finned exchangers declines rapidly, while the bifurcating-finned exchanger maintain a plateau for another 1.5 hours. Once all three profiles are in the declining phase the order of heat transfer reverses, with the bifurcating fins performing the best and the longer straight fins providing the lowest rate. Around the 5-hour mark, all of

the profiles reach a steady-state between 50 – 75 W, representing heat lost through the system to the environment.

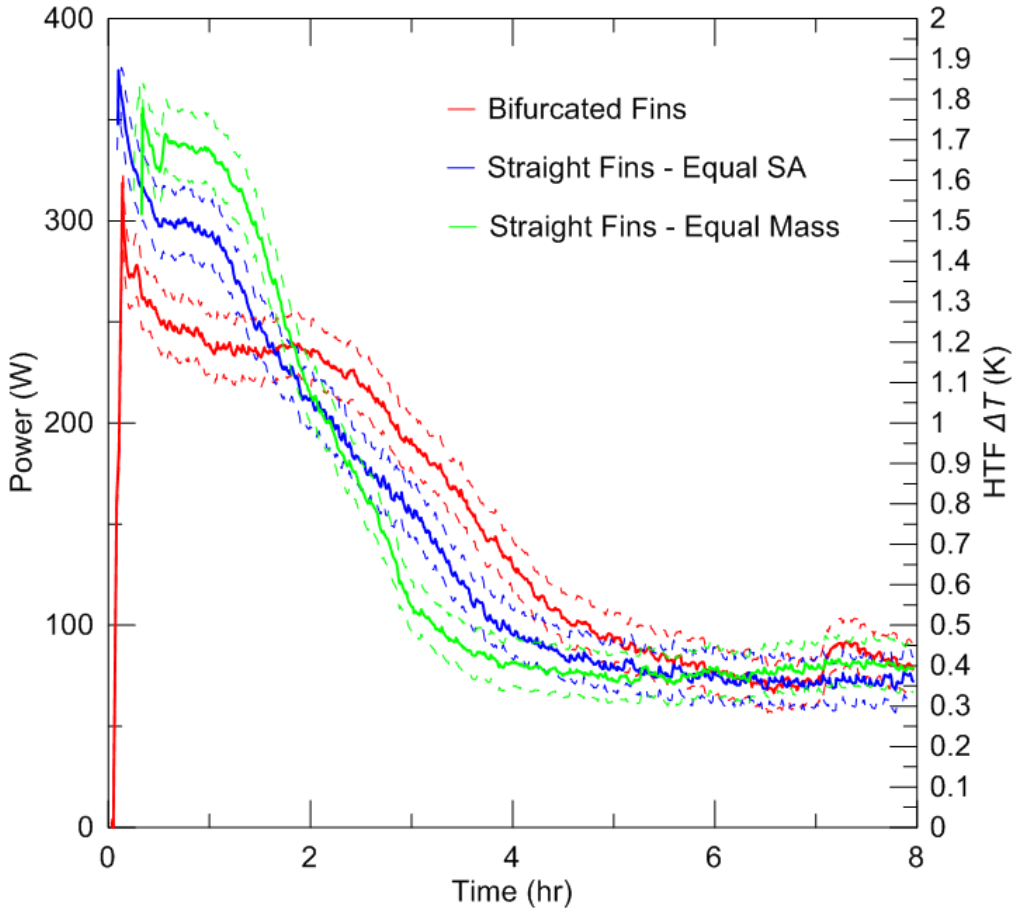

Figure 3.22: Rate of heat transfer profiles for all three fin types with HTF inlet temperature of 72.5 °C

Figure 3.23 shows the data from Figure 3.22 normalized by the surface area of the three heat exchangers. As with the results from the charging experiments run with 62.5 °C HTF, the normalization demonstrates that the longer straight fins are not as productive in terms of heat transfer per unit area compared to the other two fin geometries.

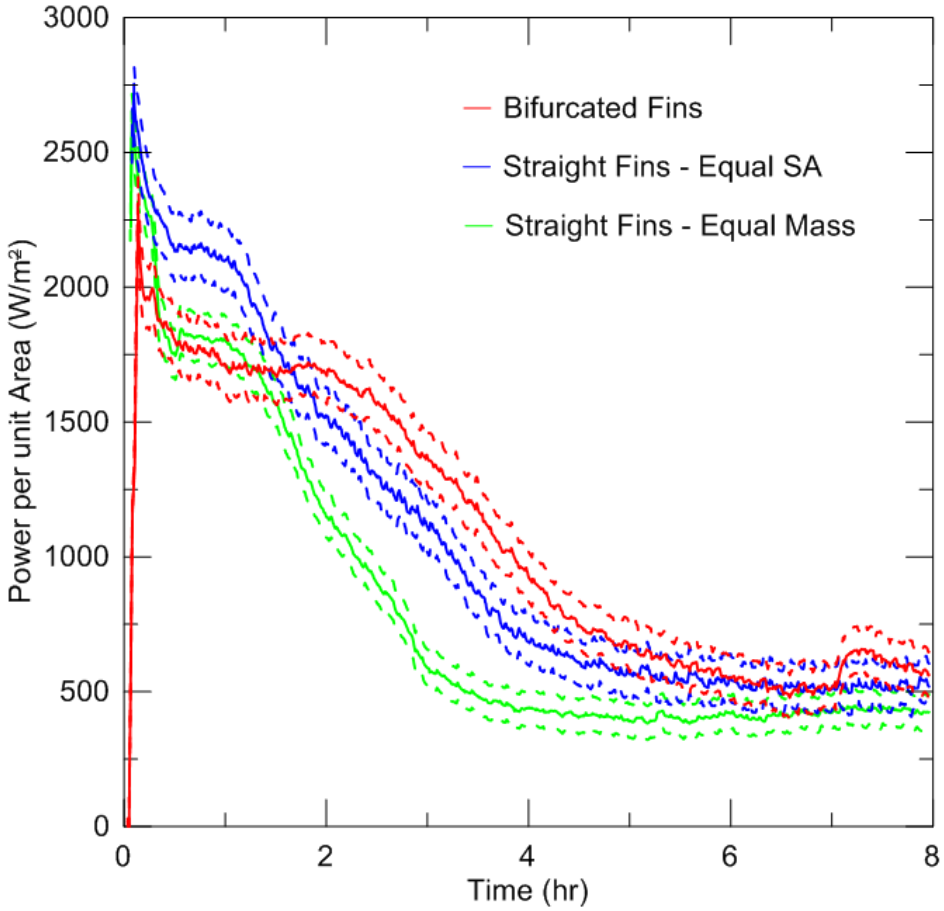

Figure 3.23: Rate of heat transfer profiles per unit of fin area for all three fin types with HTF inlet temperature of 72.5 °C

Figure 3.24 shows the heat transfer rate profiles from Figure 3.22 shifted downwards by 75 W to account for ambient losses.

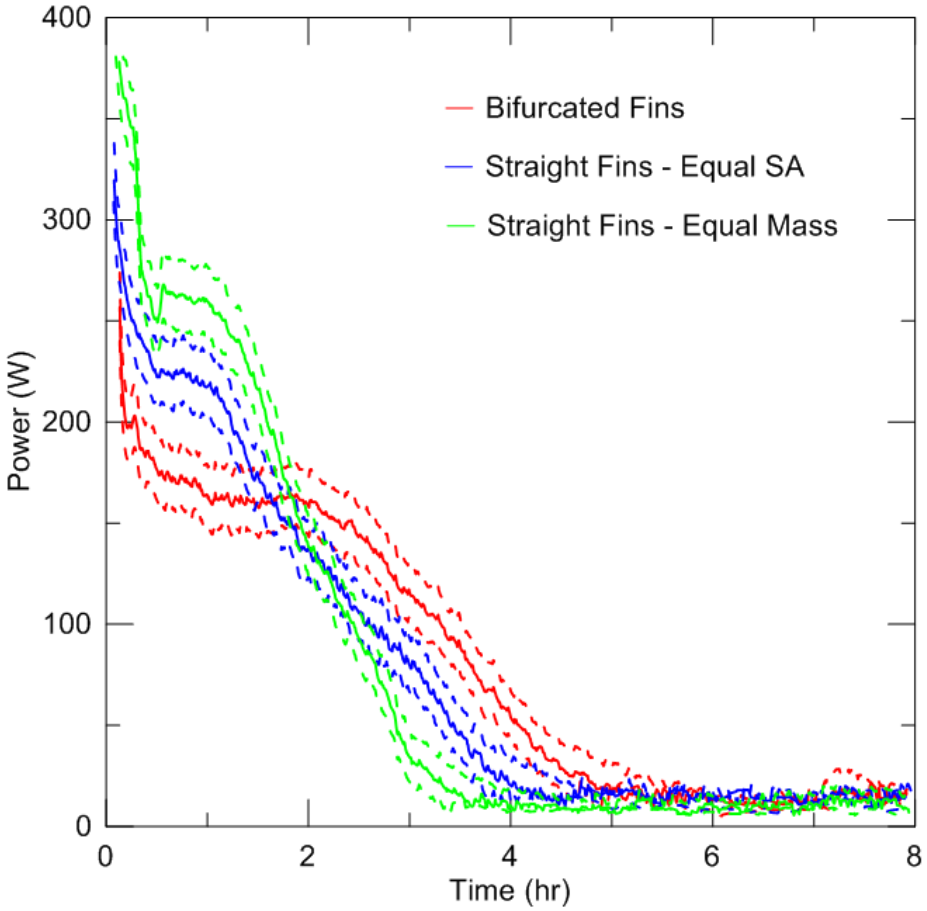

Figure 3.24: Rate of heat transfer profiles for all three fin types with HTF inlet temperature of 72.5 °C corrected to account for ambient losses

Figure 3.25 shows the heat transfer per unit fin area profiles, also corrected to account for the 75 W of losses to the environment.

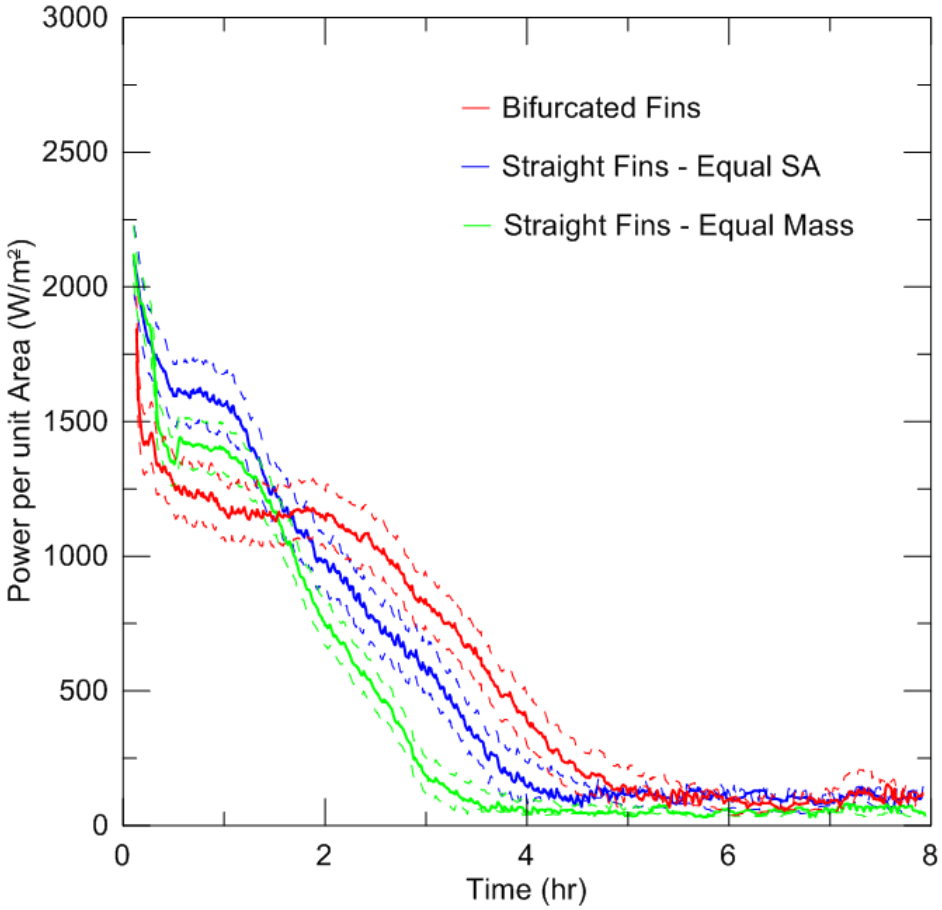

Figure 3.25: Rate of heat transfer profiles per unit of fin area for all three fin types with HTF inlet temperature of 72.5 °C corrected to account for ambient losses

The temperature profiles collected from the HTF inlet and outlet, as well as within the PCM mass, can be used to form a general picture of the heat transfer characteristics for each fin type. Overall, the bifurcated fins provided a slower rate of heat transfer over a longer period of time compared to the straight fins. The longer straight fins also showed a higher rate of heat transfer than the shorter straight fins, as expected due to their greater surface area. The most notable difference between the fin types was seen with the 62.5 °C HTF inlet condition. During these tests, the bifurcated fins were not able to bring the PCM to a steady-state temperature within the 8-hour period, while the straight finned exchanger displayed no difficulty in doing so. A possible explanation for this difference is the proximity of the fins to each other in the straight-finned exchangers. The PCM in these narrow cavities should melt more quickly than it does in the larger gaps between the bifurcated fins. Once

a cell of PCM has become liquid, it is able to carry heat through convection and thus significantly increase the rate of heat transfer in the system.

Chapter 4. ENERGY AND EFFECTIVENESS COMPARISONS

The purpose of a LHESS is to store energy received from a HTF stream and then release it back later. Therefore, when comparing different LHESS heat exchangers it is important to quantify the amount of energy within the system over time. Knowing the inlet and outlet temperatures of the HTF, the energy delivered or removed from the system may be calculated according to Eq. (4.1).

$$E = \int_{t_i}^{t_f} \dot{m} c_p \Delta T \, dt \tag{4.1}$$

where E is the energy lost or gained by the HTF over the interval t_i to t_f, $\dot{m}$ is the mass flow rate of the HTF, c_p is the heat capacity of the fluid, and ΔT is the temperature difference between the inlet and outlet thermocouples. The theoretical change of energy of the PCM may be calculated by Eq. (4.2).

$$\Delta E_{PCM} = m c_p \Delta T + \varphi m L \tag{4.2}$$

where ΔE_{PCM} is the energy change of the PCM, m is the mass of the PCM, c_p is the heat capacity of the PCM, ΔT is the temperature change of the PCM, φ is the fraction of PCM that has changed phase, and L is the latent heat of the PCM. Equation (4.2) is difficult to apply, however, because it requires that the overall temperature of the PCM be known. For the experiments performed in this work, the PCM temperature change may be approximated using the HTF setpoint temperature of the current experiment and that of the previous experiment. Assuming that most of the PCM mass reached a steady-state temperature close to the driving temperature at the end of each experiment, the difference in setpoint temperatures should be close to the actual change in PCM temperature. Equation 4.2, used that way, therefore provides the maximum theoretical amount of energy can could be stored or removed from the PCM in a specific experiment. The mass of the copper heat exchanger is approximately 1.3 kg, meaning that it contributes approximately 0.5 kJ/K (0.00014 kWh/K) of additional thermal storage. For the texted temperature ranges, the proportion of energy storage contributed by the copper was less than the uncertainty of the energy calculations, therefore it was neglected.

Figure 4.1 shows the energy profiles calculated from the integral in Eq. (4.1) for the three heat exchangers under discharge conditions, with the HTF inlet temperature set to 22.5 °C.

The dotted profiles show the uncertainty range of the energy profiles, calculated by integrating the maximum and minimum heat transfer rates. The uncertainty increases over time due to the accumulating effect of the integration. Also shown is the theoretical energy change of the PCM as a black dotted line, calculated according to Eq. (4.2) and assuming a complete change of phase. The change in the heat capacity of the PCM with temperature is accounted for using a linear fit approximation of the data presented by Desgrosseilliers *et al.* (2013). None of the energy profiles reach the theoretical change in PCM temperature, suggesting that not all of the PCM had changed phase by this point. Any energy that the PCM lost to the environment would not be captured in the energy profiles, causing them to undershoot the theoretical PCM energy change.

The energy profiles show that the shorter-straight fins initially remove the most energy from the system, although the longer straight fins overtake the shorter ones between the two and three-hour mark. The bifurcated fins remove energy more slowly, and do not catch up to the longer straight fins within the 8-hour period.

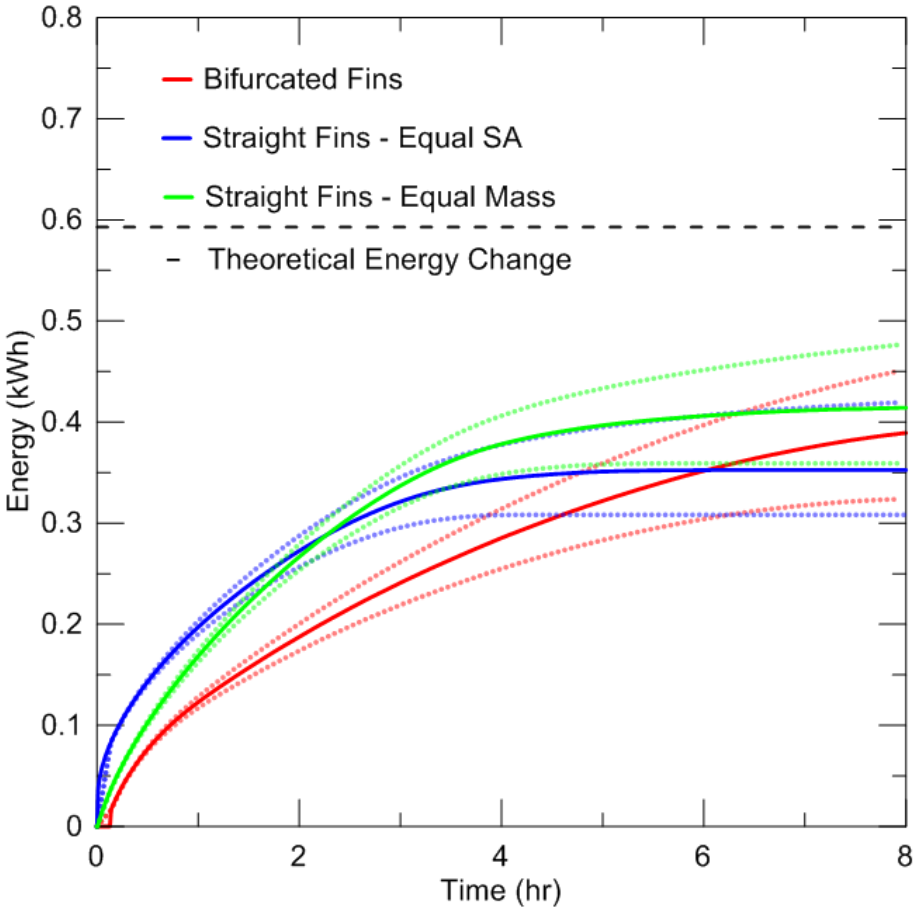

Figure 4.1: Cumulative energy profiles for all three fin types under discharge conditions, HTF temperature of 22.5 °C

For the discharge experiments at 12.5 °C, the HTF thermocouples would sometime report a small loss of temperature in the HTF on the order of 0.04 °C. This loss of HTF temperature results in a negative rate of heat transfer, implying that the PCM or the environment absorbed energy from the cool HTF stream. In order to determine what was actually happening in this case, the inlet and outlet thermocouples were retested in the calibration bath after the end of the experiment. Figure 4.2 shows the difference between the outlet and inlet HTF thermocouples when submerged in a bath of oil maintained at 12.5 °C. Over the test period, the outlet thermocouple consistently read a higher temperature than the inlet thermocouple, with an average difference of 0.03 °C over the run-time. At 12.5 °C the mass flow rate of the HTF stream was 0.05 kg/s, and the heat capacity is 4.19 kJ/kg·K, thus the apparent rate of heat transfer caused by this temperature difference is

0.006 kW. Over eight hours, that rate of heat transfer results in 0.05 kWh of deficit in the amount of stored energy, between 10-15% of the total energy discharged over the course of the experiment. The energy plots for the discharge experiment run with 12.5 °C HTF have been corrected to account for this bias.

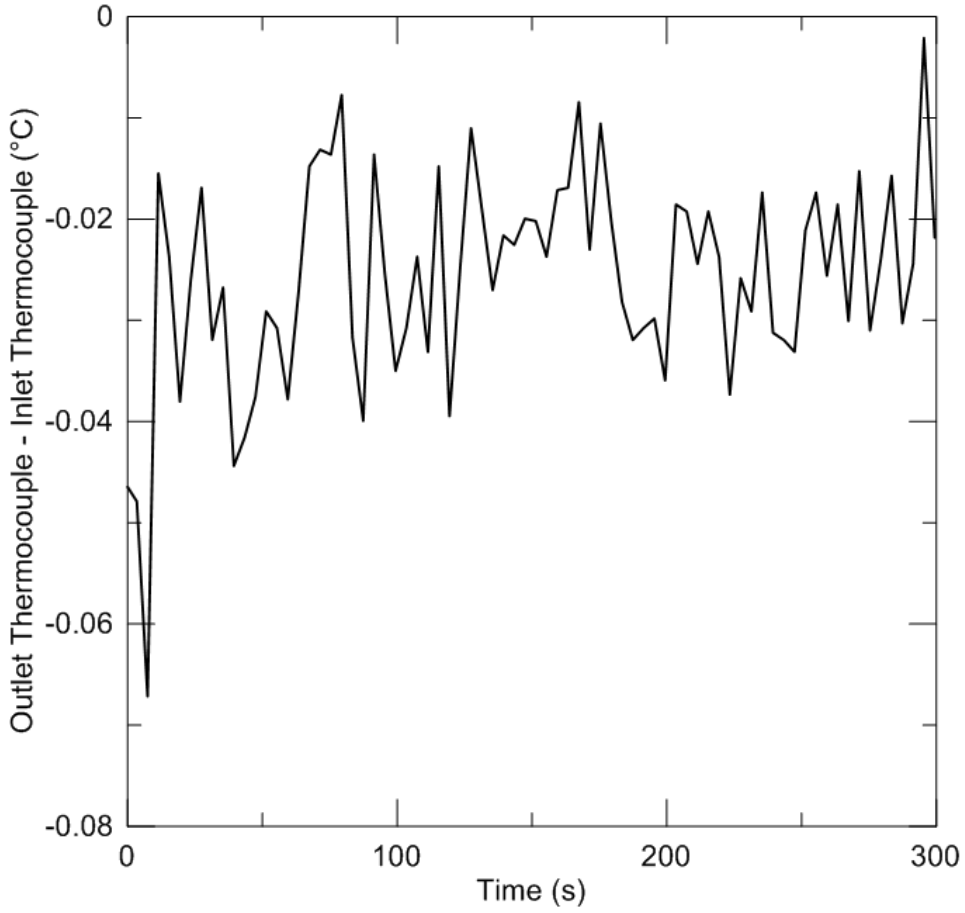

Figure 4.2: Difference between outlet and inlet HTF thermocouple when submerged in constant-temperature bath at 12.5 °C

Figure 4.3 shows the energy profiles for the three heat exchangers during discharging with HTF set to 12.5 °C. Both the long-straight fins and the bifurcated fins removed the same amount of energy during these experiments, but the long-straight fins extracted the energy in around half the time taken by the bifurcated fins. The short-straight fins extracted energy more slowly than the straight fins and more quickly than the bifurcated fins, but were unable to extract energy past the 3-hour mark. At this stage the HTF thermocouples used

in the short-straight fin experiment begin to record negative heat transfer rates, which have been corrected to 0 W, hence the flattening out of the profile. All three profiles have been corrected to account for the 0.03 °C temperature bias between the outlet and inlet HTF thermocouples.

As with the experiments performed with 22.5 °C HTF inlet fluid, none of the energy profiles reach the theoretical PCM energy change. It is possible that some of the PCM mass remains in the liquid phase by the end of the 8-hour runtime, in which case the theoretical PCM energy change would be overestimated. In the case of the short-straight finned exchanger, it is likely that a significant portion of the PCM did not solidify and that some of the PCM energy escaped to the surroundings before it could be captured by the HTF stream.

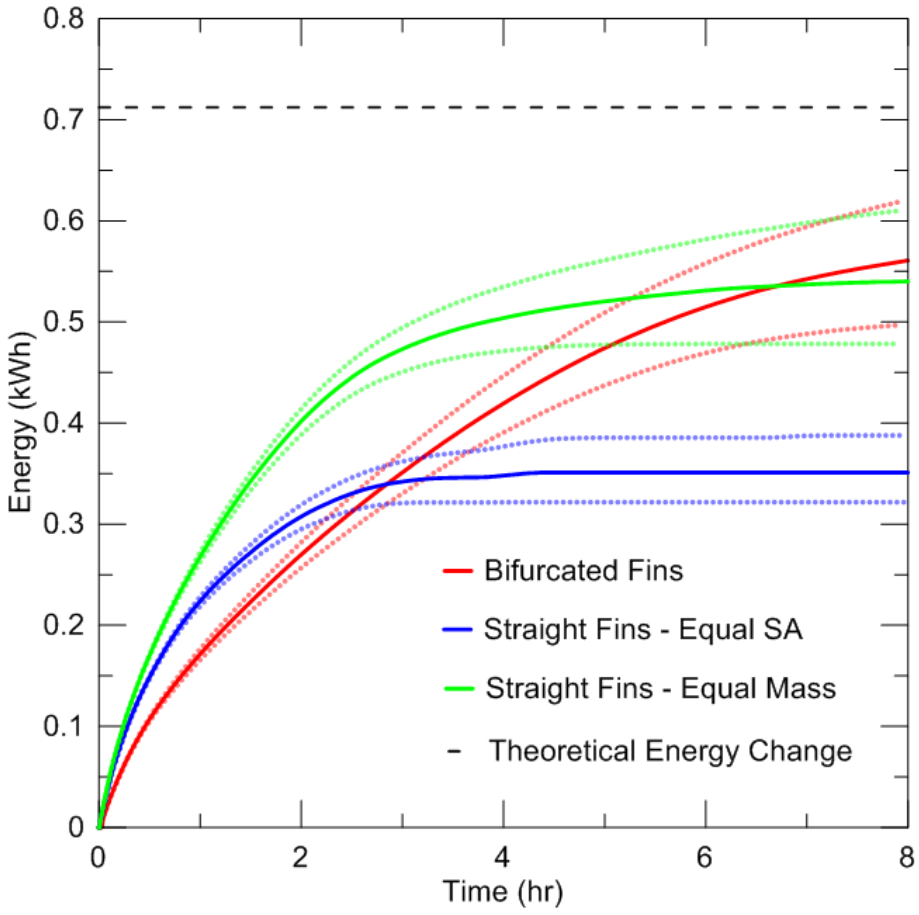

Figure 4.3: Cumulative energy profiles for all three fin types under discharge conditions, HTF temperature of 12.5 °C, corrected for thermocouple bias

Figure 4.4 shows the energy profiles for the three heat exchangers during charging with HTF set to 72.5 °C, calculated from the heat transfer rate profiled corrected for ambient losses. The three profiles are very similar, with the longer straight fins providing peak energy storage the soonest at the 3-hour mark. The short-straight fins catch up to the long-straight fins before the 4-hour point, and the bifurcated fins reach the plateau after the 5-hour mark.

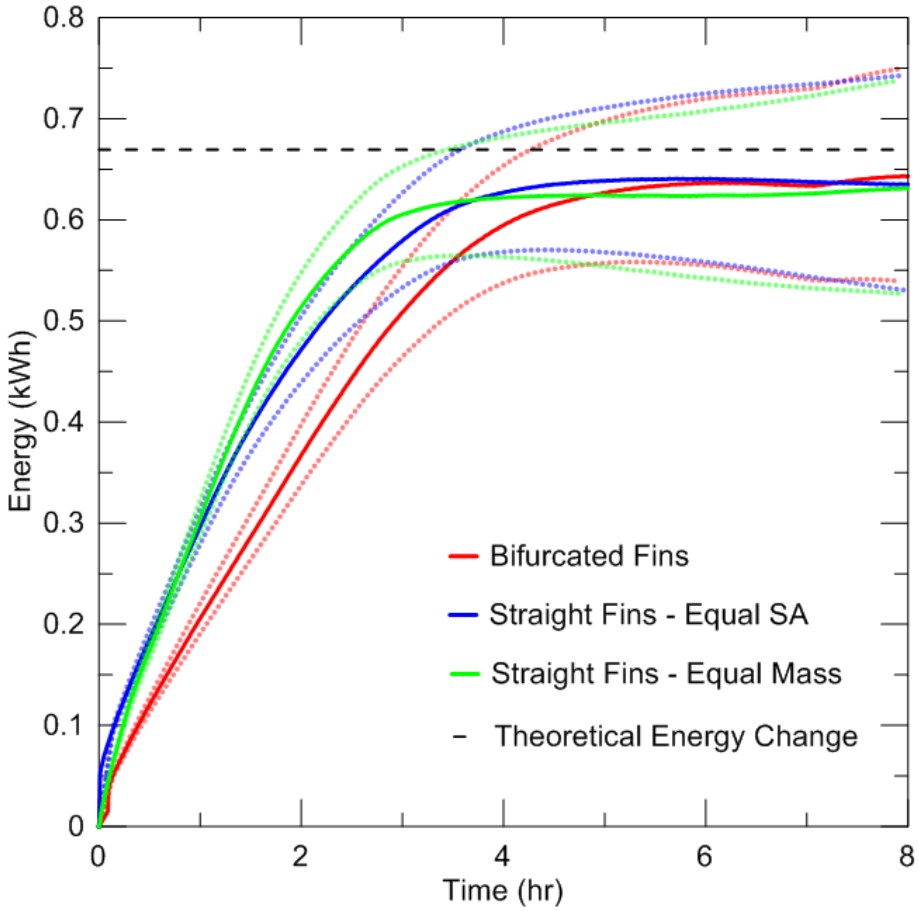

Figure 4.4: Cumulative energy profiles for all three fin types under charging conditions, HTF temperature of 72.5 °C

Figure 4.5 shows the energy profiles for the three heat exchangers during charging with HTF set to 62.5 °C. The energy profiles of the two straight fin types are the same for this HTF temperature, while the bifurcated fin profile does not reach the same plateau during the 8-hour test period.

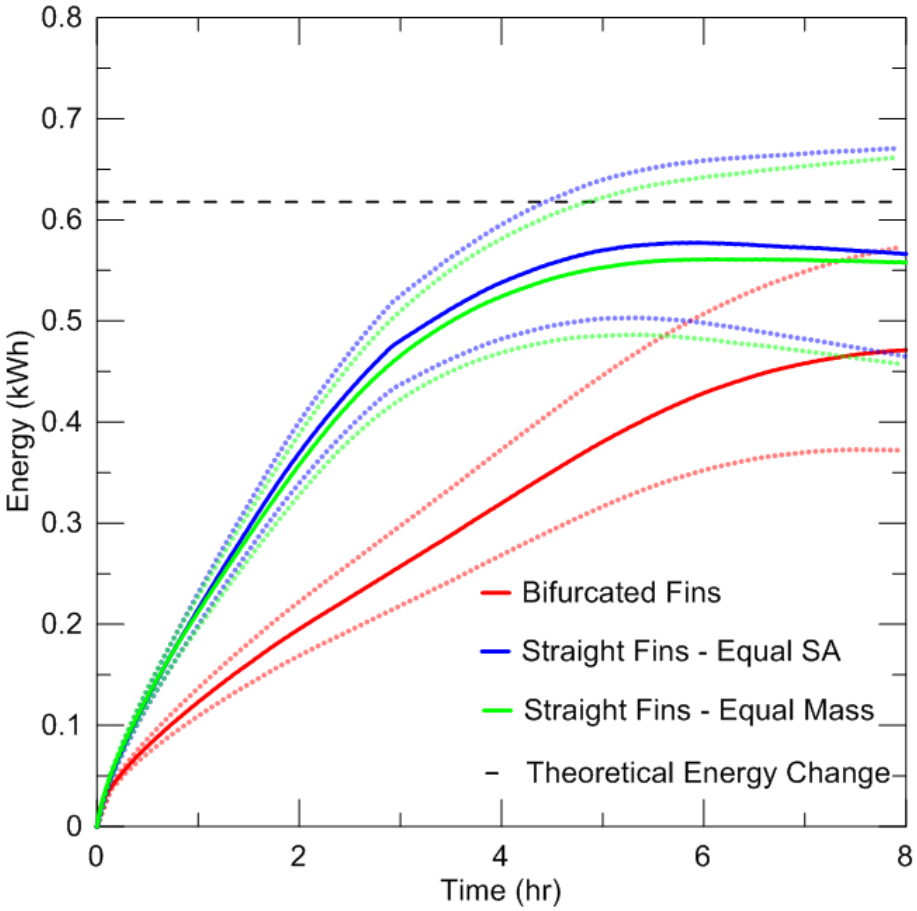

Figure 4.5: Cumulative energy profiles for all three fin types under charging conditions, HTF temperature of 62.5 °C

Table 4.1 shows the estimated change in energy of the PCM during each of the discharging experiments, calculated from the HTF inlet temperature of that experiment and the HTF inlet temperature of the previous experiment. Also shown is the total measured energy transferred between the PCM and the HTF stream. Overall, the energy delivered by the HTF during the discharge experiments is less than the theoretical change in PCM energy based on the thermocouple readings. The most likely cause for this discrepancy is that the PCM has not completely solidified throughout the container, and thus the theoretical energy change is an overestimation. This issue could be addressed in future experiments by placing thermocouples in the corners of the PCM container and using them to gauge when the phase change process was complete. Alternatively, running the experiments for a longer period of time would help guarantee that all of the PCM had changed phase. For

these discharging experiments, the long-straight and the bifurcated fins were able to extract more energy from the PCM compared to the short-straight fins during the 8-hour time span. This difference likely results from the diminished reach of the short-straight fins into the PCM mass compared to the other two geometries. Once the shorter fins are completely engulfed by the solidification front, their impact on the remaining molten PCM is expected to be limited compared to longer fins. Interestingly, the short-straight fins extracted less total energy when the HTF was at 12.5 °C compared to at 22.5 °C. This could be the result of the solidification front overtaking the shorter fins more quickly, thereby reducing the time the fins spend in contact with the liquid PCM and thus the rate of heat transfer during the 8-hour testing time.

In addition, the average effectiveness of the heat exchanger is calculated according to Eq. (4.3).

$$\varepsilon = \frac{T_{in} - T_{out}}{T_{in} - T_{PCM}} \tag{4.3}$$

where ε is the effectiveness of the heat exchanger, T_{in} is the inlet temperature of the HTF, T_{out} is the outlet temperature of the HTF, and T_{PCM} is the phase-change temperature of the PCM. The inlet and outlet temperatures change over the course of the experiment, so the mean effectiveness averaged over the 8-hour period is presented in Table 4.1. For the discharge experiments, the average effectiveness of the bifurcated fins is about the same as the long-straight fins over the course of the 8-hour experiment. The short-straight fins showed lower effectiveness figures for the discharging experiments compared to the other two fin types, especially when the HTF inlet temperature was set to 12.5 °C.

Table 4.1: Theoretical and measured energy changes for discharging experiments

Fin Type	HTF T_{inlet} (°C)	HTF $T_{inlet,\ previous}$ (°C)	PCM ΔT (±1.1 K)	Theoretical ΔE_{total} (± 0.04 kWh)	HTF ΔE (kWh)	ε_{mean} (±0.05)
Bifurcated	22.5	62.5	40.0	0.59	0.39 ±0.07	0.013
	12.5	72.5	60.0	0.71	0.52 ±0.07	0.011
Short-Straight	22.5	60.0	37.5	0.58	0.35 ±0.08	0.010
	12.5	72.5	60.0	0.71	0.33 ±0.07	0.006
Long-Straight	22.5	62.5	40.0	0.59	0.41 ±0.07	0.014
	12.5	72.5	60.0	0.71	0.49 ±0.08	0.010

Table 4.2 shows the energy results for the charging experiments, including both the raw values of energy transfer and those corrected to account for losses to the ambient. The corrected values for energy delivery via the HTF are in all cases close to the theoretical value calculated from the PCM thermocouples. The HTF energy measurements tend to overestimate the energy delivered compared to the PCM thermocouples, likely due to energy losses that were not accounted for.

For the charging experiments, all three fin types delivered similar amounts of energy over the 8-hour time period and also demonstrated roughly the same average effectiveness. As seen from the rate of heat transfer profiles for these three fin types, all of them converged during the latter half of each experiment, especially for the HTF inlet temperature on 72.5 °C. The presence of natural convection in the molten PCM during these charging experiments may be masking the differences in the heat transfer characteristics of the three fin types. The only exception is the experiment run with the bifurcated fins with a HTF inlet temperature of 62.5 °C. As shown in the temperature profiles for that experiment, it took much longer to melt the PCM in the region around the fins compared to the cases with the straight fins. For a HTF temperature of 72.5 °C, however, the bifurcated fins deliver as much energy as the other two types. There may be a critical HTF inlet temperature between 72.5 °C and 62.5 °C where the heat transfer performance of the bifurcated fins begins to deviate significantly from the straight-finned exchangers.

Table 4.2: Theoretical and measured energy changes for charging experiments

Fin Type	HTF T_{inlet} (°C)	HTF $T_{inlet,\ previous}$ (°C)	PCM ΔT (±1.1 K)	Theoretical ΔE_{total} (± 0.04 kWh)	HTF ΔE (kWh)	Corrected HTF ΔE (kWh)	ε_{mean} (±0.05)
Bifurcated	60.0	12.5	47.5	0.62	0.95 ±0.11	0.47 ± 0.11	0.034
	72.5	22.5	50.0	0.67	1.23 ±0.11	0.63 ±0.11	0.026
Short-Straight	62.5	12.5	50.0	0.64	1.04 ±0.11	0.56 ±0.11	0.032
	72.5	22.5	50.0	0.67	1.24 ±0.11	0.64 ±0.11	0.026
Long-Straight	62.5	12.5	50.0	0.64	1.04 ±0.11	0.56 ±0.11	0.032
	72.0	22.5	49.5	0.67	1.23 ±0.11	0.63 ±0.11	0.024

Figure 4.6 shows the effectiveness of the three heat exchangers over time while discharging the PCM, plotted on a logarithmic scale. From these plots, it appears that the long straight-finned exchanger has the highest effectiveness at the beginning of the discharge experiments, while the bifurcated exchanger shows the greatest long-term effectiveness. These trends follow the same pattern as the rates of heat transfer, whereby the straight-fins reach a steady-state temperature sooner than the bifurcated fins, which is accompanied by a decrease in the HTF temperature difference across the exchanger. During the 12.5 °C HTF inlet discharge experiment, the effectiveness begins to rise again after the 4-hour mark, despite the rate of heat transfer having dropped to 0 W by this stage. This anomalous rise is likely due to the HTF thermocouple bias reporting a small negative temperature change, which become visible once the heat transfer process has stopped.

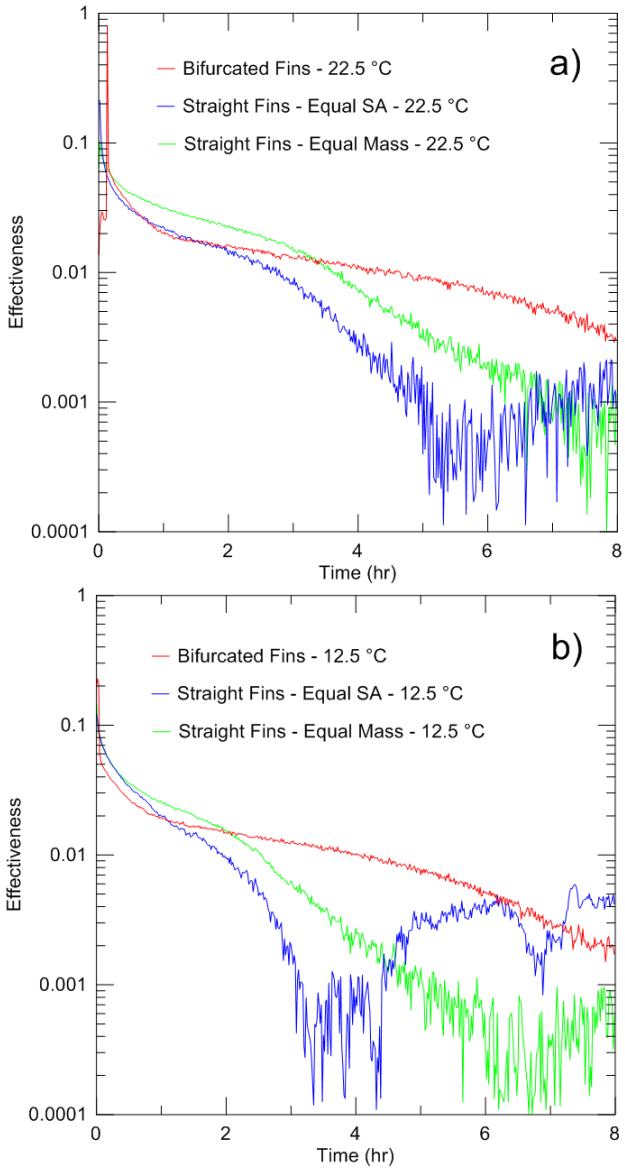

Figure 4.6: Effectiveness of heat exchangers with HTF inlet temperatures of 22.5 °C (a) and of 12.5 °C (b)

Figure 4.7 shows the effectiveness of the three heat exchangers over time while charging the PCM, plotted on a logarithmic scale. The effectiveness was calculated using the temperature values taken directly from the experiment, with no corrections made to account for what the temperatures would be without losses to the environment. With the HTF inlet temperature of 62.5 °C all three heat exchangers demonstrate similar effectiveness over time. The bifurcated fins initially perform slightly less effectively during the first three hours, but perform more effectively than the straight-finned exchangers after this point. As noted with the rate of heat transfer plots, the bifurcating finned exchanger takes longer to

bring the PCM to a steady-state temperature, thus the effectiveness profiles are comparing different states of charge for any given time. With a HTF inlet temperature of 72.5 °C, the longer-straight fins consistently provide the greatest effectiveness over the test period.

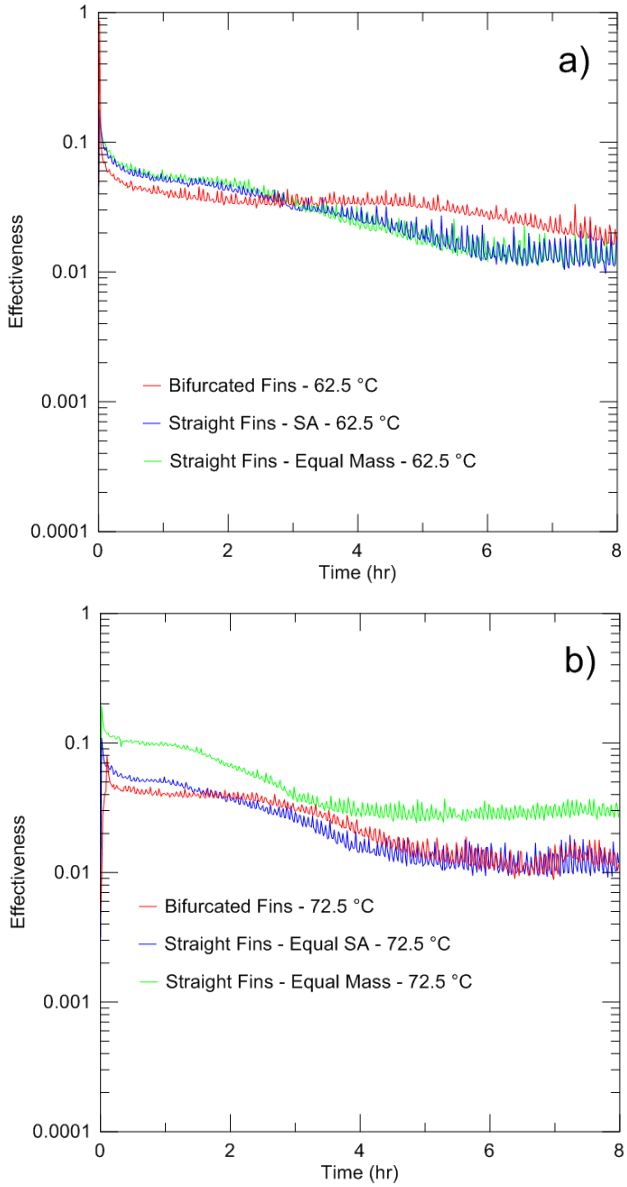

Figure 4.7: Effectiveness of heat exchangers with HTF inlet temperatures of 62.5 °C (a) and of 72.5 °C (b)

In addition to effectiveness, an important metric of the utility of a heat exchanger is the absolute amount of energy it can provide in a given time period. Figure 4.8 shows the

amount of cumulative energy transferred by each exchanger over four hours and eight hours at the various HTF inlet temperature setpoints. Four hours was chosen as one of the comparison times because during each charging experiment at least one of the heat exchangers reached steady-state by the 4-hour mark. From the two plots, it can be seen that the energy transferred by the straight fins does not change very much during the last four hours of each experiment, while the bifurcated fins continue to transfer energy. The error bars for these plots are relatively large, as the uncertainty is accumulated by the integration of the rate of heat transfer data. The greatest source of uncertainty is the temperature readings from the thermocouples in the HTF stream, which depends on temperature. Thus, error of the thermocouples was likely similar for each experiment run at the same HTF inlet temperature. Therefore, the bar plots can be useful for discerning the relative performance between the three heat exchangers at a given HTF inlet temperature, despite the large range of error.

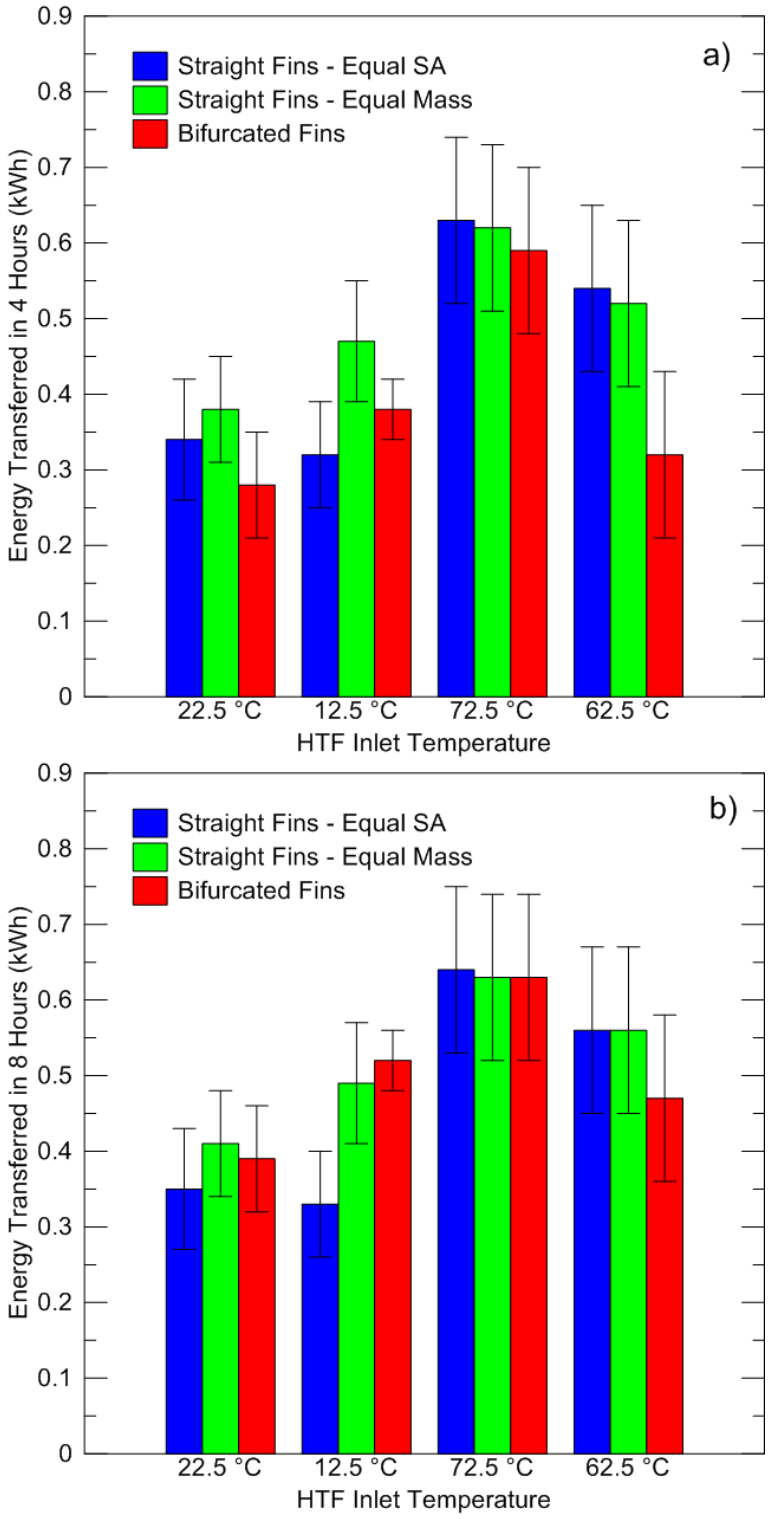

Figure 4.8: Cumulative energy transferred by heat exchangers over 4 hours (a) and 8 hours (b) with different HTF inlet temperatures.

Figure 4.9 shows the percentage difference in energy transferred by the bifurcated fin and the two straight-finned exchangers after 4 hours and then 8 hours. Based on the 4-hour data, the long-straight fins provided the best performance during discharging, while the short-straight fins provide the best performance during charging. The bifurcated fins do perform 15.8 % better than the short-straight fins during discharge at 12.5 °C, but this improvement is overshadowed by the further 23 % increase in performance provided by the long-straight fins compared to the bifurcated ones. After 8 hours, bifurcated fins have delivered more energy than the shorter-straight fins during discharging, slightly less energy than the shorter straight fins when charging with 72.5 °C HTF, and around 20% less when charging with 62.5 °C HTF. Compared to the longer-straight fins, the bifurcated fins transferred around 5% less energy when discharging with 22.5 °C HTF, around 5% more energy when discharging with 12.5 °C, the same amount of energy when charging with 72.5 °C, and 20% less energy when charging with 62.5 °C HTF.

These percentages may also be used to determine the costs at which each fin type becomes worthwhile compared to the other fins, which will be addressed in the next chapter.

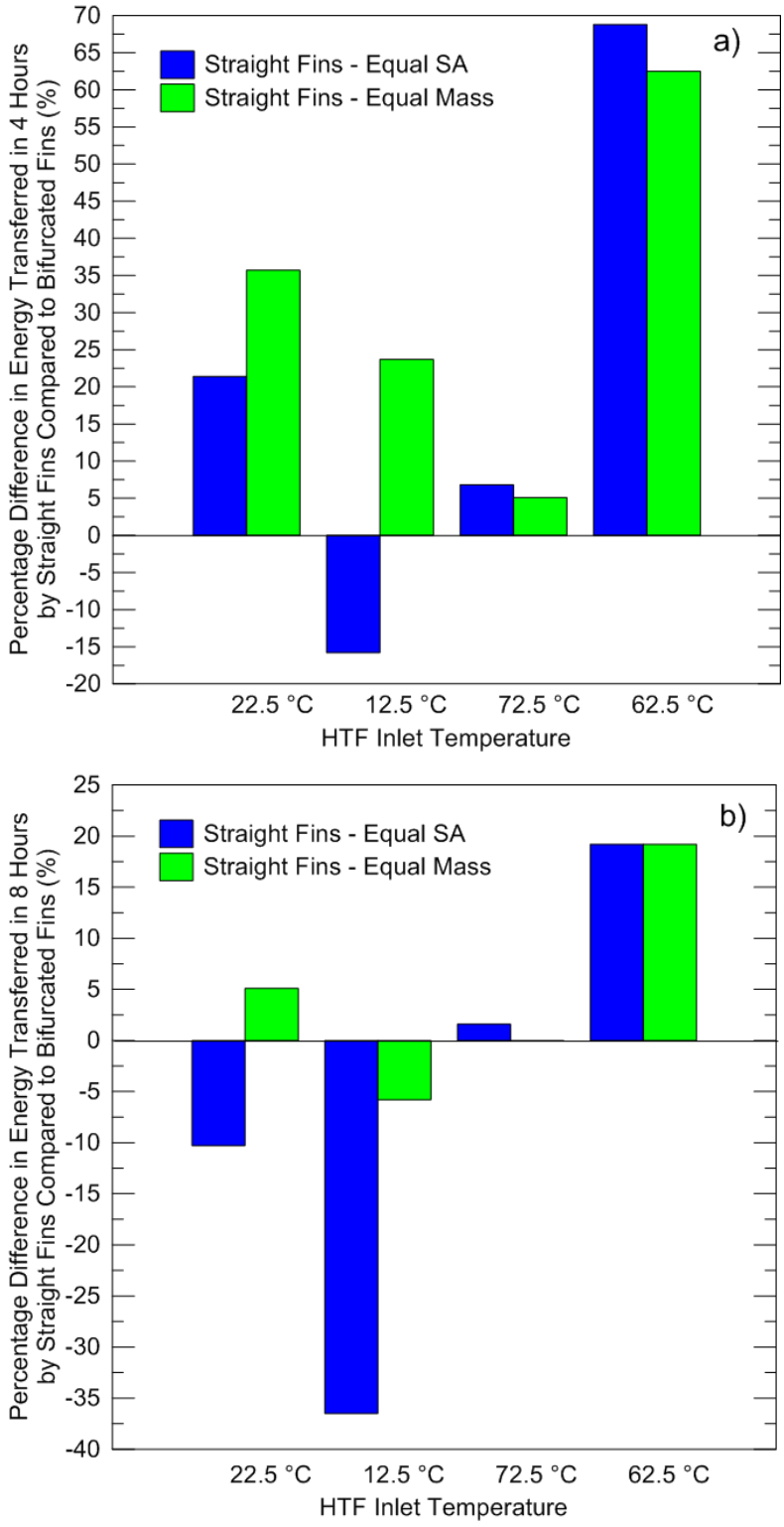

Figure 4.9: Percentage difference in cumulative energy transferred over 4 hours (a) and 8 hours (b) between the straight fins and the bifurcated fins

Chapter 5. COST BENEFIT ANALYSIS

When evaluating the heat transfer performance provided by various fin geometries, it is important to also understand the costs required to achieve those shapes. Although bifurcated fins like the ones investigated in this study are not available commercially, it is possible to provide a rough estimate of their manufacturing cost. Table 5.1 shows the price of the copper sheet purchased to create the fins used in this study, as well as the fractional cost of a single strip of the sheet. The 12-inch strips of copper were used to make the bifurcated fins and the long-straight fins, while the 9-inch strips were used to make the short-straight fins.

Table 5.1: Material costs of copper sheet for fin manufacturing

Material	Cost (CAD)
2’ x 3’ sheet of 0.024” thick copper	$ 55.26
12” x 3” strip of copper	$ 2.30
9” x 3” strip of copper	$ 1.73

Table 5.2 shows the various operations required to manufacture the fins from the sheet of copper. The first stage is cutting the sheet into strips. It takes 1 minute to set the sheet-cutter to the correct length, and then 5 second to cut and collect each strip. A sheet can be turned into 24 strips, so the total time per strip is 0.13 minutes. The strips of copper can then be folded into the bifurcated design, which takes around 4 minutes per strip. Next, the holes are drilled into the strips, it takes around 5 seconds to carefully drill one hole and 15 seconds to secure and unsecure the fin to the drill press. Straight fins span the entire width of the heat exchanger before they are cut in half and thus require two holes each, while bifurcated fins require only 1. Once the holes are drilled, the fins can be soldered onto the heat exchanger pipes, which takes around 45 seconds for each hole.

Table 5.2: Manufacturing time estimates per fin in minutes

Operation	Straight	Bifurcated
Cutting	0.13 min	0.13 min
Folding	0.00 min	4.00 min
Drilling	0.58 min	0.42 min
Soldering	1.00 min	1.00 min
Total	**2.21 min**	**5.29 min**

Assuming that the fins are produced by hand at a rate of $40 per hour for labour, then the total estimated cost per fin are as shown in Table 5.3.

Table 5.3: Estimated cost per fin

	Short-Straight	Long-Straight	Bifurcated
Cost per fin (CAD)	$ 3.09	$ 3.66	$ 5.77

Table 5.4 shows the estimated fin costs divided by the energy transferred with each heat exchanger in 4 hours. For HTF at 22.5 °C, 72.5 °C and 62.5 °C, the short-straight fins provide the best cost-to-energy ratio. For HTF at 12.5 °C, the long-straight fins are the most cost-effective. The bifurcated fins are consistently more expensive than the other fin types in terms of the energy they can deliver in a given time period.

Table 5.4: Cost of fins per kWh of energy delivered in 4 hours with various HTF inlet temperatures

	Cost per fin per kWh of energy delivered in 4 hours (CAD/kWh)		
HTF Inlet Temperature	Short-Straight	Long-Straight	Bifurcated
22.5 °C	$9.09	$9.63	$20.61
12.5 °C	$9.66	$7.79	$15.18
72.5 °C	$4.90	$5.90	$9.78
62.5 °C	$5.72	$7.04	$18.03

Table 5.5 shows the estimated fin costs divided by the energy transferred with each heat exchanger over 8 hours. The bifurcated fins see a notable drop in cost per kWh due to the increase in energy delivered over the longer time period, but the overall trends in price between the fin types remains the same as with the 4-hour evaluation.

Table 5.5: Cost of fins per kWh of energy delivered in 8 hours with various HTF inlet temperatures

	Cost per fin per kWh of energy delivered in 8 hours (CAD/kWh)		
HTF Inlet Temperature	Short-Straight	Long-Straight	Bifurcated
22.5 °C	$8.83	$8.93	$14.80
12.5 °C	$9.36	$7.47	$11.10
72.5 °C	$4.83	$5.81	$9.16
62.5 °C	$5.52	$6.54	$12.28

Examining the total energy transferred at the 4 and 8-hour points captures the differences between the three heat exchangers used in the LHESS. Most thermal storage applications, however, operate on time scales much shorter than 4 or 8 hours. Hot water demand in a domestic home, for example, often changes on a minute-to-minute basis. Therefore, even if a heat exchanger provides a low cost-to-energy ratio over a particular period of time, if that period of time is greater than what is demanded by the application then the heat exchanger is unsuitable.

The majority of the price difference between the bifurcated and the straight fins is due to the time taken to fold them. This folding time could potentially be reduced through practice, or by using a customized manufacturing process. Figure 5.1 shows how the estimated price of the bifurcated fin compared to the estimated costs of the two straight fin types for different folding times. If the folding time can be brought down to 0.8 minutes, then the cost of the bifurcated fin becomes comparable to that of the long-straight fin. As the folding

time approaches 0 minutes, the cost of the bifurcated fin approaches the cost of the short fins.

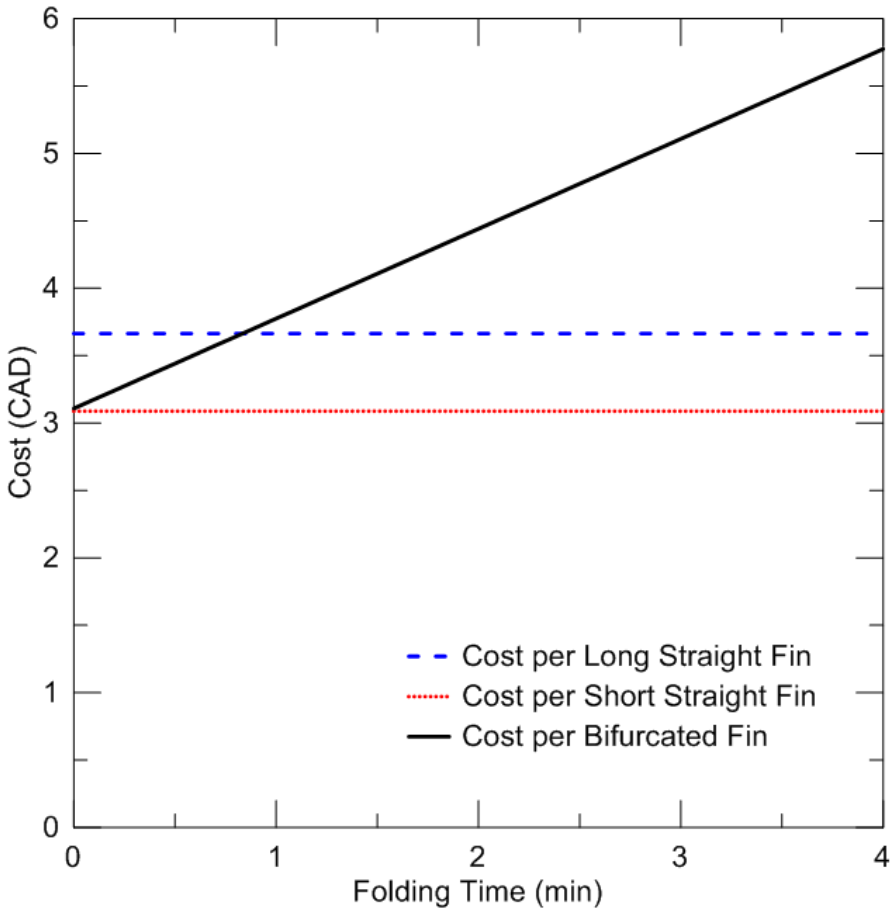

Figure 5.1: Estimated manufacturing costs of fin geometries for different folding times

Table 5.6 shows the cost-to-energy ratios for the fins after 4 hours of heat transfer, completely discounting the folding cost of the bifurcating fins. Even with the cheapest bifurcating fins, one of the straight fin types remains the most cost-effective option for each HTF inlet temperature after 4 hours of use.

Table 5.6: Cost of fins per kWh of energy delivered in 4 hours, discounting the cost of folding

	Cost per fin per kWh of energy delivered in 4 hours (CAD/kWh)		
HTF Inlet Temperature	Short-Straight	Long-Straight	Bifurcated
22.5 °C	$9.09	$9.63	$11.10
12.5 °C	$9.66	$7.79	$8.18
72.5 °C	$4.90	$5.90	$5.27
62.5 °C	$5.72	$7.04	$9.71

Table 5.7 shows the cost-to-energy ratios for the fins after 8 hours of heat transfer and discounting the folding cost of the bifurcating fins. Over this longer time scale, the bifurcated fins are the cheapest of all three types for discharging, the second cheapest when charging with 72.5 °C HTF, and the most expensive when charging with 62.5 °C HTF.

Table 5.7: Cost of fins per kWh of energy delivered in 8 hours discounting the cost of folding

	Cost per fin per kWh of energy delivered in 8 hours (CAD/kWh)		
HTF Inlet Temperature	Short-Straight	Long-Straight	Bifurcated
22.5 °C	$8.83	$8.93	$7.92
12.5 °C	$9.36	$7.47	$5.94
72.5 °C	$4.83	$5.81	$4.94
62.5 °C	$5.52	$6.54	$6.57

In terms of cost, the bifurcated fins presented in this study are more expensive per unit of energy delivered than the straight fins of equivalent surface area or the straight fins of equal mass. If the cost of the bifurcated fins is reduced, however, then they could potentially be more cost-effective than straight fins during discharge.

Chapter 6. CONCLUSION AND RECOMMENDATIONS

The use of phase change materials is a promising avenue for improving the energy density of thermal storage systems. Most PCMs suitable for domestic use, however, have low thermal conductivities and thus slow rates of heat transfer. In order to overcome this rate problem, it is necessary to improve our understanding of heat transfer processes within multi-phase solid-liquid systems. In particular, the impact of many non-traditional fin geometries for PCM heat exchangers is still poorly understood. Fins that bifurcate into tree-like forms are commonly discussed in works on bio-inspired design, but so far no experimental work on bifurcating fins within PCM has been performed. The objective of this research was to compare the heat transfer rate provided by a heat exchanger outfitted with bifurcated fins for various HTF inlet temperatures to straight fins of equivalent surface area and straight fins of equivalent mass. In pursuit of this objective, a new LHESS test platform was designed an constructed for the LAMTE, and three heat exchangers were manufactured for testing on this platform. The construction of the test platform was successful, and will serve as a fixture for future work in the LAMTE on LHESSs, such as for parametric studies on heat exchanger geometries. These studies can contribute data that may be used to develop correlations for LHESS heat exchanger design. These correlations could dramatically reduce the time and cost of designing LHESSs for new applications by providing guidelines to LHESS designers.

The rates of heat transfer provided by the different exchangers varied relative to each other according to whether the LHESS was being charged or discharged. During discharge experiments, the rates of heat transfer provided by the two straight fin types were initially greater than that provided by the bifurcated fins. Over the course of the experiments, however, the heat transfer rate of the straight fins declined more quickly than that of the bifurcated fins. Thus, for the latter half of the test the bifurcated fins transferred heat more quickly than the other types. Over the total 8-hour run, the bifurcated and long-straight fins transferred similar amounts of energy, but none were able to completely discharge the system in that timeframe. The shorter straight fins in particular transferred much less energy than the other two fin types when the HTF was maintained at 12.5 °C. The

performance difference between the short-straight fins and the other two types could be attributed to the reduced reach of those fins into the PCM body. The dominant mode of heat transfer during discharge is conduction, which decreases significantly once the heat exchanger is completely encased in solid PCM. The shorter fins should become entirely enveloped by the solidification front sooner than the bifurcated or long-straight fins, and thus would be experience greatly reduced rates of heat transfer relative to the furthest edges of the PCM container.

During charging experiments, the bifurcated fins showed a lower rate of heat transfer than the other two fin types during the beginning of each test, and then a higher rate by the end of the experiment. When the HTF inlet temperature was set to 72.5 °C, all three fin types delivered similar quantities of energy during the 8-hour run. This convergence most likely occurs due to the presence of natural convection in the molten PCM. Once the melting front has progressed far enough to allow for free convection to develop, the overall rate of heat transfer becomes less dominated by the specific geometry of the fins. The bifurcated fins delivered much less energy than the straight fin types when the HTF was set to 62.5 °C. It is likely that the smaller distance between adjacent straight fins leads to the more rapid development of convection cells, whereas the bifurcated-fins require more time to melt enough PCM for convection to be possible.

In terms of cost-effectiveness, the bifurcated fins were shown to be more expensive per kWh of energy delivered over 4 or 8 hours if they are manufactured with the process used for this study. If the cost of producing the bifurcated fins can be reduced, then they could potentially be more cost-effective than straight fins of equivalent surface area when used to discharge a LHESS with 7 kg of dodecanoic acid and with HTF of 22.5 °C or 12.5 °C. It should be noted, however, that the LHESS used in this study is not representative of a system that would be used in a commercial application. Thus, the reported rates of heat transfer are useful only in terms of comparison between the three heat exchangers.

The numerical studies on bifurcated fins available in the literature suggest that bifurcated fins should provide greater rates of heat transfer than straight fins of equivalent mass. This

trend was not seen in the experimental results. There are a few factors that could have reduced the performance of the bifurcated fins used in the experiments compared to those studied in the literature. In this study, the bifurcated fins were spread much further apart from each other than the straight fins, while in the literature the spacing is usually held constant between the fin types. In addition, the folding method used to manufacture the bifurcated fins results in a Y-shape with one thick branch being thicker than the stem and the other branch. The ideal bifurcating fins studied in the literature generally have thinner branches than the stem, which is a more optimal use of material.

Recommendations

Overall, the bifurcating-finned heat exchanger transferred heat over a longer period of time to the PCM than the two straight-finned exchangers at the operating conditions tested in this study. Therefore, this particular design of branching fins is not recommended for situations where rapid transfer of energy is desired, such as residential water heating. Applications where a slow and steady transfer of energy is required, such as storing nighttime temperatures for daytime air cooling, may be a promising application for bifurcating fins.

The work done so far along this line of inquiry has highlighted some recommendations for future work. With regard to the experimental setup, it would be beneficial to place additional thermocouples into the corners of the PCM container. These thermocouples would provide a better idea of when the entire PCM mass had changed phase, allowing for a more accurate estimate of the energy change within the system. Likewise, increasing the run time of the experiments from 8 hours to 12-16 hours would also ensure that the PCM temperature reaches steady state. For the charging experiments significant heat losses were observed, which could be managed through the addition of insulation to any exposed HTF piping, as well as further insulation of the LHESS container.

The bifurcated fin design could potentially be improved through the use of a different folding procedure or a different manufacturing process. In the current design, one branch

of the Y is thicker than the other due to the sequence of folding. This is technically an inefficient use of material, as the conduction through the fin is limited by the thickness at the base of the fin. An improved bifurcating design would have greater thickness in the "trunk" and less thickness in the "branches". Moreover, including some conductive material such as solder to gap where the branches join the trunk of the fin would improve the flow of heat from the base to the tips. An alternative construction method could involve two sheets of copper that are pressed together, providing a simple method branching the fins at any point along the stem.

It was noted that the net energy transfer of the short-straight fins during discharge decreased when the HTF temperature was reduced to 12.5 °C compared to the test run with 22.5 °C HTF. It would be of interest to see how this effect varies with the temperature of the HTF and the length of the fins. The results could provide a minimum length cut-off point to PCM-heat exchanger designers.

In addition, it was noted that during charging the energy delivered by the bifurcated fins decreased by over 30 % between the charging experiments run with 72.5°C HTF and those run with 62.5°C HTF. This difference is likely related to the time taken for natural convection to begin in the PCM, and it would be of interest to observe how the rate of heat transfer varies over HTF temperatures between 62.5 °C and 72.5 °C.

Finally, further parametric studies of PCM-based heat exchanger geometries are required as part of the effort to develop new design equations for analyzing LHESSs. For example, examining the effects of HTF flow rate and temperature for different numbers of fins of a particular shape would help provide an empirical basis for the selection of those variables during design.

References

Agyenim, F., P. Eames and M. Smyth (2009). "A comparison of heat transfer enhancement in a medium temperature thermal energy storage heat exchanger using fins." Solar Energy **83**(9): pp. 1509-1520.

Al-Abidi, A. A., S. Mat, K. Sopian, M. Y. Sulaiman and A. T. Mohammad (2013). "Numerical study of PCM solidification in a triplex tube heat exchanger with internal and external fins." International Journal of Heat and Mass Transfer **61**: pp. 684-695.

Almogbel, M. A. (2005). "Constructal tree-shaped fins." International Journal of Thermal Sciences **44**(4): pp. 342-348.

Amin, N. A. M., M. Belusko and F. Bruno (2014). "An effectiveness-NTU model of a packed bed PCM thermal storage system." Applied Energy **134**: pp. 356-362.

Amin, N. A. M., F. Bruno and M. Belusko (2012). "Effectiveness–NTU correlation for low temperature PCM encapsulated in spheres." Applied Energy **93**: pp. 549-555.

Arena, S., G. Cau and C. Palomba (2015). CFD Simulation of Melting and Solidification of PCM in Thermal Energy Storage Systems of Different Geometry. Journal of Physics: Conference Series. 11 p.

Baby, R. and C. Balaji (2012). "Experimental investigations on phase change material based finned heat sinks for electronic equipment cooling." International Journal of Heat and Mass Transfer **55**(5-6): pp. 1642-1649.

Bejan, A. (1997). "Constructal-theory network of conducting paths for cooling a heat generating volume." International Journal of Heat and Mass Transfer **40**(4): pp. 799-816.

Belusko, M., N. H. S. Tay, M. Liu and F. Bruno (2016). "Effective tube-in-tank PCM thermal storage for CSP applications, Part 1: Impact of tube configuration on discharging effectiveness." Solar Energy **139**: pp. 733-743.

Bergman, T. L., F. P. Incropera and A. S. Lavine (2011). Fundamentals of heat and mass transfer, John Wiley & Sons.

Bonjour, J., L. A. O. Rocha, A. Bejan and F. Meunier (2004). "Dendritic fins optimization for a coaxial two-stream heat exchanger." International Journal of Heat and Mass Transfer **47**(1): pp. 111-124.

Calamas, D. and J. Baker (2013). "Tree-like branching fins: Performance and natural convective heat transfer behavior." International Journal of Heat and Mass Transfer **62**: pp. 350-361.

Castell, A., C. Sole, M. Medrano, J. Roca, L. Cabeza and D. Garcia (2008). "Natural convection heat transfer coefficients in phase change material (PCM) modules with external vertical fins." Applied Thermal Engineering **28**(13): pp. 1676-1686.

Charach, C. and A. Zemel (1992). "Thermodynamic Analysis of Latent Heat Storage in a Shell-and-Tube Heat Exchanger." Journal of Solar Energy Engineering **114**(2): pp. 93-99.

Chiu, J. N. W. and V. Martin (2012). "Submerged finned heat exchanger latent heat storage design and its experimental verification." Applied Energy **93**: pp. 507-516.

Darzi, A. A. R., M. Jourabian and M. Farhadi (2016). "Melting and solidification of PCM enhanced by radial conductive fins and nanoparticles in cylindrical annulus." Energy Conversion and Management **118**: pp. 253-263.

Desgrosseilliers, L. (2012). Heat Transfer Enhancement Using Laminate Film Encapsulation for Phase Change Heat Storage Materials. Mechanical Engineering. Halifax, Dalhousie University. **MASc.**

Desgrosseilliers, L., C. A. Whitman, D. Groulx and M. A. White (2013). "Dodecanoic acid as a promising phase-change material for thermal energy storage." Applied Thermal Engineering **53**: pp. 37-41.

Eslami, M. and M. A. Bahrami (2017). "Sensible and latent thermal energy storage with constructal fins." International Journal of Hydrogen Energy **42**(28): pp. 17681-17691.

Government of Canada (2016) Pan-Canadian Framework on Clean Growth and Climate Change. 85

Groulx, D., A. C. Kheirabadi, L. Desgrosseilliers, M. Kabbara, M. Azad, A. Donaldson, A. Joseph and M. A. White (2016). Working Towards Solving the Rate Problem: Geometric vs Nano-Enhanced PCM Solutions. INNOSTORAGE Conference Ben-Gurion University of the Negev, Israel. 4 p.

Hadiya, J. P. and A. K. N. Shukla (2016). "Experimental thermal behavior response of paraffin wax as storage unit." Journal of Thermal Analysis and Calorimetry **124**(3): pp. 1511-1518.

Hasnain, S. M. (1998). "Review on sustainable thermal energy storage technologies, part 1: heat storage materials and techniques." Energy Conversion and Management **39**(11): pp. 1127-1138.

Ismail, K. A. R., C. L. F. Alves and M. S. Modesto (2001). "Numerical and experimental study on the solidification of PCM around a vertical axially finned isothermal cylinder." Applied Thermal Engineering **21**(1): pp. 53-77.

Ismail, K. A. R. and M. M. Goncalves (1993). "Effectiveness Ntu Performance of Finned Pcm Storage Unit." Computational Modelling of Free and Moving Boundary Problems Ii **6**: pp. 279-286.

Kahwaji, S., M. B. Johnson, A. C. Kheirabadi, D. Groulx and M. A. White (2016). "Stable, low-cost phase change material for building applications: The eutectic mixture of decanoic acid and tetradecanoic acid." Applied Energy **168**: pp. 457-464.

Kahwaji, S., M. B. Johnson, A. C. Kheirabadi, D. Groulx and M. A. White (2017). "Fatty acids and related phase change materials for reliable thermal energy storage at moderate temperatures." Solar Energy Materials and Solar Cells **167**: pp. 109-120.

Kamkari, B., H. Shokouhmand and F. Bruno (2014). "Experimental investigation of the effect of inclination angle on convection-driven melting of phase change material in a rectangular enclosure." International Journal of Heat and Mass Transfer **72**: pp. 186-200.

Kim, D.-K. (2014). "Thermal optimization of branched-fin heat sinks subject to a parallel flow." International Journal of Heat and Mass Transfer **77**: pp. 278-287.

Kurnia, J. C., A. P. Sasmito, S. V. Jangam and A. S. Mujumdar (2013). "Improved design for heat transfer performance of a novel phase change material (PCM) thermal energy storage (TES)." Applied Thermal Engineering **50**(1): pp. 896-907.

Languri, E. M., C. O. Aigbotsua and J. L. Alvarado (2013). "Latent thermal energy storage system using phase change material in corrugated enclosures." Applied Thermal Engineering **50**(1): pp. 1008-1014.

Liu, C. and D. Groulx (2014). "Experimental study of the phase change heat transfer inside a horizontal cylindrical latent heat energy storage system." International Journal of Thermal Sciences **82**: pp. 100-110.

Longeon, M., A. Soupart, J.-F. Fourmigué, A. Bruch and P. Marty (2013). "Experimental and numerical study of annular PCM storage in the presence of natural convection." Applied Energy **112**: pp. 175-184.

Lorenzini, G., R. L. Correa, E. D. dos Santos and L. A. O. Rocha (2011). Constructal Design of Complex Assembly of Fins. Journal of Heat Transfer-Transactions of the Asme. 7 p.

Lorenzini, G. and L. A. Oliveira Rocha (2006). "Constructal design of Y-shaped assembly of fins." International Journal of Heat and Mass Transfer **49**(23-24): pp. 4552-4557.

Medrano, M., M. O. Yilmaz, M. Nogués, I. Martorell, J. Roca and L. F. Cabeza (2009). "Experimental evaluation of commercial heat exchangers for use as PCM thermal storage systems." Applied Energy **86**(10): pp. 2047-2055.

Merlin, K., D. Delaunay, J. Soto and L. Traonvouez (2016). "Heat transfer enhancement in latent heat thermal storage systems: Comparative study of different solutions and thermal contact investigation between the exchanger and the PCM." Applied Energy **166**: pp. 107-116.

Murray, R. E. and D. Groulx (2014). "Experimental study of the phase change and energy characteristics inside a cylindrical latent heat energy storage system: Part 1 consecutive charging and discharging." Renewable Energy **62**: pp. 571-581.

Natural Resources Canada (2017) Energy Fact Book 2016-2017. 140

Paria, S., S. Baradaran, A. Amiri, A. A. D. Sarhan and S. N. Kazi (2015). "Performance evaluation of latent heat energy storage in horizontal shell-and-finned tube for solar application." Journal of Thermal Analysis and Calorimetry **123**(2): pp. 1371-1381.

Park, K. T., H. J. Kim and D.-K. Kim (2014). "Experimental study of natural convection from vertical cylinders with branched fins." Experimental Thermal and Fluid Science **54**: pp. 29-37.

Pielichowska, K. and K. Pielichowski (2014). "Phase change materials for thermal energy storage." Progress in Materials Science **65**: pp. 67-123.

Pizzolato, A., A. Sharma, K. Maute, A. Sciacovelli and V. Verda (2017). "Topology optimization for heat transfer enhancement in Latent Heat Thermal Energy Storage." International Journal of Heat and Mass Transfer **113**: pp. 875-888.

Rahimi, M., A. A. Ranjbar, D. D. Ganji, K. Sedighi, M. J. Hosseini and R. Bahrampoury (2014). "Analysis of geometrical and operational parameters of PCM in a fin and tube heat exchanger." International Communications in Heat and Mass Transfer **53**: pp. 109-115.

Rathod, M. K. and J. Banerjee (2015). "Thermal performance enhancement of shell and tube Latent Heat Storage Unit using longitudinal fins." Applied Thermal Engineering **75**: pp. 1084-1092.

Rouault, F., D. Bruneau, P. Sébastian and J. Lopez (2014). "Experimental investigation and modelling of a low temperature PCM thermal energy exchange and storage system." Energy and Buildings **83**: pp. 96-107.

Sarı, A. and K. Kaygusuz (2002). "Thermal and heat transfer characteristics in a latent heat storage system using lauric acid." Energy Conversion and Management **43**: pp. 2493-2507.

Sciacovelli, A., F. Gagliardi and V. Verda (2015). "Maximization of performance of a PCM latent heat storage system with innovative fins." Applied Energy **137**: pp. 707-715.

Sharma, A., V. V. Tyagi, C. R. Chen and D. Buddhi (2009). "Review on thermal energy storage with phase change materials and applications." Renewable & Sustainable Energy Reviews: pp. 318-345.

Sharma, R. K., P. Ganesan and V. V. Tyagi (2016). "Long-term thermal and chemical reliability study of different organic phase change materials for thermal energy storage applications." Journal of Thermal Analysis and Calorimetry **124**(3): pp. 1357-1366.

Sharma, S. D. and K. Sagara (2005). "Latent Heat Storage Materials and Systems: A Review." International Journal of Green Energy **2**(1): pp. 1-56.

Sheikholeslami, M., S. Lohrasbi and D. D. Ganji (2016). "Response surface method optimization of innovative fin structure for expediting discharging process in latent heat thermal energy storage system containing nano-enhanced phase change material." Journal of the Taiwan Institute of Chemical Engineers **67**: pp. 115-125.

Skaalum, J. and D. Groulx (2017). Experimental Investigation of Bifurcated-Fin Heat Exchanger for Latent Heat Energy Storage System. 9th World Conference on Experimental Heat Transfer, Fluid Mechanics and Thermodynamics, Iguazu Falls, Brazil. 12 p.

Sugawara, M., Y. Komatsu, Y. Takahashi and H. Beer (2011). "Freezing enhancement around a horizontal tube using copper foil disks." Heat and Mass Transfer **47**(12): pp. 1691-1698.

Tatsidjodoung, P., N. Le Pierrès and L. Luo (2013). "A review of potential materials for thermal energy storage in building applications." Renewable and Sustainable Energy Reviews **18**: pp. 327-349.

Tay, N. H. S., M. Belusko, A. Castell, L. F. Cabeza and F. Bruno (2014). "An effectiveness-NTU technique for characterising a finned tubes PCM system using a CFD model." Applied Energy **131**: pp. 377-385.

Tay, N. H. S., F. Bruno and M. Belusko (2012). "Experimental validation of a CFD model for tubes in a phase change thermal energy storage system." International Journal of Heat and Mass Transfer **55**(4): pp. 574-585.

Tay, N. H. S., F. Bruno and M. Belusko (2013). "Comparison of pinned and finned tubes in a phase change thermal energy storage system using CFD." Applied Energy **104**: pp. 79-86.

Xiao, X. and P. Zhang (2015). "Numerical and experimental study of heat transfer characteristics of a shell-tube latent heat storage system: Part I – Charging process." Energy **79**: pp. 337-350.

Yan, T., R. Z. Wang, T. X. Li, L. W. Wang and I. T. Fred (2015). "A review of promising candidate reactions for chemical heat storage." Renewable and Sustainable Energy Reviews **43**: pp. 13-31.

Yaws, C. L. (1999). Chemical Properties Handbook, McGraw-Hill**.**

Yu, B. and B. Li (2006). Fractal-like tree networks reducing the thermal conductivity. Phys Rev E Stat Nonlin Soft Matter Phys. 8 p.

Zalba, B., J. M. Marin, L. F. Cabeza and H. Mehling (2003). "Review on thermal energy storage with phase change: materials, heat transfer analysis and applications." Applied Thermal Engineering: pp. 251-283.

Ziaei, S., S. Lorente and A. Bejan (2015). Morphing tree structures for latent thermal energy storage. Journal of Applied Physics. 6 p.

Ziaei, S., S. Lorente and A. Bejan (2016). "Constructal design for convection melting of a phase change body." International Journal of Heat and Mass Transfer **99**: pp. 762-769.

Appendix A: Data Sheets

Section 2 General Information

Specifications

The Cole Parmer Polystat® Heated Immersion Circulators are used with refrigerated and heated baths. All circulators can pump to an external system. All have a digital display and easy-to-use touch pad, five programmable setpoint temperatures, acoustic and optical alarms, and offer adjustable high temperature protection.

Part Number			
115V/60Hz	12120-01 or 12120-08	12120-03 or 12120-11	12120-13
230V/50Hz	12120-02 or 12120-09	12120-04 or 12120-12	-
Process Fluid Temperature and Setpoint Range	Ambient to 100°C Ambient to 212°F	Ambient to 150°C Ambient to 302°F	Ambient to 200°C Ambient to 392°F
Temperature Stability	±0.05°C	±0.05°C	±0.025°C
Heater Capacity KWatts 230V	1.2	1.2	2.0
115V	1.0	1.0	1.2
Dimensions (H x W x D)			
mm	321.2 x 112.5 x 189.6	321.2 x 112.5 x 189.6	339.2 x 144.3 x 189.6
Inches	12.6 x 4.4 x 7.5	12.6 x 4.4 x 7.5	13.4 x 5.7 x 7.5
Net Weight kg	3.9	3.9	4.7
lb	7.4	7.4	10.1
Pump Type	Force only	Force only	Force/Suction

Pumping Capacity

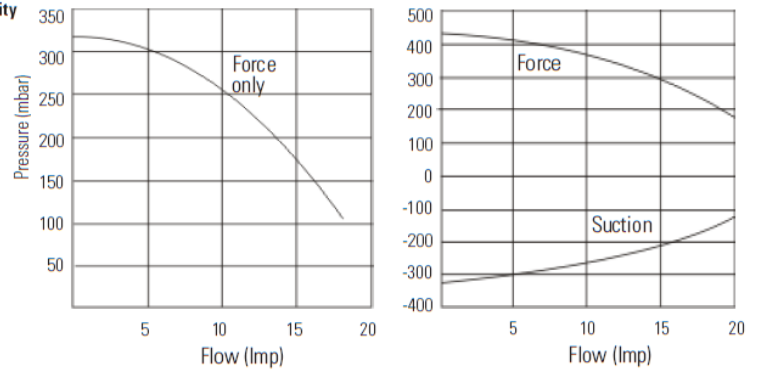

- Lower process fluid temperature ranges available with supplemental cooling.
- Pumping curves obtained using water at ambient temperature, nominal voltage operating in high speed mode. Other conditions will affect performance.
- Cole Parmer reserves the right to change specifications without notice.

Stainless Steel Refrigerated/Heated Bath Circulator Specifications

Part Number* 115V/60Hz 230V/50Hz	**12122-02** **12122-04**	**12122-16** **12122-18**	**12122-32** **21233-34**	**12122-46** **12122-48**
Temperature Range	-20 to 100°C -4 to 212°F	-20 to 100°C -4 to 212°F	-28 to 100°C -18 to 212°F	-35 to 100°C -31 to 212°F
Bath Volume liters gallons	3 - 6 0.8 - 1.6	3 - 6 0.8 - 1.6	8 - 15 2.1 - 4.0	8 - 15 2.1 - 4.0
Cooling Capacity watts @20°C	250	250	500	800
Refrigerant	R134a	R134a	R134a	R404a
Dimensions (H x W x D)** mm inches	617.2 x 205.0 x 414.0 24.3 x 8.1 x 16.3	425.5 x 467.4 x 416.6 16.8 x 18.4 x 16.4	647.9 x 258.0 x 483.0 25.5 x 10.2 x 19.0	686.9 x 370.0 x 520.7 27.0 x 14.6 x 20.5
Net Weight kg lb	23.9 52.7	26.7 58.9	33.3 73.4	52.6 115.9

Part Number* 115V/60Hz 230V/50Hz	**12122-36** **12122-38**	**12122-52** **12122-54**
Temperature Range	-28 to 150°C -18 to 302°F	-35 to 150°C -31 to 302°F
Bath Volume liters gallons	8 - 15 2.1 - 4.0	8 - 15 2.1 - 4.0
Cooling Capacity watts @20°C	500	800
Refrigerant	R134a	R404a
Dimensions (H x W x D)** mm inches	647.9 x 258.0 x 483.0 25.5 x 10.2 x 19.0	686.9 x 370.0 x 519.0 27.0 x 14.6 x 20.4
Net Weight kg lb	33.3 73.4	52.6 115.9

Part Number* 115V/60Hz 230V/50Hz	**12122-12** **12122-14**	**12122-26** **12122-28**	**12122-42** **12122-44**	**12122-56** **12122-58**
Temperature Range	-20 to 100°C -4 to 212°F	-20 to 100°C -4 to 212°F	-28 to 200°C -18 to 392°F	-35 to 200°C -31 to 392°F
Bath Volume liters gallons	3 - 6 0.8 - 1.6	3 - 6 0.8 - 1.6	8 - 15 2.1 - 4.0	8 - 15 2.1 - 4.0
Cooling Capacity watts @20°C	250	250	500	800
Refrigerant	R134a	R134a	R134a	R404a
Dimensions (H x W x D)** mm inches	635.0 x 205.0 x 414.0 25.0 x 8.1 x 16.3	443.0 x 467.4 x 416.6 17.4 x 18.4 x 16.4	665.4 x 258.0 x 483.0 26.2 x 10.2 x 19.0	706.1 x 370.0 x 520.7 27.8 x 14.6 x 20.5
Net Weight kg lb	24.7 53.5	27.1 59.7	33.7 74.2	52.9 116.7

*Refer to serial tag on the back of the bath for part number.

**Add ~15 mm to D for drain fitting

Flow Curves for Magnetic Drive Pumps with Enclosed Motors

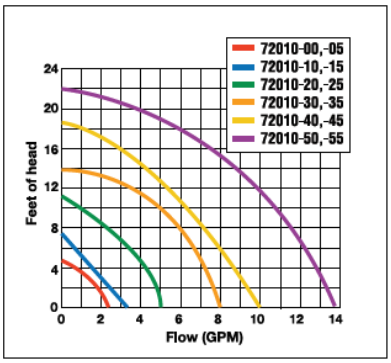

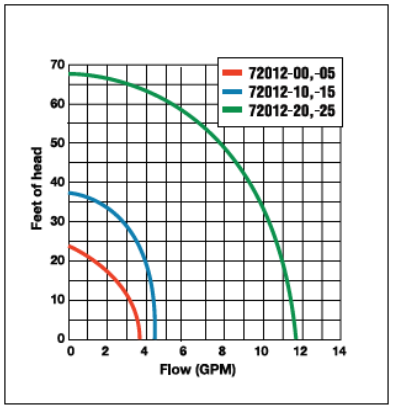

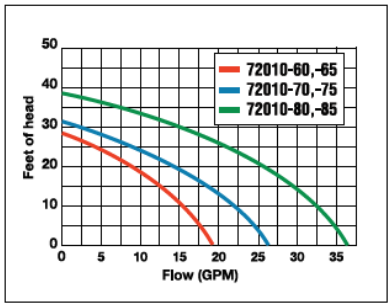

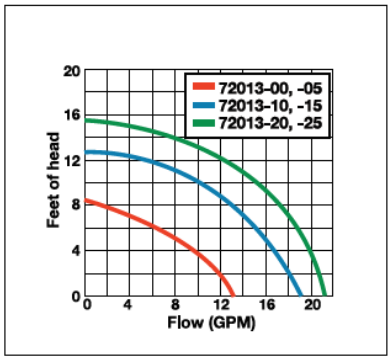

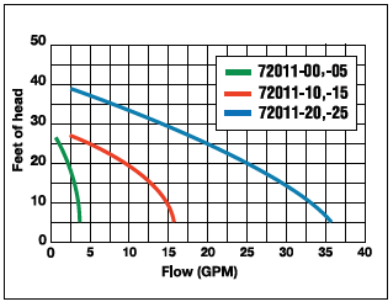

Revised Thermocouple Reference Tables

TYPE T

Reference Tables
N.I.S.T.
Monograph 175
Revised to
ITS-90

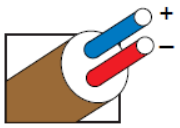

Thermocouple Grade

Copper vs. Copper-Nickel

Extension Grade

MAXIMUM TEMPERATURE RANGE
Thermocouple Grade
– 328 to 662°F
– 200 to 350°C
Extension Grade
– 76 to 212°F
– 60 to 100°C
LIMITS OF ERROR
(whichever is greater)
Standard: 1.0°C or 0.75% Above 0°C
1.0°C or 1.5% Below 0°C
Special: 0.5°C or 0.4%
COMMENTS, BARE WIRE ENVIRONMENT:
Mild Oxidizing, Reducing Vacuum or Inert; Good Where Moisture Is Present; Low Temperature and Cryogenic Applications
TEMPERATURE IN DEGREES °C
REFERENCE JUNCTION AT 0°C

Thermoelectric Voltage in Millivolts

°C	-10	-9	-8	-7	-6	-5	-4	-3	-2	-1	0	°C
-260	-6.258	-6.256	-6.255	-6.253	-6.251	-6.248	-6.245	-6.242	-6.239	-6.236	-6.232	-260
-250	-6.232	-6.228	-6.223	-6.219	-6.214	-6.209	-6.204	-6.198	-6.193	-6.187	-6.180	-250
-240	-6.180	-6.174	-6.167	-6.160	-6.153	-6.146	-6.138	-6.130	-6.122	-6.114	-6.105	-240
-230	-6.105	-6.096	-6.087	-6.078	-6.068	-6.059	-6.049	-6.038	-6.028	-6.017	-6.007	-230
-220	-6.007	-5.996	-5.985	-5.973	-5.962	-5.950	-5.938	-5.926	-5.914	-5.901	-5.888	-220
-210	-5.888	-5.876	-5.863	-5.850	-5.836	-5.823	-5.809	-5.795	-5.782	-5.767	-5.753	-210
-200	-5.753	-5.739	-5.724	-5.710	-5.695	-5.680	-5.665	-5.650	-5.634	-5.619	-5.603	-200
-190	-5.603	-5.587	-5.571	-5.555	-5.539	-5.523	-5.506	-5.489	-5.473	-5.456	-5.439	-190
-180	-5.439	-5.421	-5.404	-5.387	-5.369	-5.351	-5.334	-5.316	-5.297	-5.279	-5.261	-180
-170	-5.261	-5.242	-5.224	-5.205	-5.186	-5.167	-5.148	-5.128	-5.109	-5.089	-5.070	-170
-160	-5.070	-5.050	-5.030	-5.010	-4.989	-4.969	-4.949	-4.928	-4.907	-4.886	-4.865	-160
-150	-4.865	-4.844	-4.823	-4.802	-4.780	-4.759	-4.737	-4.715	-4.693	-4.671	-4.648	-150
-140	-4.648	-4.626	-4.604	-4.581	-4.558	-4.535	-4.512	-4.489	-4.466	-4.443	-4.419	-140
-130	-4.419	-4.395	-4.372	-4.348	-4.324	-4.300	-4.275	-4.251	-4.226	-4.202	-4.177	-130
-120	-4.177	-4.152	-4.127	-4.102	-4.077	-4.052	-4.026	-4.000	-3.975	-3.949	-3.923	-120
-110	-3.923	-3.897	-3.871	-3.844	-3.818	-3.791	-3.765	-3.738	-3.711	-3.684	-3.657	-110
-100	-3.657	-3.629	-3.602	-3.574	-3.547	-3.519	-3.491	-3.463	-3.435	-3.407	-3.379	-100
-90	-3.379	-3.350	-3.322	-3.293	-3.264	-3.235	-3.206	-3.177	-3.148	-3.118	-3.089	-90
-80	-3.089	-3.059	-3.030	-3.000	-2.970	-2.940	-2.910	-2.879	-2.849	-2.818	-2.788	-80
-70	-2.788	-2.757	-2.726	-2.695	-2.664	-2.633	-2.602	-2.571	-2.539	-2.507	-2.476	-70
-60	-2.476	-2.444	-2.412	-2.380	-2.348	-2.316	-2.283	-2.251	-2.218	-2.186	-2.153	-60
-50	-2.153	-2.120	-2.087	-2.054	-2.021	-1.987	-1.954	-1.920	-1.887	-1.853	-1.819	-50
-40	-1.819	-1.785	-1.751	-1.717	-1.683	-1.648	-1.614	-1.579	-1.545	-1.510	-1.475	-40
-30	-1.475	-1.440	-1.405	-1.370	-1.335	-1.299	-1.264	-1.228	-1.192	-1.157	-1.121	-30
-20	-1.121	-1.085	-1.049	-1.013	-0.976	-0.940	-0.904	-0.867	-0.830	-0.794	-0.757	-20
-10	-0.757	-0.720	-0.683	-0.646	-0.608	-0.571	-0.534	-0.496	-0.459	-0.421	-0.383	-10
0	-0.383	-0.345	-0.307	-0.269	-0.231	-0.193	-0.154	-0.116	-0.077	-0.039	0.000	0
0	0.000	0.039	0.078	0.117	0.156	0.195	0.234	0.273	0.312	0.352	0.391	0
10	0.391	0.431	0.470	0.510	0.549	0.589	0.629	0.669	0.709	0.749	0.790	10
20	0.790	0.830	0.870	0.911	0.951	0.992	1.033	1.074	1.114	1.155	1.196	20
30	1.196	1.238	1.279	1.320	1.362	1.403	1.445	1.486	1.528	1.570	1.612	30
40	1.612	1.654	1.696	1.738	1.780	1.823	1.865	1.908	1.950	1.993	2.036	40
°C	0	1	2	3	4	5	6	7	8	9	10	°C

°C	0	1	2	3	4	5	6	7	8	9	10	°C
50	2.036	2.079	2.122	2.165	2.208	2.251	2.294	2.338	2.381	2.425	2.468	50
60	2.468	2.512	2.556	2.600	2.643	2.687	2.732	2.776	2.820	2.864	2.909	60
70	2.909	2.953	2.998	3.043	3.087	3.132	3.177	3.222	3.267	3.312	3.358	70
80	3.358	3.403	3.448	3.494	3.539	3.585	3.631	3.677	3.722	3.768	3.814	80
90	3.814	3.860	3.907	3.953	3.999	4.046	4.092	4.138	4.185	4.232	4.279	90
100	4.279	4.325	4.372	4.419	4.466	4.513	4.561	4.608	4.655	4.702	4.750	100
110	4.750	4.798	4.845	4.893	4.941	4.988	5.036	5.084	5.132	5.180	5.228	110
120	5.228	5.277	5.325	5.373	5.422	5.470	5.519	5.567	5.616	5.665	5.714	120
130	5.714	5.763	5.812	5.861	5.910	5.959	6.008	6.057	6.107	6.156	6.206	130
140	6.206	6.255	6.305	6.355	6.404	6.454	6.504	6.554	6.604	6.654	6.704	140
150	6.704	6.754	6.805	6.855	6.905	6.956	7.006	7.057	7.107	7.158	7.209	150
160	7.209	7.260	7.310	7.361	7.412	7.463	7.515	7.566	7.617	7.668	7.720	160
170	7.720	7.771	7.823	7.874	7.926	7.977	8.029	8.081	8.133	8.185	8.237	170
180	8.237	8.289	8.341	8.393	8.445	8.497	8.550	8.602	8.654	8.707	8.759	180
190	8.759	8.812	8.865	8.917	8.970	9.023	9.076	9.129	9.182	9.235	9.288	190
200	9.288	9.341	9.395	9.448	9.501	9.555	9.608	9.662	9.715	9.769	9.822	200
210	9.822	9.876	9.930	9.984	10.038	10.092	10.146	10.200	10.254	10.308	10.362	210
220	10.362	10.417	10.471	10.525	10.580	10.634	10.689	10.743	10.798	10.853	10.907	220
230	10.907	10.962	11.017	11.072	11.127	11.182	11.237	11.292	11.347	11.403	11.458	230
240	11.458	11.513	11.569	11.624	11.680	11.735	11.791	11.846	11.902	11.958	12.013	240
250	12.013	12.069	12.125	12.181	12.237	12.293	12.349	12.405	12.461	12.518	12.574	250
260	12.574	12.630	12.687	12.743	12.799	12.856	12.912	12.969	13.026	13.082	13.139	260
270	13.139	13.196	13.253	13.310	13.366	13.423	13.480	13.537	13.595	13.652	13.709	270
280	13.709	13.766	13.823	13.881	13.938	13.995	14.053	14.110	14.168	14.226	14.283	280
290	14.283	14.341	14.399	14.456	14.514	14.572	14.630	14.688	14.746	14.804	14.862	290
300	14.862	14.920	14.978	15.036	15.095	15.153	15.211	15.270	15.328	15.386	15.445	300
310	15.445	15.503	15.562	15.621	15.679	15.738	15.797	15.856	15.914	15.973	16.032	310
320	16.032	16.091	16.150	16.209	16.268	16.327	16.387	16.446	16.505	16.564	16.624	320
330	16.624	16.683	16.742	16.802	16.861	16.921	16.980	17.040	17.100	17.159	17.219	330
340	17.219	17.279	17.339	17.399	17.458	17.518	17.578	17.638	17.698	17.759	17.819	340
350	17.819	17.879	17.939	17.999	18.060	18.120	18.180	18.241	18.301	18.362	18.422	350
360	18.422	18.483	18.543	18.604	18.665	18.725	18.786	18.847	18.908	18.969	19.030	360
370	19.030	19.091	19.152	19.213	19.274	19.335	19.396	19.457	19.518	19.579	19.641	370
380	19.641	19.702	19.763	19.825	19.886	19.947	20.009	20.070	20.132	20.193	20.255	380
390	20.255	20.317	20.378	20.440	20.502	20.563	20.625	20.687	20.748	20.810	20.872	390
°C	0	1	2	3	4	5	6	7	8	9	10	°C

MAXIMUM TEMPERATURE RANGE
Thermocouple Grade
– 328 to 2282°F
– 200 to 1250°C
Extension Grade
32 to 392°F
0 to 200°C
LIMITS OF ERROR
(whichever is greater)
Standard: 2.2°C or 0.75% Above 0°C
2.2°C or 2.0% Below 0°C
Special: 1.1°C or 0.4%
COMMENTS, BARE WIRE ENVIRONMENT:
Clean Oxidizing and Inert; Limited Use in Vacuum or Reducing; Wide Temperature Range; Most Popular Calibration
TEMPERATURE IN DEGREES °C
REFERENCE JUNCTION AT 0°C

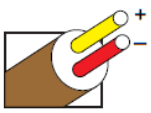

Thermocouple Grade

Nickel-Chromium vs. Nickel-Aluminum

Extension Grade

Revised Thermocouple Reference Tables

TYPE K

Reference Tables
N.I.S.T. Monograph 175
Revised to ITS-90

Z

Thermoelectric Voltage in Millivolts

°C	-10	-9	-8	-7	-6	-5	-4	-3	-2	-1	0	°C
-260	-6.458	-6.457	-6.456	-6.455	-6.453	-6.452	-6.450	-6.448	-6.446	-6.444	-6.441	-260
-250	-6.441	-6.438	-6.435	-6.432	-6.429	-6.425	-6.421	-6.417	-6.413	-6.408	-6.404	-250
-240	-6.404	-6.399	-6.393	-6.388	-6.382	-6.377	-6.370	-6.364	-6.358	-6.351	-6.344	-240
-230	-6.344	-6.337	-6.329	-6.322	-6.314	-6.306	-6.297	-6.289	-6.280	-6.271	-6.262	-230
-220	-6.262	-6.252	-6.243	-6.233	-6.223	-6.213	-6.202	-6.192	-6.181	-6.170	-6.158	-220
-210	-6.158	-6.147	-6.135	-6.123	-6.111	-6.099	-6.087	-6.074	-6.061	-6.048	-6.035	-210
-200	-6.035	-6.021	-6.007	-5.994	-5.980	-5.965	-5.951	-5.936	-5.922	-5.907	-5.891	-200
-190	-5.891	-5.876	-5.861	-5.845	-5.829	-5.813	-5.797	-5.780	-5.763	-5.747	-5.730	-190
-180	-5.730	-5.713	-5.695	-5.678	-5.660	-5.642	-5.624	-5.606	-5.588	-5.569	-5.550	-180
-170	-5.550	-5.531	-5.512	-5.493	-5.474	-5.454	-5.435	-5.415	-5.395	-5.374	-5.354	-170
-160	-5.354	-5.333	-5.313	-5.292	-5.271	-5.250	-5.228	-5.207	-5.185	-5.163	-5.141	-160
-150	-5.141	-5.119	-5.097	-5.074	-5.052	-5.029	-5.006	-4.983	-4.960	-4.936	-4.913	-150
-140	-4.913	-4.889	-4.865	-4.841	-4.817	-4.793	-4.768	-4.744	-4.719	-4.694	-4.669	-140
-130	-4.669	-4.644	-4.618	-4.593	-4.567	-4.542	-4.516	-4.490	-4.463	-4.437	-4.411	-130
-120	-4.411	-4.384	-4.357	-4.330	-4.303	-4.276	-4.249	-4.221	-4.194	-4.166	-4.138	-120
-110	-4.138	-4.110	-4.082	-4.054	-4.025	-3.997	-3.968	-3.939	-3.911	-3.882	-3.852	-110
-100	-3.852	-3.823	-3.794	-3.764	-3.734	-3.705	-3.675	-3.645	-3.614	-3.584	-3.554	-100
-90	-3.554	-3.523	-3.492	-3.462	-3.431	-3.400	-3.368	-3.337	-3.306	-3.274	-3.243	-90
-80	-3.243	-3.211	-3.179	-3.147	-3.115	-3.083	-3.050	-3.018	-2.986	-2.953	-2.920	-80
-70	-2.920	-2.887	-2.854	-2.821	-2.788	-2.755	-2.721	-2.688	-2.654	-2.620	-2.587	-70
-60	-2.587	-2.553	-2.519	-2.485	-2.450	-2.416	-2.382	-2.347	-2.312	-2.278	-2.243	-60
-50	-2.243	-2.208	-2.173	-2.138	-2.103	-2.067	-2.032	-1.996	-1.961	-1.925	-1.889	-50
-40	-1.889	-1.854	-1.818	-1.782	-1.745	-1.709	-1.673	-1.637	-1.600	-1.564	-1.527	-40
-30	-1.527	-1.490	-1.453	-1.417	-1.380	-1.343	-1.305	-1.268	-1.231	-1.194	-1.156	-30
-20	-1.156	-1.119	-1.081	-1.043	-1.006	-0.968	-0.930	-0.892	-0.854	-0.816	-0.778	-20
-10	-0.778	-0.739	-0.701	-0.663	-0.624	-0.586	-0.547	-0.508	-0.470	-0.431	-0.392	-10
0	-0.392	-0.353	-0.314	-0.275	-0.236	-0.197	-0.157	-0.118	-0.079	-0.039	0.000	0
0	0.000	0.039	0.079	0.119	0.158	0.198	0.238	0.277	0.317	0.357	0.397	0
10	0.397	0.437	0.477	0.517	0.557	0.597	0.637	0.677	0.718	0.758	0.798	10
20	0.798	0.838	0.879	0.919	0.960	1.000	1.041	1.081	1.122	1.163	1.203	20
30	1.203	1.244	1.285	1.326	1.366	1.407	1.448	1.489	1.530	1.571	1.612	30
40	1.612	1.653	1.694	1.735	1.776	1.817	1.858	1.899	1.941	1.982	2.023	40
50	2.023	2.064	2.106	2.147	2.188	2.230	2.271	2.312	2.354	2.395	2.436	50
60	2.436	2.478	2.519	2.561	2.602	2.644	2.685	2.727	2.768	2.810	2.851	60
70	2.851	2.893	2.934	2.976	3.017	3.059	3.100	3.142	3.184	3.225	3.267	70
80	3.267	3.308	3.350	3.391	3.433	3.474	3.516	3.557	3.599	3.640	3.682	80
90	3.682	3.723	3.765	3.806	3.848	3.889	3.931	3.972	4.013	4.055	4.096	90
100	4.096	4.138	4.179	4.220	4.262	4.303	4.344	4.385	4.427	4.468	4.509	100
110	4.509	4.550	4.591	4.633	4.674	4.715	4.756	4.797	4.838	4.879	4.920	110
120	4.920	4.961	5.002	5.043	5.084	5.124	5.165	5.206	5.247	5.288	5.328	120
130	5.328	5.369	5.410	5.450	5.491	5.532	5.572	5.613	5.653	5.694	5.735	130
140	5.735	5.775	5.815	5.856	5.896	5.937	5.977	6.017	6.058	6.098	6.138	140
150	6.138	6.179	6.219	6.259	6.299	6.339	6.380	6.420	6.460	6.500	6.540	150
160	6.540	6.580	6.620	6.660	6.701	6.741	6.781	6.821	6.861	6.901	6.941	160
170	6.941	6.981	7.021	7.060	7.100	7.140	7.180	7.220	7.260	7.300	7.340	170
180	7.340	7.380	7.420	7.460	7.500	7.540	7.579	7.619	7.659	7.699	7.739	180
190	7.739	7.779	7.819	7.859	7.899	7.939	7.979	8.019	8.059	8.099	8.138	190
200	8.138	8.178	8.218	8.258	8.298	8.338	8.378	8.418	8.458	8.499	8.539	200
210	8.539	8.579	8.619	8.659	8.699	8.739	8.779	8.819	8.860	8.900	8.940	210
220	8.940	8.980	9.020	9.061	9.101	9.141	9.181	9.222	9.262	9.302	9.343	220
230	9.343	9.383	9.423	9.464	9.504	9.545	9.585	9.626	9.666	9.707	9.747	230
240	9.747	9.788	9.828	9.869	9.909	9.950	9.991	10.031	10.072	10.113	10.153	240
°C	0	1	2	3	4	5	6	7	8	9	10	°C

°C	0	1	2	3	4	5	6	7	8	9	10	°C
250	10.153	10.194	10.235	10.276	10.316	10.357	10.398	10.439	10.480	10.520	10.561	250
260	10.561	10.602	10.643	10.684	10.725	10.766	10.807	10.848	10.889	10.930	10.971	260
270	10.971	11.012	11.053	11.094	11.135	11.176	11.217	11.259	11.300	11.341	11.382	270
280	11.382	11.423	11.465	11.506	11.547	11.588	11.630	11.671	11.712	11.753	11.795	280
290	11.795	11.836	11.877	11.919	11.960	12.001	12.043	12.084	12.126	12.167	12.209	290
300	12.209	12.250	12.291	12.333	12.374	12.416	12.457	12.499	12.540	12.582	12.624	300
310	12.624	12.665	12.707	12.748	12.790	12.831	12.873	12.915	12.956	12.998	13.040	310
320	13.040	13.081	13.123	13.165	13.206	13.248	13.290	13.331	13.373	13.415	13.457	320
330	13.457	13.498	13.540	13.582	13.624	13.665	13.707	13.749	13.791	13.833	13.874	330
340	13.874	13.916	13.958	14.000	14.042	14.084	14.126	14.167	14.209	14.251	14.293	340
350	14.293	14.335	14.377	14.419	14.461	14.503	14.545	14.587	14.629	14.671	14.713	350
360	14.713	14.755	14.797	14.839	14.881	14.923	14.965	15.007	15.049	15.091	15.133	360
370	15.133	15.175	15.217	15.259	15.301	15.343	15.385	15.427	15.469	15.511	15.554	370
380	15.554	15.596	15.638	15.680	15.722	15.764	15.806	15.849	15.891	15.933	15.975	380
390	15.975	16.017	16.059	16.102	16.144	16.186	16.228	16.270	16.313	16.355	16.397	390
400	16.397	16.439	16.482	16.524	16.566	16.608	16.651	16.693	16.735	16.778	16.820	400
410	16.820	16.862	16.904	16.947	16.989	17.031	17.074	17.116	17.158	17.201	17.243	410
420	17.243	17.285	17.328	17.370	17.413	17.455	17.497	17.540	17.582	17.624	17.667	420
430	17.667	17.709	17.752	17.794	17.837	17.879	17.921	17.964	18.006	18.049	18.091	430
440	18.091	18.134	18.176	18.218	18.261	18.303	18.346	18.388	18.431	18.473	18.516	440
450	18.516	18.558	18.601	18.643	18.686	18.728	18.771	18.813	18.856	18.898	18.941	450
460	18.941	18.983	19.026	19.068	19.111	19.154	19.196	19.239	19.281	19.324	19.366	460
470	19.366	19.409	19.451	19.494	19.537	19.579	19.622	19.664	19.707	19.750	19.792	470
480	19.792	19.835	19.877	19.920	19.962	20.005	20.048	20.090	20.133	20.175	20.218	480
490	20.218	20.261	20.303	20.346	20.389	20.431	20.474	20.516	20.559	20.602	20.644	490
500	20.644	20.687	20.730	20.772	20.815	20.857	20.900	20.943	20.985	21.028	21.071	500
510	21.071	21.113	21.156	21.199	21.241	21.284	21.326	21.369	21.412	21.454	21.497	510
520	21.497	21.540	21.582	21.625	21.668	21.710	21.753	21.796	21.838	21.881	21.924	520
530	21.924	21.966	22.009	22.052	22.094	22.137	22.179	22.222	22.265	22.307	22.350	530
540	22.350	22.393	22.435	22.478	22.521	22.563	22.606	22.649	22.691	22.734	22.776	540
550	22.776	22.819	22.862	22.904	22.947	22.990	23.032	23.075	23.117	23.160	23.203	550
560	23.203	23.245	23.288	23.331	23.373	23.416	23.458	23.501	23.544	23.586	23.629	560
570	23.629	23.671	23.714	23.757	23.799	23.842	23.884	23.927	23.970	24.012	24.055	570
580	24.055	24.097	24.140	24.182	24.225	24.267	24.310	24.353	24.395	24.438	24.480	580
590	24.480	24.523	24.565	24.608	24.650	24.693	24.735	24.778	24.820	24.863	24.905	590
600	24.905	24.948	24.990	25.033	25.075	25.118	25.160	25.203	25.245	25.288	25.330	600
610	25.330	25.373	25.415	25.458	25.500	25.543	25.585	25.627	25.670	25.712	25.755	610
620	25.755	25.797	25.840	25.882	25.924	25.967	26.009	26.052	26.094	26.136	26.179	620
630	26.179	26.221	26.263	26.306	26.348	26.390	26.433	26.475	26.517	26.560	26.602	630
640	26.602	26.644	26.687	26.729	26.771	26.814	26.856	26.898	26.940	26.983	27.025	640
650	27.025	27.067	27.109	27.152	27.194	27.236	27.278	27.320	27.363	27.405	27.447	650
660	27.447	27.489	27.531	27.574	27.616	27.658	27.700	27.742	27.784	27.826	27.869	660
670	27.869	27.911	27.953	27.995	28.037	28.079	28.121	28.163	28.205	28.247	28.289	670
680	28.289	28.332	28.374	28.416	28.458	28.500	28.542	28.584	28.626	28.668	28.710	680
690	28.710	28.752	28.794	28.835	28.877	28.919	28.961	29.003	29.045	29.087	29.129	690
700	29.129	29.171	29.213	29.255	29.297	29.338	29.380	29.422	29.464	29.506	29.548	700
710	29.548	29.589	29.631	29.673	29.715	29.757	29.798	29.840	29.882	29.924	29.965	710
720	29.965	30.007	30.049	30.090	30.132	30.174	30.216	30.257	30.299	30.341	30.382	720
730	30.382	30.424	30.466	30.507	30.549	30.590	30.632	30.674	30.715	30.757	30.798	730
740	30.798	30.840	30.881	30.923	30.964	31.006	31.047	31.089	31.130	31.172	31.213	740
750	31.213	31.255	31.296	31.338	31.379	31.421	31.462	31.504	31.545	31.586	31.628	750
760	31.628	31.669	31.710	31.752	31.793	31.834	31.876	31.917	31.958	32.000	32.041	760
770	32.041	32.082	32.124	32.165	32.206	32.247	32.289	32.330	32.371	32.412	32.453	770
780	32.453	32.495	32.536	32.577	32.618	32.659	32.700	32.742	32.783	32.824	32.865	780
790	32.865	32.906	32.947	32.988	33.029	33.070	33.111	33.152	33.193	33.234	33.275	790
°C	0	1	2	3	4	5	6	7	8	9	10	°C

Model No.	Min.	FlowRate GPM Cont.	Max	Connections MNPT	Length (in.)	Height (in.)	Width (in.)	Pressure Loss (psi)	Weight (lb)	Max. Temp.
FTB-4005	0.15	6.6	13.2	1/2"C	4.33	2.50	2.75	3.60	1.10	122˚F
FTB-4007	0.20	11.0	20.0	3/4'C	5.10	2.50	2.75	3.60	1.40	122˚F
FTB-4105	0.15	6.6	13.2	1/2"C	4.33	2.50	2.75	3.60	1.10	200˚F
FTB-4105P+	0.15	6.6	13.2	1/2"C	4.33	*	2.75	3.60	1.10	200˚F
FTB-4107	0.20	11.0	20.0	3/4"C	5.10	2.50	2.75	3.60	1.40	200˚F
FTB-4107P+	0.20	11.0	20.0	3/4"C	5.10	*	2.75	3.60	1.40	200˚F
FTB-4110	0.50	26.4	52.8	1"C	10.25	4.75	4.00	2.00	5.50	200˚F
FTB-4110P+	0.50	26.4	52.8	1"C	10.25	4.75	4.00	2.00	5.50	200˚F
FTB-4112	0.50	26.4	52.8	1.25"C	10.25	4.75	4.00	2.00	5.50	200˚F
FTB-4112P+	0.50	26.4	52.8	1.25"C	10.25	4.75	4.00	2.00	5.50	200˚F
FTB-4115	0.80	44.0	88.0	1.5C	11.80	5.50	5.25	2.00	12.00	200˚F
FTB-4115P+	0.80	44.0	88.0	1.5C	11.80	5.50	5.25	2.00	12.00	200˚F
FTB-4605	0.15	6.6	13.0	1/2"C	4.33	2.00	2.75	3.60	1.20	190˚F
FTB-4607	0.22	11.0	20.0	3/4"C	5.10	2.00	2.75	3.60	1.30	190˚F
FTB-5000	0.13	6.6	13.2	1/2"C	4.33	4.50	3.25	2.90	2.20	248˚F
FTB-5005	0.22	11.0	22.0	3/4"C	5.10	4.75	3.25	2.90	2.40	248˚F
FTB-5010X	0.40	26.4	52.8	1"C	10.25	7.25	4.00	2.90	6.40	248˚F
FTB-5015	0.70	43.9	87.2	1.5"C	11.80	8.10	5.25	3.60	11.25	248˚F
FTB-5020	0.88	65.8	131.6	2FL	10.63	8.95	FL	2.90	27.50	248˚F
FTB-5020X	2.63	65.8	307.0	2FL	7.90	10.90	FL	0.15	31.50	248˚F
FTB-5030	3.51	175.4	658.0	3FL	8.90	11.50	FL	0.30	40.10	248˚F
FTB-5040	5.26	263.2	790.0	4FL	9.85	12.20	FL	0.40	43.70	248˚F
FTB-5060	26.32	657.9	1535.0	6FL	11.80	14.10	FL	0.30	71.60	248˚F
FTB-5080	43.86	1096.5	2631.0	8FL	13.75	15.30	FL	0.20	99.20	248˚F

P+ = Pulse Output Models
C = Union Coupling connections with NPT threads
FL = Flanged interconnection (conforms to ANSI B 16.5-150 lbs.)
* Height increases by approximately 2 inches with pulse output
Optional reed relay for remote totalization-order model FTB-RR

SPECIFICATIONS (CONT'D)

ACCURACY:

4600 Series:	From 10% of cont. to max. flow:	± 1.5% of reading
	Below 10% of cont. flow:	± 2% of reading
4000, 5000 Series:	From 20% of cont. to max. flow:	± 1% of reading
	Below 20% of cont. flow:	± 3% of reading

MAX. TEMPERATURE:

4000 Series:	122°F (50°C)
4100 Series:	190°F (87.7°C)
4600 Series:	190°F (87.7°C)
5000 Series:	248°F (120°C)

MAX. PRESSURE:

4000, 4600 Series:	150 PSI
5000 Series:	250 PSI

PULSE OUTPUTS: Reed relay

4100P Series:	1 gal./pulse
5010 - 5020:	1 or 10 gal./pulse
5020X - 5040:	10 gal./pulse
5060 & 5080:	100 gal./pulse

FTB4600 HIGH RESOLUTION PULSE OUTPUT:

FTB4605:	151.4 pulses/gal.
FTB4607:	75.7 pulses/gal. Requires 6-16 VDC @ 10mA max power; output requires pull-up to positive DC voltage.

(OPTICAL PICKUP (= MIN. INCREMENT):

5010 -5020X:	0.5 gal./pulse
5030 & 5040:	1 gal./pulse
5060 & 5080:	5 gal./pulse

MAX. READING (GAL.):

4000 Series:	100,000,000
5010 - 5040:	10,000,000
5060 - 5080:	100,000,000

HOUSING:

4000, 4100, 5005 - 5015:	Cast brass
5020 - 5080:	Cast iron
4600 Series:	Brass

BEARING: Ceramic/sapphire

TURBINE: High temperature thermoplastic/fiberglass (polyimide)

FLOW TRANSFER: Ceramic magnet

OTHER WETTED PARTS: Stainless steel, polypropylene, EPDM O-ring

WIRING DIAGRAM (FTB4605/FTB4607 ONLY)

NOTE

The wiring scheme illustrated below may be of two versions
Follow the appropriate wiring scheme.

LEAD	KEY	COLOR SCHEME
6-16VDC	A	BROWN
PULSE SIGNAL HI	B	GREEN
POWER GROUND PULSE LO	C	WHITE

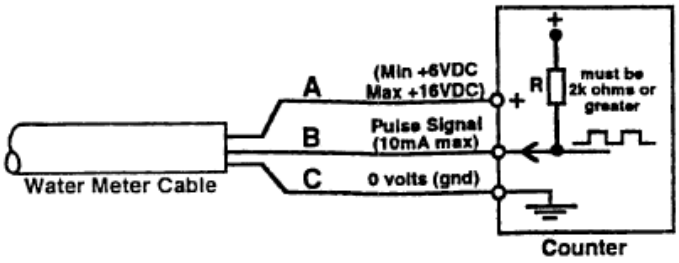

NI 9213 Specifications

The following specifications are typical for the range -40 °C to 70 °C unless otherwise noted.

Caution Do not operate the NI 9213 in a manner not specified in this document. Product misuse can result in a hazard. You can compromise the safety protection built into the product if the product is damaged in any way. If the product is damaged, return it to NI for repair.

Warm-up time	15 minutes

Input Characteristics

Number of channels	16 thermocouple channels, 1 internal autozero channel, 1 internal cold-junction compensation channel
ADC resolution	24 bits
Type of ADC	Delta-Sigma
Sampling mode	Scanned
Voltage measurement range	±78.125 mV
Temperature measurement ranges	Works over temperature ranges defined by NIST (J, K, T, E, N, B, R, S thermocouple types)

Table 1. Timing Modes

Timing Mode	Conversion Time (Per Channel)	Sample Rate[1] (All Channels[2])
High-resolution	55 ms	1 S/s
High-speed	740 µs	75 S/s

Common-mode voltage range	
Channel-to-COM	±1.2 V minimum
COM-to-earth ground	±250 V

[1] If you are using fewer than all channels, the sample rate might be faster. The maximum sample rate = 1/(*Conversion Time* x *Number of Channels*), or 100 S/s, whichever is smaller. Sampling faster than the maximum sample rate may result in the degradation of accuracy.

[2] Including the autozero and cold-junction channels.

Common-mode rejection ratio	
High-resolution mode (at DC and 50 Hz to 60 Hz)	
Channel-to-COM	100 dB
COM-to-earth ground	>170 dB
High-speed mode (at 0 Hz to 60 Hz)	
Channel-to-COM	70 dB
COM-to-earth ground	>150 dB
Input bandwidth	
High-resolution mode	14.4 Hz
High-speed mode	78 Hz
High-resolution noise rejection (at 50 Hz and 60 Hz)	60 dB
Overvoltage protection	±30 V between any two inputs
Differential input impedance	78 MΩ
Input current	50 nA
Input noise	
High-resolution mode	200 nVrms
High-speed mode	7 µVrms
Gain error	
High-resolution mode	
at 25 °C	0.03% typical
at -40 °C to 70 °C	0.07% typical, 0.15% maximum
High-speed mode	
at 25 °C	0.04% typical
at -40 °C to 70 °C	0.08% typical, 0.16% maximum
Offset error	
High-resolution mode	4 µV typical, 6 µV maximum
High-speed mode	14 µV typical, 17 µV maximum
Offset error from source impedance	Add 0.05 µV per Ω, when source impedance >50 Ω

Cold-junction compensation accuracy	
0 °C to 70 °C	0.8 °C typical, 1.7 °C maximum
-40 °C to 70 °C	1.1 °C typical, 2.1 °C maximum
MTBF	852,407 hours at 25 °C; Bellcore Issue 2, Method 1,Case 3, Limited Part Stress Method

Temperature Measurement Accuracy

Measurement sensitivity[3]	
High-resolution mode	
Types J, K, T, E, N	<0.02 °C
Types B, R, S	<0.15 °C
High-speed mode	
Types J, K, T, E	<0.25 °C
Type N	<0.35 °C
Type B	<1.2 °C
Types R, S	<2.8 °C

The following figures show the errors for each thermocouple type when connected to the NI 9213 with the autozero channel on. The figures display the maximum errors over a full temperature range and typical errors at room temperature. The figures account for gain errors, offset errors, differential and integral nonlinearity, quantization errors, noise errors, 50 Ω lead wire resistance, and cold-junction compensation errors. The figures do not account for the accuracy of the thermocouple itself.

[3] Measurement sensitivity represents the smallest change in a temperature that a sensor can detect. It is a function of noise. The values assume the full measurement range of the standard thermocouple sensor according to ASTM E230-87.

Figure 2. Thermocouple Types J and N Errors

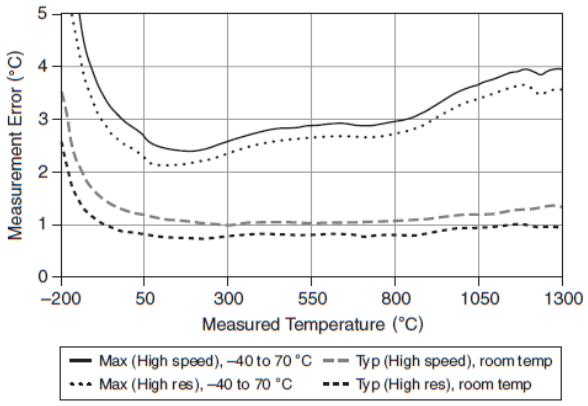

Figure 3. Thermocouple Type K Errors

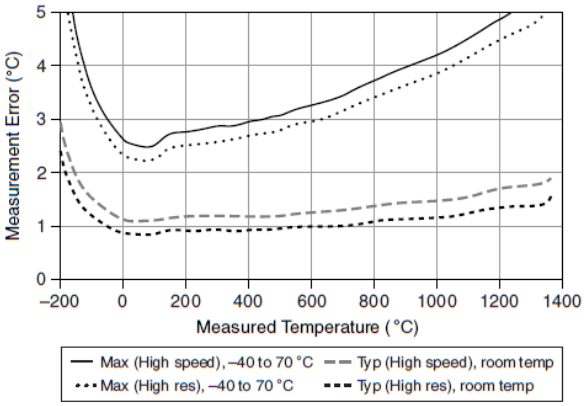

Figure 4. Thermocouple Types T and E Errors

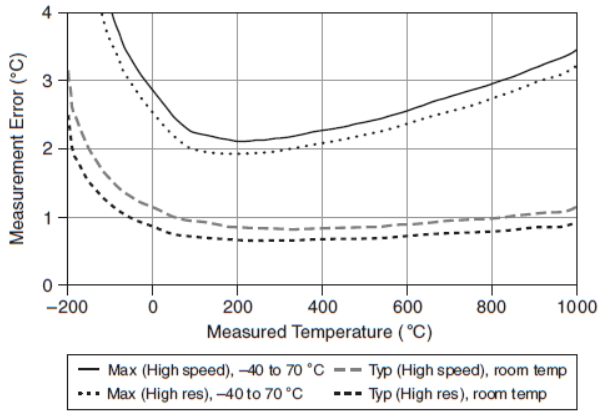

Figure 5. Thermocouple Type B Errors

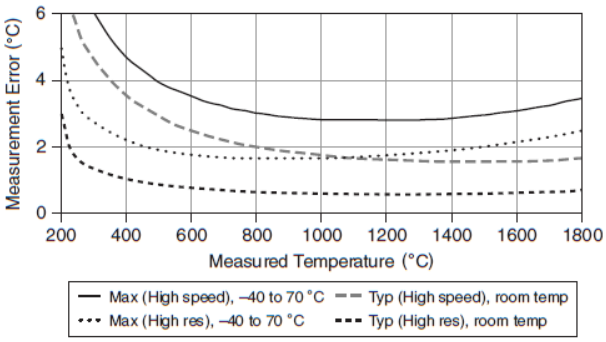

Figure 6. Thermocouple Types R and S Errors

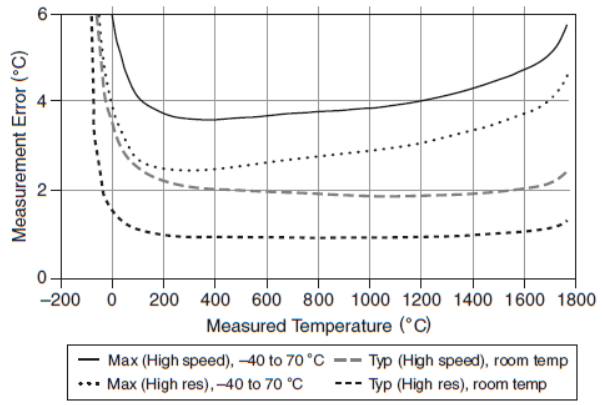

Technical Sales

(866) 531-6285
orders@ni.com

Last Revised: 2014-11-06 07:14:23.0

NI 9219

24-Bit Universal Analog Input

- 250 Vrms channel-to-channel isolation
- Built-in quarter-, half-, and full-bridge support
- Built-in voltage and current excitation
- Thermocouple, RTD, resistance, voltage, and current measurements
- CJC per channel for accurate thermocouple measurement
- 100 S/s/ch simultaneous inputs (50 S/s/ch for thermocouple)

Overview

The NI 9219 is a four-channel universal C Series module designed for multipurpose testing in any NI CompactDAQ or CompactRIO chassis. With the NI 9219, you can measure several signals from sensors such as strain gages, RTDs, thermocouples, load cells, and other powered sensors. The channels are individually selectable, so you can perform a different measurement type on each of the four channels. Measurement ranges differ for each type of measurement and include up to ±60 V for voltage and ±25 mA for current. Please see the manual for detailed specifications and ranges.

Back to Top

Requirements and Compatibility

OS Information

- Real-Time OS
- Windows

Driver Information

- NI-DAQmx
- NI-RIO

Software Compatibility

- LabVIEW
- LabWindows/CVI
- Measurement Studio
- SignalExpress
- Visual Basic
- Visual C#
- Visual C++
- Visual Studio
- Visual Studio .NET

Back to Top

Comparison Tables

Thermocouple Module	Channels	Sample Rate	Resolution	Feature
NI 9213	16	1,200 S/s	24-bit	Lowest cost/channel
NI 9219	4	50 S/s/ch	24-bit	Channel-to-channel isolation
NI 9211	4	14 S/s	24-bit	Low-channel count

Back to Top

Support and Services

System Assurance Programs

NI system assurance programs are designed to make it even easier for you to own an NI system. These programs include configuration and deployment services for your NI PXI, CompactRIO, or Compact FieldPoint system. The NI Basic System Assurance Program provides a simple integration test and ensures that your system is delivered completely assembled in one box. When you configure your system with the NI Standard System Assurance Program, you can select from available NI system driver sets and application development environments to create customized, reorderable software configurations. Your system arrives fully assembled and tested in one box with your software preinstalled. When you order your system with the standard program, you also receive system-specific documentation including a bill of materials, an integration test report, a recommended maintenance plan, and frequently asked question documents. Finally, the standard program reduces the total cost of owning an NI system by providing three years of warranty coverage and calibration service. Use the online product advisors at ni.com/advisor to find a system assurance program to meet your needs.

Calibration

NI measurement hardware is calibrated to ensure measurement accuracy and verify that the device meets its published specifications. To ensure the ongoing accuracy of your measurement hardware, NI offers basic or detailed recalibration service that provides ongoing ISO 9001 audit compliance and confidence in your measurements. To learn more about NI calibration services or to locate a qualified service center near you, contact your local sales office or visit ni.com/calibration.

Technical Support

Get answers to your technical questions using the following National Instruments resources.

- **Support** - Visit ni.com/support to access the NI KnowledgeBase, example programs, and tutorials or to contact our applications engineers who are located in NI sales offices around the world and speak the local language.
- **Discussion Forums** - Visit forums.ni.com for a diverse set of discussion boards on topics you care about.
- **Online Community** - Visit community.ni.com to find, contribute, or collaborate on customer-contributed technical content with users like you.

Repair

While you may never need your hardware repaired, NI understands that unexpected events may lead to necessary repairs. NI offers repair services performed by highly trained technicians who quickly return your device with the guarantee that it will perform to factory specifications. For more information, visit ni.com/repair.

Training and Certifications

The NI training and certification program delivers the fastest, most certain route to increased proficiency and productivity using NI software and hardware. Training builds the skills to more efficiently develop robust, maintainable applications, while certification validates your knowledge and ability.

- **Classroom training in cities worldwide** - the most comprehensive hands-on training taught by engineers.
- **On-site training at your facility** - an excellent option to train multiple employees at the same time.
- **Online instructor-led training** - lower-cost, remote training if classroom or on-site courses are not possible.
- **Course kits** - lowest-cost, self-paced training that you can use as reference guides.
- **Training memberships** and training credits - to buy now and schedule training later.

Visit ni.com/training for more information.

Extended Warranty

NI offers options for extending the standard product warranty to meet the life-cycle requirements of your project. In addition, because NI understands that your requirements may change, the extended warranty is flexible in length and easily renewed. For more information, visit ni.com/warranty.

OEM

NI offers design-in consulting and product integration assistance if you need NI products for OEM applications. For information about special pricing and services for OEM customers, visit ni.com/oem.

Alliance

Our Professional Services Team is comprised of NI applications engineers, NI Consulting Services, and a worldwide National Instruments Alliance Partner program of more than 700 independent consultants and integrators. Services range from start-up assistance to turnkey system integration. Visit ni.com/alliance.

Back to Top

Detailed Specifications

The following specifications are typical for the range –40 to 70 °C unless otherwise noted.

Input Characteristics	
Number of channels	4 analog input channels
ADC resolution	24 bits
Type of ADC	Delta-sigma (with analog prefiltering)
Sampling mode	Simultaneous
Type of TEDS supported	IEEE 1451.4 TEDS Class II (Interface)

Mode input ranges		
Mode	**Nominal Range(s)**	**Actual Range(s)**
Voltage	±60 V, ±15 V, ±4 V, ±1 V, ±125 mV	±60 V, ±15 V, ±4 V, ±1 V, ±125 mV
Current	±25 mA	±25 mA
4-Wire and 2-Wire Resistance	10 kΩ, 1 kΩ	10.5 kΩ, 1.05 kΩ
Thermocouple	±125 mV	±125 mV
4-Wire and 3-Wire RTD	Pt 1000, Pt 100	5.05 kΩ, 505 Ω
Quarter-Bridge	350 Ω, 120 Ω	390 Ω, 150 Ω
Half-Bridge	±500 mV/V	±500 mV/V
Full-Bridge	±62.5 mV/V, ±7.8 mV/V	±62.5 mV/V, ±7.8125 mV/V
Digital In	—	0–60 V
Open Contact	—	1.05 kΩ

Conversion time, no channels in TC mode	
High speed	10 ms for all channels
Best 60 Hz rejection	110 ms for all channels
Best 50 Hz rejection	130 ms for all channels
High resolution	500 ms for all channels
Conversion time, one or more channels in TC mode	
High speed	20 ms for all channels
Best 60 Hz rejection	120 ms for all channels
Best 50 Hz rejection	140 ms for all channels
High resolution	510 ms for all channels
Overvoltage protection	
Terminals 1 and 2	±30 V
Terminals 3 through 6, across any combination	±60 V
Input impedance	
Voltage and Digital In modes (±60 V, ±15 V, ±4 V)	1 MΩ
Current mode	<40 Ω
All other modes	>1 GΩ

Accuracy		
Mode, Range	**Gain Error (Percent of Reading)**	**Offset Error (ppm of Range)**
	Typ (25 °C, ±5 °C), Max (–40 to 70 °C)	
Voltage, ±60 V	±0.3, ±0.4	±20, ±50
Voltage, ±15 V	±0.3, ±0.4	±60, ±180
Voltage, ±4 V	±0.3, ±0.4	±240, ±720
Voltage, ±1 V	±0.1, ±0.18	±15, ±45
Voltage/Thermocouple, ±125 mV	±0.1, ±0.18	±120, ±360
Current, ±25 mA	±0.1, ±0.6	±30, ±100
4-Wire and 2-Wire [1] Resistance, 10 kΩ	±0.1, ±0.5	±120, ±320
4-Wire and 2-Wire [1] Resistance, 1 kΩ	±0.1, ±0.5	±1200, ±3200
4-Wire and 3-Wire RTD, Pt 1000	±0.1, ±0.5	±240, ±640
4-Wire and 3-Wire RTD, Pt 100	±0.1, ±0.5	±2400, ±6400
Quarter-Bridge, 350 Ω	±0.1, ±0.5	±2400, ±6400
Quarter-Bridge, 120 Ω	±0.1, ±0.5	±2400, ±6400
Half-Bridge, ±500 mV/V	±0.03, ±0.07	±300, ±450
Full-Bridge, ±62.5 mV/V	±0.03, ±0.08	±300, ±1000

Accuracy		
Mode, Range	Gain Error (Percent of Reading)	Offset Error (ppm of Range)
	Typ (25 °C, ±5 °C), Max (–40 to 70 °C)	
Full-Bridge, ±7.8 mV/V	±0.03, ±0.08	±2200, ±8000

Cold-junction compensation sensor accuracy	±1°C typ

Stability		
Mode, Range	Gain Drift (ppm of Read-ing/°C)	Offset Drift (ppm of Range/°C)
Voltage, ±60 V	±20	±0.2
Voltage, ±15 V	±20	±0.8
Voltage, ±4 V	±20	±3.2
Voltage, ±1 V	±10	±0.2
Voltage/Thermocouple, ±125 mV	±10	±1.6
Current, ±25 mA	±15	±0.4
4-Wire and 2-Wire Resistance, 10 kΩ	±15	±3
4-Wire and 2-Wire Resistance, 1 kΩ	±15	±30
4-Wire and 3-Wire RTD, Pt 1000	±15	±6
4-Wire and 3-Wire RTD, Pt 100	±15	±60
Quarter-Bridge, 350 Ω	±15	±120
Quarter-Bridge, 120 Ω	±15	±240
Half-Bridge, ±500 mV/V	±3	±20
Full-Bridge, ±62.5 mV/V	±3	±20
Full-Bridge, ±7.8 mV/V	±3	±20

Input noise in ppm of $Range_{rms}$				
Mode, Range	Conversion Time			
	High speed	Best 60 Hz re-jection	Best 50 Hz re-jection	High resolution
Voltage, ±60 V	7.6	1.3	1.3	0.5
Voltage, ±15 V	10.8	1.9	1.9	0.7
Voltage, ±4 V	10.8	2.7	2.7	1.3
Voltage, ±1 V	7.6	1.3	1.3	0.5
Voltage/Thermocouple, ±125 mV	10.8	1.9	1.9	1.0
Current, ±25 mA	10.8	1.9	1.9	1.0
4-Wire and 2-Wire Resistance, 10 kΩ	4.1	1.3	0.8	0.3
4-Wire and 2-Wire Resistance, 1 kΩ	7.1	1.8	1.2	0.7
4-Wire and 3-Wire RTD, Pt 1000	7.6	1.7	1.1	0.4
4-Wire and 3-Wire RTD, Pt 100	10.8	1.9	1.9	0.9
Quarter-Bridge, 350 Ω	5.4	1.0	1.0	0.7
Quarter-Bridge, 120 Ω	5.4	1.0	1.0	0.7
Half-Bridge, ±500 mV/V	3.8	0.5	0.5	0.2
Full-Bridge, ±62.5 mV/V	5.4	1.0	1.0	0.8
Full-Bridge, ±7.8 mV/V	30	4.7	4.7	2.3

Input bias current	<1 nA
INL	±15 ppm
CMRR (f_{in} = 60 Hz)	>100 dB
NMRR	
Best 60 Hz rejection	90 dB at 60 Hz

Best 50 Hz rejection	80 dB at 50 Hz
High resolution	65 dB at 50 Hz and 60 Hz

Excitation level for Half-Bridge and Full-Bridge modes		
Mode	**Load Resistance (Ω)**	**Excitation (V)**
Half-Bridge	700	2.5
	240	2.0
Full-Bridge	350	2.7
	120	2.2

Excitation level for Resistance, RTD, and Quarter-Bridge modes	
Load Resistance (Ω)	**Excitation (mV)**
120	50
350	150
1 k	430
10 k	2200

MTBF	384,716 hours at 25 °C; Bellcore Issue 2, Method 1, Case 3, Limited Part Stress Method

Note Contact NI for Bellcore MTBF specifications at other temperatures or for MIL-HDBK-217F specifications.

Power Requirements

Power consumption from chassis	
Active mode	750 mW max
Sleep mode	25 µW max
Thermal dissipation (at 70 °C)	
Active mode	625 mW max
Sleep mode	25 µW max

Physical Characteristics

Note For two-dimensional drawings and three-dimensional models of the C Series module and connectors, visit ni.com/dimensions and search by module number.

Spring-terminal wiring	18 to 28 AWG copper conductor wire with 7 mm (0.28 in.) of insulation stripped from the end
Weight	156 g (5.5 oz)

Safety

If you need to clean the module, wipe it with a dry towel.

Safety Voltages

Connect only voltages that are within the following limits.

Channel-to-channel	
Continuous	250 VAC, Measurement Category II
Withstand	1,390 VAC, verified by a 5 s dielectric withstand test
Channel-to-earth ground	
Continuous	250 VAC, Measurement Category II
Withstand	2,300 VAC, verified by a 5 s dielectric withstand test
Zone 2 hazardous locations applications in Europe channel-to-channel and channel-to-earth ground	60 VDC, Measurement Category I

Measurement Category I is for measurements performed on circuits not directly connected to the electrical distribution system referred to as MAINS [2] voltage. This category is for measurements of voltages from specially protected secondary circuits. Such voltage measurements include signal levels, special equipment, limited-energy parts of equipment, circuits powered by regulated low-voltage sources, and electronics.

Caution Do *not* connect to signals or use for measurements within Measurement Categories II, III, or IV.

Measurement Category II is for measurements performed on circuits directly connected to the electrical distribution system. This category refers to local-level electrical distribution, such as that provided by a standard wall outlet (e.g., 115 V for U.S. or 230 V for Europe). Examples of Measurement Category II are measurements performed on household appliances, portable tools, and similar products.

Caution Do *not* connect to signals or use for measurements within Measurement Categories III or IV.

Hazardous Locations	
U.S. (UL)	Class I, Division 2, Groups A, B, C, D, T4; Class I, Zone 2, AEx nA IIC T4
Canada (C-UL)	Class I, Division 2, Groups A, B, C, D, T4; Class I, Zone 2, Ex nA IIC T4
Europe (DEMKO)	Ex nA IIC T4

Safety Standards

This product is designed to meet the requirements of the following standards of safety for electrical equipment for measurement, control, and laboratory use:

- IEC 61010-1, EN 61010-1
- UL 61010-1, CSA 61010-1

Note For UL and other safety certifications, refer to the product label or the *Online Product Certification* section.

Electromagnetic Compatibility

This product meets the requirements of the following EMC standards for electrical equipment for measurement, control, and laboratory use:

- EN 61326 (IEC 61326): Class A emissions; Industrial Immunity
- EN 55011 (CISPR 11): Group 1, Class A emissions
- AS/NZS CISPR 11: Group 1, Class A emissions
- FCC 47 CFR Part 15B: Class A emissions
- ICES-001: Class A emissions

Note For the standards applied to assess the EMC of this product, refer to the *Online Product Certification* section.

Note For EMC compliance, operate this device with shielded cables.

CE Compliance

This product meets the essential requirements of applicable European Directives, as amended for CE marking, as follows:

- 2006/95/EC; Low-Voltage Directive (safety)
- 2004/108/EC; Electromagnetic Compatibility Directive (EMC)

Note For the standards applied to assess the EMC of this product, refer to the *Online Product Certification* section.

Online Product Certification

Refer to the product Declaration of Conformity (DoC) for additional regulatory compliance information. To obtain product certifications and the DoC for this product, visit ni.com/certification, search by module number or product line, and click the appropriate link in the Certification column.

Shock and Vibration

To meet these specifications, you must panel mount the system.

Operating vibration	
Random (IEC 60068-2-64)	5 g_{rms}, 10 to 500 Hz
Sinusoidal (IEC 60068-2-6)	5 g, 10 to 500 Hz
Operating shock (IEC 60068-2-27)	30 g, 11 ms half sine, 50 g, 3 ms half sine, 18 shocks at 6 orientations

Environmental

National Instruments C Series modules are intended for indoor use only but may be used outdoors if installed in a suitable enclosure. Refer to the manual for the chassis you are using for more information about meeting these specifications.

Operating temperature (IEC 60068-2-1, IEC 60068-2-2)	–40 to 70 °C
Storage temperature (IEC 60068-2-1, IEC 60068-2-2)	–40 to 85 °C
Ingress protection	IP 40
Operating humidity (IEC 60068-2-56)	10 to 90% RH, noncondensing
Storage humidity (IEC 60068-2-56)	5 to 95% RH, noncondensing
Maximum altitude	2,000 m
Pollution Degree (IEC 60664)	2

Environmental Management

National Instruments is committed to designing and manufacturing products in an environmentally responsible manner. NI recognizes that eliminating certain hazardous substances from our products is beneficial not only to the environment but also to NI customers.

Technical Sales

(866) 531-6285
orders@ni.com

Requirements and Compatibility | Ordering Information | Detailed Specifications
For user manuals and dimensional drawings, visit the product page resources tab on ni.com.

Last Revised: 2014-11-06 07:14:37.0

NI 9435

Requirements and Compatibility

OS Information

- Real-Time OS
- Windows

Driver Information

- NI-DAQmx
- NI-RIO

Software Compatibility

- LabVIEW
- LabWindows/CVI
- SignalExpress
- Visual Studio
- Visual Studio .NET

Back to Top

Ordering Information

For a complete list of accessories, visit the product page on ni.com.

Products	Part Number	Recommended Accessories	Part Number
		No accessories required.	

Back to Top

Software Recommendations

LabVIEW Professional Development System for Windows

- Advanced software tools for large project development
- Automatic code generation using DAQ Assistant and Instrument I/O Assistant
- Tight integration with a wide range of hardware
- Advanced measurement analysis and digital signal processing
- Open connectivity with DLLs, ActiveX, and .NET objects
- Capability to build DLLs, executables, and MSI installers

NI LabWindows™/CVI for Windows

- Real-time advanced 2D graphs and charts
- Complete hardware compatibility with IVI, VISA, DAQ, GPIB, and serial
- Analysis tools for array manipulation, signal processing statistics, and curve fitting
- Simplified cross-platform communication with network variables
- Measurement Studio .NET tools (included in LabWindows/CVI Full only)
- The mark LabWindows is used under a license from Microsoft Corporation.

NI LabVIEW FPGA Module

Detailed Specifications

The following specifications are typical for the range –40 to 70 °C unless otherwise noted. All voltages are relative to DIa–DIb unless otherwise noted.

Input Characteristics	
Number of channels	4 digital input channels
Input type	Sinking or sourcing
Digital logic levels	
OFF state	
Input voltage	≤±1 VDC/VAC_{peak}
Input current	≤±200 µA DC/AC_{peak}
ON state	
DC input voltage	≥±4 VDC
DC input current	≥600 µA DC
AC input voltage	≥10 V_{rms} at 50/60 Hz
AC input voltage	≥3 V_{rms} at 1 kHz
I/O protection	
Input voltage (DIa–DIb)	250 VAC, ±250 VDC max
Input current	±1.4 mA, internally limited
Input delay time [1]	2.8 ms max
MTBF	700,726 hours at 25 °C; Bellcore Issue 2, Method 1, Case 3, Limited Part Stress Method

Note Contact NI for Bellcore MTBF specifications at other temperatures or for MIL-HDBK-217F specifications.

Power Requirements	
Power consumption from chassis	
Active mode	105 mW max
Sleep mode	1.3 mW max
Thermal dissipation (at 70 °C)	
Active mode	1.4 W max
Sleep mode	1.35 W max

Physical Characteristics	

If you need to clean the module, wipe it with a dry towel.

Note For two-dimensional drawings and three-dimensional models of the C Series module and connectors, visit ni.com/dimensions and search by module number.

Screw-terminal wiring	12 to 24 AWG copper conductor wire with 10 mm (0.39 in.) of insulation stripped from the end.
Torque for screw terminals	0.5 to 0.6 N · m (4.4 to 5.3 lb · in.)
Ferrules	0.25 mm^2 to 2.5 mm^2
Weight	150 g (5.3 oz)

Safety	
Safety Voltages	
Connect only voltages that are within the following limits.	
DIa-to-DIb	250 V_{rms} max, Measurement Category II
Isolation	
Channel-to-channel	None
Channel-to-earth ground	
Continuous	250 V_{rms}, Measurement Category II

Withstand	2,300 V_{rms}, verified by a 5 s dielectric withstand test

Measurement Category II is for measurements performed on circuits directly connected to the electrical distribution system (MAINS [2]). This category refers to local-level electrical distribution, such as that provided by a standard wall outlet (for example, 115 AC voltage for U.S. or 230 AC voltage for Europe). Examples of Measurement Category II are measurements performed on household appliances, portable tools, and similar hardware.

Caution Do not connect the NI 9435 to signals or use for measurements within Measurement Categories III or IV.

Hazardous Locations

U.S. (UL)	Class I, Division 2, Groups A, B, C, D, T4

Note The NI 9435 is not approved for use in hazardous locations in Europe or Canada.

Safety Standards

This product is designed to meet the requirements of the following standards of safety for electrical equipment for measurement, control, and laboratory use:

- IEC 61010-1, EN 61010-1
- UL 61010-1, CSA 61010-1

Note For UL and other safety certifications, refer to the product label or the *Online Product Certification* section.

Electromagnetic Compatibility

This product is designed to meet the requirements of the following standards of EMC for electrical equipment for measurement, control, and laboratory use:

- EN 61326 (IEC 61326): Class A emissions; Industrial immunity
- EN 55011 (CISPR 11): Group 1, Class A emissions
- AS/NZS CISPR 11: Group 1, Class A emissions
- FCC 47 CFR Part 15B: Class A emissions
- ICES-001: Class A emissions

Note For the standards applied to assess the EMC of this product, refer to the *Online Product Certification* section.

Note For EMC compliance, operate this device with double-shielded cables.

CE Compliance

This product meets the essential requirements of applicable European Directives, as amended for CE marking, as follows:

- 2006/95/EC; Low-Voltage Directive (safety)
- 2004/108/EC; Electromagnetic Compatibility Directive (EMC)

Note For the standards applied to assess the EMC of this product, refer to the *Online Product Certification* section.

Online Product Certification

Refer to the product Declaration of Conformity (DoC) for additional regulatory compliance information. To obtain product certifications and the DoC for this product, visit ni.com/certification, search by module number or product line, and click the appropriate link in the Certification column.

Shock and Vibration

To meet these specifications, you must panel mount the system and either affix ferrules to the ends of the terminal wires or use the NI 9932 backshell kit to protect the connections.

Operating vibration	
Random (IEC 60068-2-64)	5 g_{rms}, 10 to 500 Hz
Sinusoidal (IEC 60068-2-6)	5 g, 10 to 500 Hz
Operating shock (IEC 60068-2-27)	30 g, 11 ms half sine, 50 g, 3 ms half sine, 18 shocks at 6 orientations

Environmental

National Instruments C Series modules are intended for indoor use only, but may be used outdoors if installed in a suitable enclosure. Refer to the manual for the chassis you are using for more information about meeting these specifications.

Operating temperature	–40 to 70 °C
Storage temperature	–40 to 85 °C
Ingress protection	IP 40
Operating humidity	10 to 90% RH, noncondensing
Storage humidity	5 to 95% RH, noncondensing
Maximum altitude	2,000 m
Pollution Degree	2

Environmental Management

National Instruments is committed to designing and manufacturing products in an environmentally responsible manner. NI recognizes that eliminating certain hazardous substances from our products is beneficial not only to the environment but also to NI customers.

7102

Micro-Bath

3.1 Specifications

Table 2. Specifications

Range	–5 to 125 °C (23 to 257 °F)
Accuracy	±0.25 °C
Stability	±0.015 °C at –5 °C (oil, 5010) ±0.03 °C at 121 °C (oil, 5010)
Uniformity	±0.02 °C
Resolution	0.01 °C/F
Operating Temperature	5 to 45 °C (41 to 113 °F)
Heating Time	25 °C to 100 °C (77 °F to 212 °F): 30 minutes
Cooling Time	25 °C to 0 °C (77 °F to 32 °F): 30 minutes
Well Size	2.5" dia. x 5.5" deep (64 x 139 mm) (access opening is 1.9" [48 mm] in diameter)
Exterior Dimension	12" H x 7.2" W x 9.5" D (31 cm x 18 cm x 24 cm)
Weight	15 lb. (6.8 kg) with fluid
Power	115 VAC (±10 %), 1.8 A, or 230 VAC (±10 %), 0.9 A, switchable, 50/60 Hz, 200 W
Readout	Switchable °C or °F
Controller	Digital controller with data retention
Thermal Electric Devices (TED)	150 W
Cooling	Fan and Thermal Electric Devices (TED)
Fault Protection	Sensor burnout and short protection
Safety	Overvoltage (Installation) Category II, Pollution Degree 2 per IEC 61010-01
Fuse Rating	115 V: 250 V 3A SB (slow blow) 230 V: 250 V 1.6 A T (time delay)

My Orders | My Library | My Profile | Welcome jskaalum@dal.ca Log out | Help

My Orders > Orders > All Orders

My Orders

Orders | Billing History | Payable Invoices

SEARCH

Order Number:

Date Range: From 11-Sep-2017 To 11-Dec-2017 Go

View: All | Response Required | Pending | Completed | Canceled | Denied | Credited

Results: 1-3 of 3

Order Date	Article Title	Publication	Type Of Use	Order Status	Order Number
26-Sep-2017	Sensible and latent thermal energy storage with constructal fins	International Journal of Hydrogen Energy	reuse in a thesis/dissertation	Completed	4196510226581
26-Sep-2017	Response surface method optimization of innovative fin structure for expediting discharging process in latent heat thermal energy storage system containing nano-enhanced phase change material	Journal of the Taiwan Institute of Chemical Engineers	reuse in a thesis/dissertation	Completed	4196510100820
26-Sep-2017	Maximization of performance of a PCM latent heat storage system with innovative fins	Applied Energy	reuse in a thesis/dissertation	Completed	4196501480339